Spring 1-1-2014

Open-Loop Thrust Profile Development for Tethered Towing of Large Space Objects

Lee E.Z. Jasper
University of Colorado at Boulder, lee.jasper@colorado.edu

Open-Loop Thrust Profile Development for Tethered Towing of Large Space Objects

by

Lee E. Z. Jasper

B.S., University of Colorado, Boulder, 2010

M.S., University of Colorado, Boulder, 2010

A thesis submitted to the

Faculty of the Graduate School of the

University of Colorado in partial fulfillment

of the requirements for the degree of

Doctor of Philosophy

Department of Aerospace Engineering Science

2014

This thesis entitled:
Open-Loop Thrust Profile Development for Tethered Towing of Large Space Objects
written by Lee E. Z. Jasper
has been approved for the Department of Aerospace Engineering Science

_____
Dr. Hanspeter Schaub - Committee Chair

_____
Dr. John K. Bennett

_____
Dr. Brandon Jones

_____
Dr. Jeffrey Parker

_____
Dr. Daniel Scheeres

Date _____

The final copy of this thesis has been examined by the signatories, and we find that both the content and the form meet acceptable presentation standards of scholarly work in the above mentioned discipline.

Jasper, Lee E. Z. (Ph.D., Aerospace Engineering Science)

Open-Loop Thrust Profile Development for Tethered Towing of Large Space Objects

Thesis directed by Dr. Hanspeter Schaub - Committee Chair

Towing objects in space has become an increasingly researched mission concept. Active debris removal, satellite servicing, and asteroid retrieval concepts in many cases rely on a thrusting vehicle to redirect and steer a passive object. Focus is often placed on the method of attachment, considering techniques such as grappling or netting the passive object. However, the actual process of towing, once capture has occurred, has not yet received much attention. This research considers the process of towing in space with the tug and passive object attached by a tether. Tethers are not only an effective way of transmitting forces, but they are utilized on many of the towing concepts considered, especially in orbital debris removal.

Because the two end bodies are tethered, there is a potential for collision after any maneuver. To avoid collisions, the maneuver, and therefore thrust profile, must be designed in such a way as to limit separation distance reduction between the end bodies. Open-loop input shaping techniques are developed and employed in order to control the flexible system in both deep space and on-orbit environments. To study the behavior, an active debris removal system is proposed as a case study. This system, called the tethered-tug, considers using the reserve fuel from a recently launched upper stage rocket to rendezvous with, capture, and tow a near-by debris object.

The system's performance is considered for five distinct open-loop thrust control profiles including on-off/step, frequency notched, discretized notch, Posicast, and bang-off-bang. Tether property variations are also considered along with off-axis towing, slack tethers, and debris with initial rotation rates. Input shaping is not only necessary but, it can be robust to unknown system properties while nearly zeroing relative motion between the end bodies. When considering on-orbit behavior specifically, the system settles into a tumbling or gravity gradient oscillation formation. This is highly advantageous because the orbital dynamics keep the end bodies separated. While the study focuses on the debris problem, conclusions from this dissertation are applicable to general tethered towing mission concepts.

Dedication

To those who will keep space clean.

Acknowledgements

The best way to become better at something is to be surrounded by others who are models of excellence. Dr. Hanspeter Schaub is exactly that, excellent. He excels in just about everything I have seen him attempt and I am honored to have learned from him. This research, and my development as an engineer, are possible because of him. I would also like to thank my committee: Dr. John K. Bennett, who has been a friend and mentor throughout my college career, Dr. Brandon Jones, Dr. Jeffrey Parker, and Dr. Daniel Scheeres.

It is hard to get anywhere in the world without great parents. I am unimaginably fortunate to have always had the love and support of my parents Peter and Leslie Jasper. You have given me a world of opportunity and I hope I can always take advantage of that, to make you proud, and pay it forward.

Alicia Harris, you have seen every good and bad day and been encouraging throughout. This whole process would have been *so much more* difficult without your loving presence. This thesis is, in many ways, a testament to your patience and endurance. Thank you.

Chris Koehler, Brian Sanders, Bernadette Garcia: for being great educators and providing experiences that I never thought I would get, for always being welcoming...and for too many things to keep this short.

Marcin Pilinski, Bruce Davis, Mike Grusin, and Brady Young: for inspiring me to pursue a Ph. D.

The AVS Lab: Carl Seubert, Laura Stiles, Steve O'Keefe, Erik Hogan, Paul Anderson, Daan Stevenson, Lauren McManus, Trevor Bennett, Stephanie Jones, Robin Blenden, Samantha Krening, Peter Jasch, Steve Panosian: for your collaboration and making going to work fun. I would especially like to thank Anthony Lima. He has been extremely helpful by, literally, aiding me in visualizing the system while pursuing several areas of study that I would not have been able to address.

Contents

Chapter

1 Introduction 1

1.1 Space Debris: Environment and Active Debris Removal 2

1.1.1 Growth of Human-Made Objects in Space 2

1.1.2 The Case for Active Debris Removal 7

1.1.3 Challenges for Active Debris Removal 9

1.2 Tethered - Tug Concept: Prospects and Challenges 10

1.2.1 System Description 10

1.2.2 Motivation of Research 12

1.3 Literature Review 13

1.3.1 Active Debris Removal Related Research 13

1.3.2 Previous Tether Research 17

1.4 Research Intent 18

1.4.1 Goals 18

1.4.2 Scope 19

1.4.3 Contributions 20

1.5 Thesis Outline 22

2 Modeling the Rigid Body-to-Tether Interaction 23

2.1 Simulation Software Architecture 23

2.2 Tethered-Tug System Model 24
2.2.1 Equations of Motion 25
2.2.2 Modal Analysis 30
2.2.3 Verification of Model 33
2.2.4 Number of Tether Discretizations 37
2.2.5 Deep Space Simulations 37
2.2.6 Orbital Simulations 38
2.3 Baseline Concept Parameters 39

3 Open-Loop Input Shaping for the Tethered-Tug System 41
3.1 Un-Shaped Input: the Step Input 41
3.2 Description of Input Shaping 42
3.3 Notch Filter Input Shaping 44
3.3.1 Concept 44
3.3.2 Design 45
3.3.3 Adding Robustness 46
3.3.4 Deep Space Performance 50
3.3.5 On-orbit Performance 55
3.3.6 Discretized Double Notch 62
3.4 Posicast Input Shaping 67
3.4.1 Concept 67
3.4.2 Design 67
3.4.3 Adding Robustness 71
3.4.4 Deep Space Performance 75
3.4.5 On-orbit Performance 76
3.5 Bang-Bang Input Shaping 78
3.5.1 Concept 78

3.5.2 Design . . . 78
3.5.3 Deep Space Performance . . . 81
3.5.4 On-orbit Performance . . . 82
3.6 Conclusions . . . 84

4 Tether Design 85
4.1 Considered Tether Properties . . . 86
4.1.1 Length Trade Space . . . 86
4.1.2 Elasticity Trade Space . . . 87
4.1.3 Damping Trade Space . . . 87
4.2 Modifications to Posicast Control . . . 88
4.3 Tether Length . . . 89
4.4 Tether Stiffness . . . 94
4.5 Longitudinal Damping . . . 96
4.6 Stiffness and Damping Study . . . 100
4.6.1 Linearized 'Gain' Study . . . 101
4.6.2 Stiffness and Damping Sweeps . . . 104
4.7 Conclusions . . . 105

5 Slack Tethers and Rotational Debris Motion 106
5.1 Slack Tethers . . . 106
5.1.1 Effects of a slack tether . . . 107
5.1.2 Input Shaping Methods' Sensitivity to a Slack Tether . . . 108
5.1.3 Input Shaping Methods' Sensitivity to a Tensioned Tether . . . 110
5.2 Rotational Motion . . . 112
5.2.1 Challenges of Towing Rotating Debris . . . 112
5.2.2 Offset Tether Attachment to Debris . . . 113
5.2.3 Tumbling Debris . . . 118

5.3 Conclusions 119

6 Conclusion 121

6.1 Thesis Summary 121

6.2 Future Work for the Tethered-Tug System 123

Bibliography 125

Tables

Table

2.1 Vehicle, Tether and Simulation Parameters 40

3.1 Lifetime of Tethered-Tug system using Jacchia 1977 atmosphere model[44] 62

4.1 Change in natural frequency, and mass with tether length, L_0. $E = 170$ GPa, $C = 0\ \frac{kg}{s}$ . . . 87

4.2 Change in natural frequency with Young's modulus, E. $L_0 = 1$ km, $C = 0\ \frac{kg}{s}$ 87

4.3 Change in natural frequency with tether damping, C. $L_0 = 1$ km, $E = 170$ GPa. 88

4.4 End body rotation rate average and standard deviation for L_0 study. $E = 170$ GPa, $C = 0\ \frac{kg}{s}$ 93

4.5 Summary of tether length, L_0, study. $E = 170$ GPa, $C = 0\ \frac{kg}{s}$ 94

4.6 End body rotation rate average and standard deviation for E study. $L_0 = 1000$ m, $C = 0\ \frac{kg}{s}$ 94

4.7 Summary of tether stiffness, E, study. $L_0 = 1000$ m, $C = 0\ \frac{kg}{s}$ 96

4.8 End body rotation rate average and standard deviation for the *Posicast* profile C study. $L_0 =$ 1000 m, $E = 170$ GPa 99

4.9 End body rotation rate average and standard deviation for the *step* profile C study. $L_0 =$ 1000 m, $E = 170$ GPa 99

4.10 Summary of tether damping, C, study. $E = 170$ GPa, $L_0 = 1$ km 100

4.11 Summary of tether stiffness E and damping C study using a *step* input. $L_0 = 1$ km 105

5.1 Maximum slack possible in tether for a given shaping method. Deep space. $L_0 = 1$ km, the debris mass is 2000 kg (1500 kg expected). Simulation duration of 1500 s. 108

5.2 Maximum slack possible in tether for a given shaping method. On-orbit. $L_0 = 1$ km, the debris mass is 2000 kg (1500 kg expected). Simulation duration of 6 orbits. 109

5.3 Response of various pre-existing tensions in tether for a given shaping method. Deep space. $L_0 = 1$ km, the debris mass is 2000 kg (1500 kg expected). Simulation duration of 1500 s. . 110

5.4 Response of various existing tensions in tether for a given shaping method. On-orbit. $L_0 =$ 1 km, the debris mass is 2000 kg (1500 kg expected). Simulation duration of 6 orbits. . . . 111

Figures

Figure

1.1 1

1.2 Estimated number of objects in Low Earth Orbit, as of 1998[67] 3

1.3 Mitigation Techniques: Impact of Passivation and SRM Slag Avoidance[35] 5

1.4 No Mitigation as Predicted by NASA's LEGEND[47] 5

1.5 Expected number of future collisions due to debris 6

1.6 Percentage of All Observed Breakups Compared to the Number of Launches in a Given Year 8

1.7 Mitigation and ADR Estimates for Improving LEO Debris Populations[47] 8

1.8 Examples of tethered tug concepts 10

1.9 Top 500 Objects for ADR[47] 12

1.10 Debris Capture Concepts 15

2.1 Segment of a string model of a tether 24

2.2 Discretized tether model example with 2 tether masses 25

2.3 Discretized tether model example with 2 tether masses 27

2.4 TCS rotational test model. Voltages applied to rigid end bodies 34

2.5 Energy change in simulation due to integration step size, 2 orbits. Maximum energy of system $\approx 100 \times 10^{11}$ J. 36

2.6 Angular momentum change for 6^o/sec end body rotation rate in deep space. Maximum momentum of system $\approx 2 \times 10^6$ N-s. 36

2.7 System performance variation due to multiple tether masses 38
2.8 Upper stage rocket bodies used for this study 39

3.1 Relative motion and tether tension between tug and debris for a step input. Thrust duration of $\tilde{2}00$ s. Deep space 42
3.2 Open-loop control block diagram 42
3.3 Example thrust profiles considered 43
3.4 Bode plot demonstrating notch frequency response 45
3.5 Sensitivity of the tether-mass system's first two fundamental modes to imperfect debris mass knowledge 48
3.6 Double notch centered about first fundamental mode of system 49
3.7 Sensitivity of the tether-mass system's first fundamental mode ($\omega_n = 0.17$ Hz) to variable spring constant 49
3.8 Thrust profiles with different input shaping techniques 50
3.9 **Tug** vehicle frequency response to 2009 N thrust, with 2 discrete tether masses. Deep space . 51
3.10 Relative motion and tether tension response between tug and debris for a single notch with the cut off frequency at the first mode. 2009 N thrust, with 2 discrete tether masses. Deep space 52
3.11 **Tether mass** frequency response to 2009 N thrust, with 2 discrete tether masses. Deep space 52
3.12 **Debris** object frequency response to 2009 N thrust, with 2 discrete tether masses. Deep space 52
3.13 Relative motion and tether tension response between tug and debris for an expected debris mass of 2000 kg ($\omega_n = 0.17$ Hz), actual mass is 1500 kg ($\omega_n = 0.19$ Hz). 2009 N thrust, with 2 discrete tether masses. Deep space 53
3.14 **Tug** vehicle frequency response with 2 discrete tether masses. Expected $\omega_n = 0.17$ Hz, actual $\omega_n = 0.19$ Hz. Deep space 54

3.15 Tug vehicle frequency response to Spring Constant K_S variability with 2 discrete tether masses. Expected $\omega_n = 0.17$ Hz, actual $\omega_n = 0.21$ Hz. Deep space 54

3.16 Relative motion and tether tension response between tug and debris for four orbits. Tether $\omega_n = .19$ Hz. 2009 N thrust, with 2 discrete tether masses. On-orbit 56

3.17 Notch end body rotation rates over 4 orbits 56

3.18 Angle from along-track vector. 90^o is the radial vector. On-orbit 57

3.19 On-orbit tug/m_T vehicle frequency response with 2 discrete tether masses. Tether $\omega_n = 0.19$ Hz. On-orbit 57

3.20 On-orbit tether mass frequency response with 2 discrete tether masses. Tether $\omega_n = 0.19$ Hz. On-orbit 58

3.21 On-orbit debris/m_D object frequency response with 2 discrete tether masses. Tether $\omega_n = 0.19$ Hz. On-orbit 58

3.22 Behavior of the double notched system over 36 orbits. Tether $\omega_n = .19$ Hz. 2009 N thrust, with 2 discrete tether masses. On-orbit 59

3.23 Behavior of the double notched system given a 0.5 s radial thrust after notch filtering. Tether $\omega_n = .19$ Hz. 2009 N thrust, with 2 discrete tether masses. On-orbit 60

3.24 Required impulsive Δv to achieve periapsis altitude, given a starting 800 km circular orbit . 61

3.25 Applied thrust profiles with different input shaping techniques 63

3.26 Relative motion and tether tension response between tug and debris using a *discretized notch* profile. Expected debris mass of 2000 kg ($\omega_n = .17$ Hz), actual mass is 1500 kg ($\omega_n = .19$ Hz). 2009 N thrust, with 2 discrete tether masses. Deep space 63

3.27 Tug vehicle frequency response to 2009 N thrust, with 2 discrete tether masses. Deep space . 64

3.28 Relative motion and tether tension response between tug and debris for four orbits. Tether $\omega_n = .19$ Hz. 2009 N thrust, with 2 discrete tether masses. On-orbit 65

3.29 Discretized notch end body rotation rates over 4 orbits 66

3.30 Discretized notch angle from along-track vector. 90^o is the radial vector 66

3.31 Separation distance and tether tension in deep space, $\Delta t_{\text{burn}} = 101$ s, $\Delta v = 120$ m/s. $K_S = 1360$ N/m, T = 5kN 69

3.32 Residual vibration (percentage) from each Posicast method. Debris mass varies between 1000 kg and 2000 kg (nominal at 1500 kg, $\omega_n = 1.21$ rad/s). 74

3.33 Relative motion and tether tension response between tug and debris. *Robust Posicast* thrust shaping, Eq. (3.24). Expected debris mass of 2000 kg ($\omega_n = 0.17$ Hz), actual mass is 1500 kg ($\omega_n = 0.19$ Hz). 2009 N thrust, with 2 discrete tether masses. Deep space 75

3.34 Tug vehicle frequency response to *Robust Posicast* 2009 N thrust, with 2 discrete tether masses. Deep space 76

3.35 *Robust Posicast* relative motion and tether tension response between tug and debris for four orbits. Tether $\omega_n = 0.19$ Hz. 2009 N thrust, with 2 discrete tether masses. On-orbit 77

3.36 *Robust Posicast* end body rotation rates over 4 orbits 77

3.37 *Robust Posicast* angle from along-track vector. 90^o is the radial vector 78

3.38 Relative motion and tether tension response between tug and debris using a *Bang-off-bang* thrust profile. Expected debris mass of 2000 kg ($\omega_n = 0.17$ Hz), actual mass is 1500 kg ($\omega_n = 0.19$ Hz). 2009 N thrust, with 2 discrete tether masses. Deep space 82

3.39 Tug vehicle frequency response to a *Bang-off-bang* 2009 N thrust, with 2 discrete tether masses. Deep space 83

3.40 *Bang-off-bang* relative motion and tether tension response between tug and debris for four orbits. Tether $\omega_n = 0.19$ Hz. 2009 N thrust, with 2 discrete tether masses. On-orbit 83

3.41 *Bang-off-bang* end body rotation rates over 4 orbits 83

3.42 Bang-off-bang angle from along-track vector. 90^o is the radial vector 84

4.1 Tether properties considered for on orbit towing to achieve gravity gradient oscillation about θ 85

4.2 Relative motion and tether tension between tug and debris with a *step* input. $L_0 = 1$ km, $E = 170$ GPa and $C = 0\ \frac{kg}{s}$. The debris' expected mass is 1500 kg but it is actually 2000 kg in simulation. Tension scaled by 27.78. Tether length study. 90

4.3 Relative motion and tether tension between tug and debris with a Posicast input. $E = 170$ GPa and $C = 0\ \frac{kg}{s}$. The debris' expected mass is 1500 kg but it is actually 2000 kg in simulation. Tension scaled by 27.78. Tether length study. 91

4.4 Rotation rate of end bodies for $L_0 = 1000$ m tether length study. 92

4.5 Relative motion and tether tension between tug and debris with a Posicast input. $L_0 = 1$ km, $C = 0\ \frac{kg}{s}$. The debris' expected mass is 1500 kg but it is actually 2000 kg in simulation. Tension scaled by 27.78. Stiffness study. 95

4.6 Relative motion and tether tension between tug and debris with a *step* input. $L_0 = 1$ km, $E = 170$ GPa and $C = 8\ \frac{kg}{s}$. The debris' expected mass is 1500 kg but it is actually 2000 kg in simulation. Tension scaled by 27.78. Damping study. 97

4.7 Relative motion and tether tension between tug and debris with a *Posicast* input. $L_0 = 1$ km, $E = 170$ GPa. The debris' expected mass is 1500 kg but it is actually 2000 kg in simulation. Tension scaled by 27.78. Damping study. 98

4.8 Example system properties of $C = 0.1\frac{kg}{s}$ for the Posicast control 100

4.9 Orbit and tether frame definitions using Euler Angles 101

5.1 Illustration of a slack tether, just prior to thrusting, with a taut length of L_0 106

5.2 Slack tether: 1000 m tether with 200 m of slack. Simulated in deep space with a double notch ($.14 \leq \omega_c \leq .22$ Hz), assuming a debris mass of 2000 kg (actual 1500 kg), 2009 N thrust, 2 discrete tether masses. Deep space 107

5.3 Motion of system using a notch and 25 m of slack 109

5.4 Tether attachment locations on debris 112

5.5 Tether attachment model inducing rotation about 'pitch' axis (about the minor axis of the cylinder) 113

5.6 Approximate frequency response as thrust varies 115

5.7 Deep space performance of system with various tether attachment offsets about debris minor inertia axis 116

5.8 Example deep space rotation rates of the end bodies with $\phi_0 = 10^o$ 117

5.9 End body motion for a Posicast control with initial tether attachment offset, on-orbit 118

5.10 End body motion for a Posicast control with body rotation rate of 1.15^o/sec about each axis, on-orbit 119

Chapter 1

Introduction

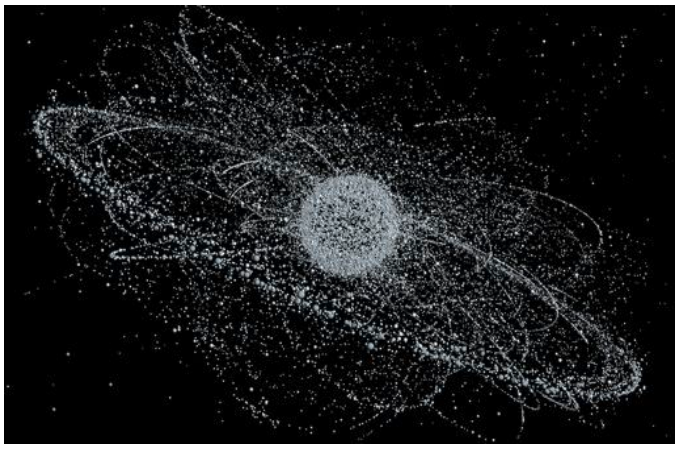

Figure 1.1: Illustration of human-made orbital debris surrounding Earth[1]

Throughout the course of human history, exploration into unknown, new environments has been dangerous, but also exciting and hope-filled endeavors. Frequently, explorers have set the path for pioneers who create infrastructure and economic foundations for settlers to then arrive and prosper. This often brings about great change in the world. Unfortunately, humans also introduce a myriad of problems to the new frontier.

While we are only yet explorers in space, we have begun to litter our near-Earth environment. The extensive use of Earth orbit, without regard for the the effects we can have, has literally created an orbital environmental issue. Figure 1.1 illustrates this by marking approximate locations of orbital debris, at a given

[1] http://firstlook.pnas.org/michael-najjar-artist-in-space/

time. Still, there is hope that this problem can not only be corrected, but improved so that our continued use of space remains relatively unhindered by space debris.

This dissertation considers the current Low Earth Orbit (LEO) debris environment and considers one possible method for actively removing high-risk, large debris from orbit.

1.1 Space Debris: Environment and Active Debris Removal

In order to understand why the orbits around Earth have become hazardous, the context of human operations in space must be known. A very brief history of debris in orbit is given and the decision to consider Active Debris Removal is discussed.

1.1.1 Growth of Human-Made Objects in Space

1.1.1.1 Historical Orbital Debris Events

The space surrounding Earth has become increasingly crowded due to our growing dependence on satellite technology for communications, exploration, and military endeavors. Objects in Earth orbit have been tracked and cataloged since 1961[67] by the U.S. Air Force for communications tracking as well as identification of foreign satellites. However, the use of tracking to provide conjunction assessments has become an increasingly important role of the catalog. Out of the 22,000 objects of at least 10 cm in size that are tracked[22] in orbit, approximately 1,100 are functioning assets. This means that there are about 20,900 objects that are debris. The number of debris jumps significantly when the known, but uncataloged debris are considered. These are debris that may be seen by some of the more powerful observatories, however they are not consistently tracked due to the lack of ability for persistent observation or unknown dynamics as with high area-to-mass ratio objects.[74] This number is often registered in the many tens of thousands.[84] An estimated number of debris by size is shown in Figure 1.2. (Note that this figure is from 1998 and does not capture the major recent events and therefore is an underestimate.)

When space operations first started in 1957, the majority of the objects in Earth orbit were dust and micro-meteoroids. For all intents and purposes, it was assumed that the “Big Sky Theory” held true:

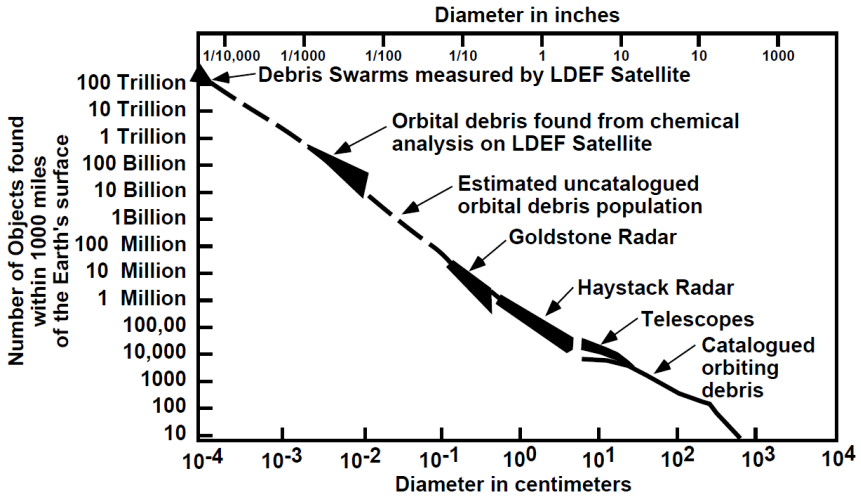

Figure 1.2: Estimated number of objects in Low Earth Orbit, as of 1998[67]

due to the large volume of space and small volume of a satellite the probability for collisions was very small. Therefore, most organizations paid little attention to debris and sources of debris creation. This can be summarized by the 1967 Apollo collision analysis: "the number of untrackable fragments ... from explosions ... constitutes an insignificant increase in the total number of objects in earth orbit and hence can be neglected in the calculation of collision probability".[53]

The first rocket body break-up occurred in 1961. Multiple other contributions to the debris population has occurred throughout the years including some hypothesized collisions, anti-satellite tests (ASAT), and the deployment of West Ford needles.[67] Micro-meteoroids and orbital debris (MMOD) were considered enough of a threat to include shielding on manned missions like Skylab however the shielding was for very small MMOD. Due to the increasing debris population, a small group of people began characterizing the environment, and in 1978, Cour-Palais and Kessler published their landmark paper[39] describing the likely 'debris cascade effect'. Understanding the debris environment was further fueled by the idea of creating a large, relatively permanent space station in orbit. The orbital debris program gained traction in NASA and was funded soon afterwards. By 1980, a Geosynchronous Earth Orbit (GEO) disposal method was also proposed.[67] Throughout the 1980s and 1990s further emphasis was placed on the growing orbital debris population by both NASA and the U.S. military. The first mitigation guidelines were outlined in

1992[1] prompting similar discussions in Russia and Europe. The creation of the Inter-Agency Space Debris Coordination Committee (IADC) and its efforts have helped to better formulate and summarize mitigation strategies that are in use today.[18]

In recent years, the creation of LEO debris has increased, largely due to two major catastrophic events: the Fengyun 1C ASAT test[60] that created over 3300 objects[38] and the Cosmos-Iridium collision[37] that created over 1700 objects.[61] This collision has helped to demonstrate that the debris cascade effect, first predicted by Kessler and Cour-Palais in 1978,[39] is occurring. Further, environmental models developed at the NASA Johnson Space Center Orbital Debris Office have shown that the debris environment is unstable and will grow in size dramatically, especially for LEO.[48] As of 2008, there have been a total of 194 fragmentations[56] with over ten more fragmentations since 2008.[57,58]

1.1.1.2 Orbital Debris Mitigation

In order to reduce debris creation, mitigation techniques have been employed. The primary debris mitigation methods include captive spacecraft elements (i.e. captive bolts), passivation (dumping excess fuel and shorting batteries), and demonstrating that all objects in LEO will deorbit within 25 years. These guidelines have been adopted by many nations (those in the IADC), however, adherence to these methods is not universal or consistently practiced.

Still, there has been a lot of evidence that mitigation methods are important to controlling the growth of space debris. Ruediger Jehn, from the European Space Agency (ESA), has demonstrated that mitigating both large and small sources of debris is effective at reducing the overall population. Figure 1.3 shows that there will be significant increases in the number of large, damaging debris objects if current practices are continued. The use of mitigation techniques are shown to noticeably reduce the number of debris created. Passivation helps to stop break-ups, however, solid rocket motor (SRM) slag is a large contributor to the smaller debris diameters and therefore its prevention will more significantly reduce debris objects.

Similar to ESA's findings, NASA has shown that the "business as usual" approach will cause drastic increases to the number of debris in orbit. Figure 1.4 shows the expected number of large objects to grow for all orbital regimes where LEO experiences the most drastic growth. The NASA model in Figure 1.4

shows larger increases in the debris population than the ESA estimates due to the fact that information on the A-SAT and Cosmos-Iridium debris is included.

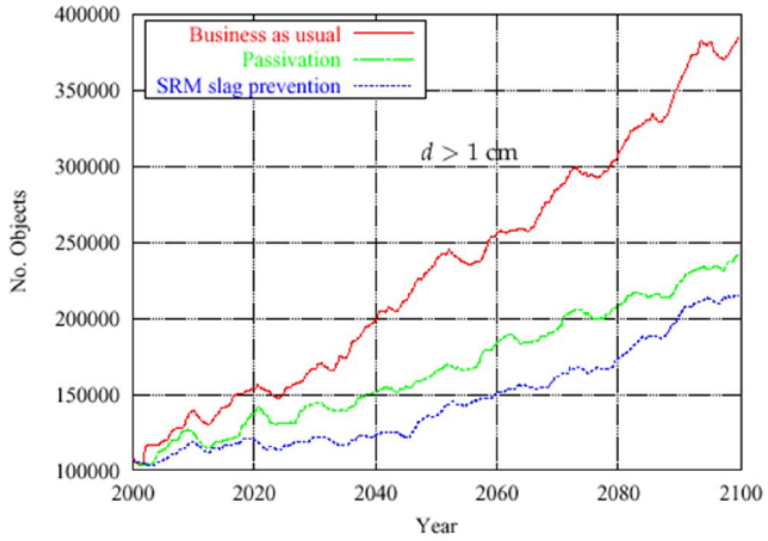

Figure 1.3: Mitigation Techniques: Impact of Passivation and SRM Slag Avoidance[35]

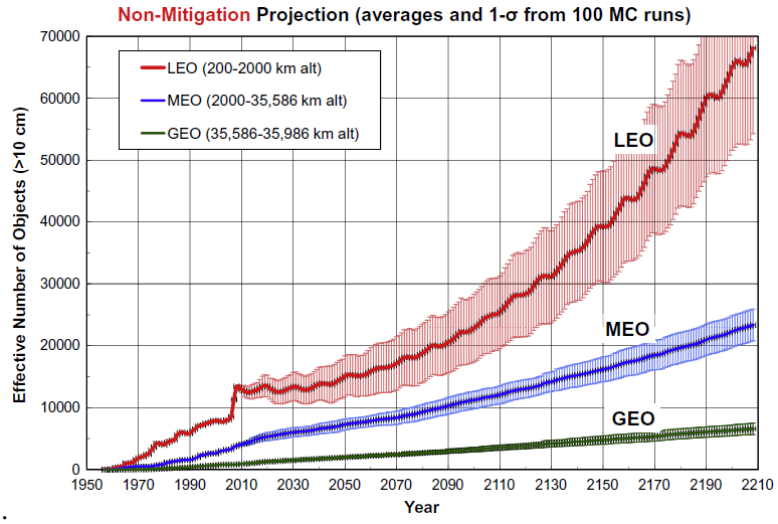

Figure 1.4: No Mitigation as Predicted by NASA's LEGEND[47]

When the time to deorbit a spacecraft after End of Mission is considered (Figure 1.5(a)), the debris environment and the number of collisions predicted change drastically. The "business as usual" plan, without

any artificially reduced spacecraft lifetimes, experiences large, non-linear growth in the number of collisions. This demonstrates that the behavior is unstable and will accelerate. Almost any deorbit time frame less than the natural lifetime of a spacecraft drastically reduces the number of collisions expected over the next 100 years. What is also interesting about Figure 1.5(a) is that the differences in number of collisions between 25 to 100 year deorbits are all about the same. The 0 or 10 year deorbit solutions reduce the number of collisions predicted in the next 100 years to about 10.

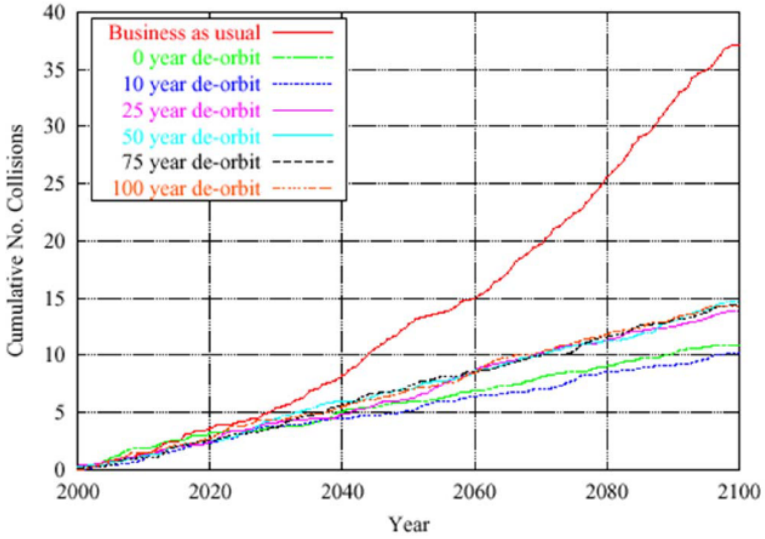

(a) Impact of Differing End of Mission Deorbiting Times.[35] ESA predictions

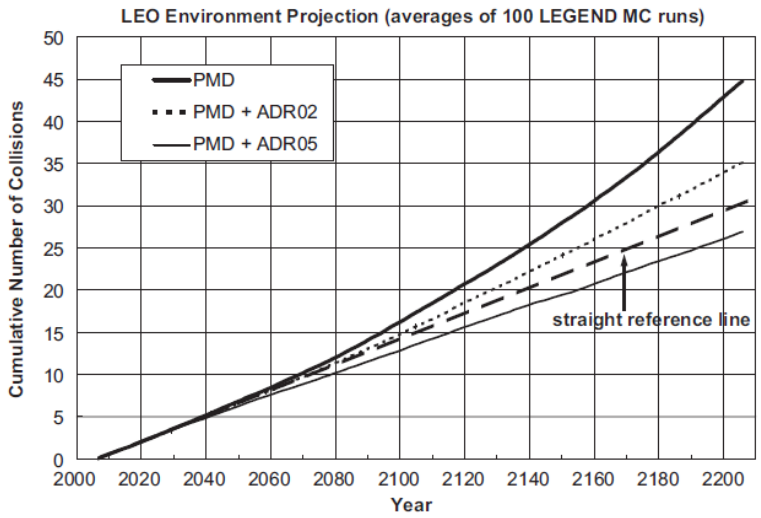

(b) Number of Collisions from Mitigation and ADR Predicted by NASA's LEGEND[49]

Figure 1.5: Expected number of future collisions due to debris

Figure 1.5(b) shows NASA's predictions of the number of collisions over the next 200 years. This plot differs from Figure 1.5(a) in that it considers disposal 25 years after End of Mission (for both rocket bodies and satellites, this occasionally includes moving to disposal orbits instead of deorbiting) as well as ADR. Still, similar trends can be seen between the two plots. First, collisions will occur in the future, even with aggressive mitigation and ADR measures. Second, both ESA and NASA models predict there to be about 15 collisions over the next 100 years when using 25 year End of Mission disposal practices (equivalent of the post mission disposal (PMD) line in Figure 1.5(b)). This shows that both models are predicting similar outcomes with the debris environment. Further, the use of current-day mitigation techniques alone will not stop the debris growth.

1.1.2 The Case for Active Debris Removal

Implementation of mitigation practices for on-orbit spacecraft have been shown to be effective at reducing debris growth in orbit. Both ESA and NASA predictive models seem to agree on this result. However, it has also been shown that mitigation only slows the growth of debris, it does not stop it. Because proper mitigation standards are not always followed, the effectiveness of the methods (Figure 1.3 and Figure 1.5(a)) are reduced. Looking at the number of break-up events from 1961 to 1998[67] and comparing them to the total number of launches for each given year,[43] Figure 1.6 is obtained. There has been about an average of 146 launches per year from 1961 to 1998, however, the number of break-ups each year are shown in Figure 1.6 to be increasing. Note that this figure was produced by:

$$\text{Percent of Break-ups} = \frac{\text{Number of Recorded Break-ups for Year X}}{\text{Number of Launches in Year X}} \text{ x } 100$$

The break-up events are from mostly old but some newer satellites (that should be practicing mitigation techniques). This demonstrates that mitigation is not a perfect method and another, more aggressive option might need to be considered because the number of break-ups have not been reduced during this time frame.

Active debris removal (ADR) is the next step, above and beyond mitigation, to reduce orbital debris. NASA's Orbital Debris Office has shown that removing 5 large objects from orbit a year,[49] while achieving 90% PMD with all future launches will stop the debris growth in LEO. Figure 1.1.2 demonstrates this

aggressive approach's effectiveness over the next 200 years. Thus, it is obvious that ADR, in combination with the common use of mitigation methods, are pivotal to controlling the LEO debris population.

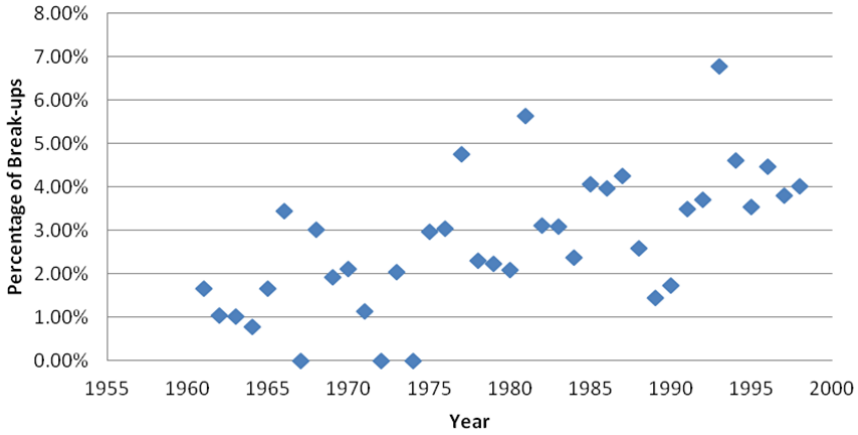

..

Figure 1.6: Percentage of All Observed Breakups Compared to the Number of Launches in a Given Year

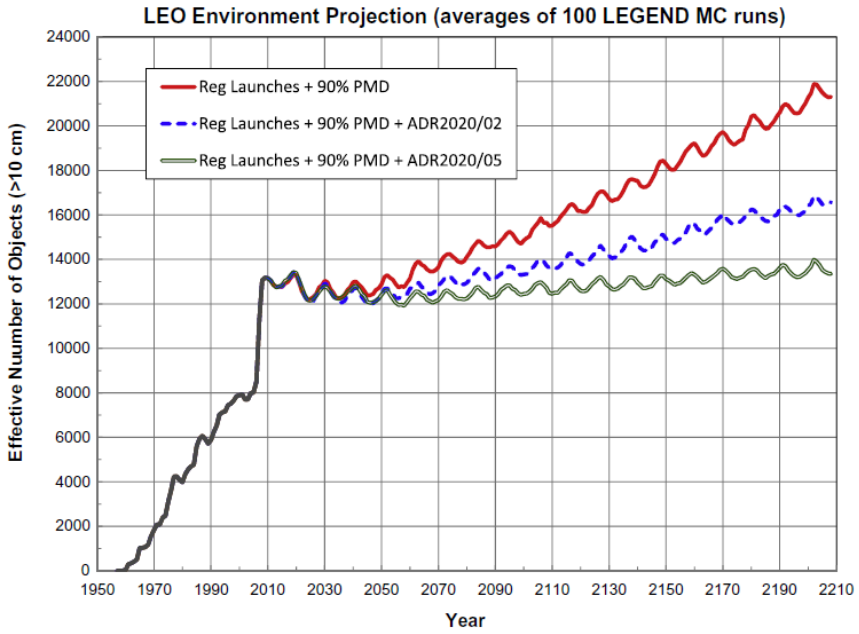

Figure 1.7: Mitigation and ADR Estimates for Improving LEO Debris Populations[47]

Unfortunately, the scenario presented in Figure 1.1.2 may be in many ways optimistic. The model used to obtain the figures assumes that 90% of all satellites and rocket bodies deorbit in 25 years, something

that is not achieved today. Further, the models assume that ADR will start in 2020. This is only 6 years away and the current economic and political environment may likely push this date back, which reduces some of the effectiveness of ADR.[47] (Dr. Liou also looked at how ADR will behave if it does not start until 2060 and found that it is still quite effective, but there does appear to be growth in the LEO population, unlike the 2020 start.) These results also assume that the rate of launches does not increase over the next 200 years, which can be very variable. Finally, this model assumes that no further A-SAT tests will occur. It is therefore likely that, for a multitude of reasons, ADR will not be as effective as described in Figure 1.1.2. It may also require that more than just 5 objects per year are deorbited to achieve the same reduction in the debris environment. All of these facts demonstrate a pressing need for ADR technology development so that if, and when, ADR is needed, it will be available.

1.1.3 Challenges for Active Debris Removal

The process of active debris removal creates many old and new challenges. Because ADR is defined by using an active craft to maneuver a debris object, several key events must occur: identification and tracking of the debris, rendezvous, uncooperative docking, and execution of removal operations. In LEO, tracking is a continuous process, most notably performed by the U.S. Air Force's Joint Space Operations Center (JSpOC). Still, this process is not always perfect and the locations of tracked objects can have significant error bounds. Identification of the most hazardous debris is also necessary and the classification of how they are hazardous can vary. If debris can be accurately tracked and identified as sufficiently hazardous, an ADR system can focus on that particular object.

After launching into orbit, the ADR system will then have to rendezvous with the debris object. While rendezvous has occurred on a variety of manned missions, it is less practiced for unmanned and autonomous vehicles in orbit. A multitude of studies have been done to address this issue and it is an active area of research.[25,55,64,65,85,93] Uncooperative docking is also an active area of research and requires continued development to be useful for on-orbit implementation[86,91,92]

Finally, once the ADR system has rendezvoused and docked with the debris, it will need to properly maneuver the debris to a disposal orbit. For LEO, this means an orbit that will decay within 25 years or a

direct reentry into the atmosphere. All of these technologies will either need to be improved or created to function properly for ADR.

1.2 Tethered - Tug Concept: Prospects and Challenges

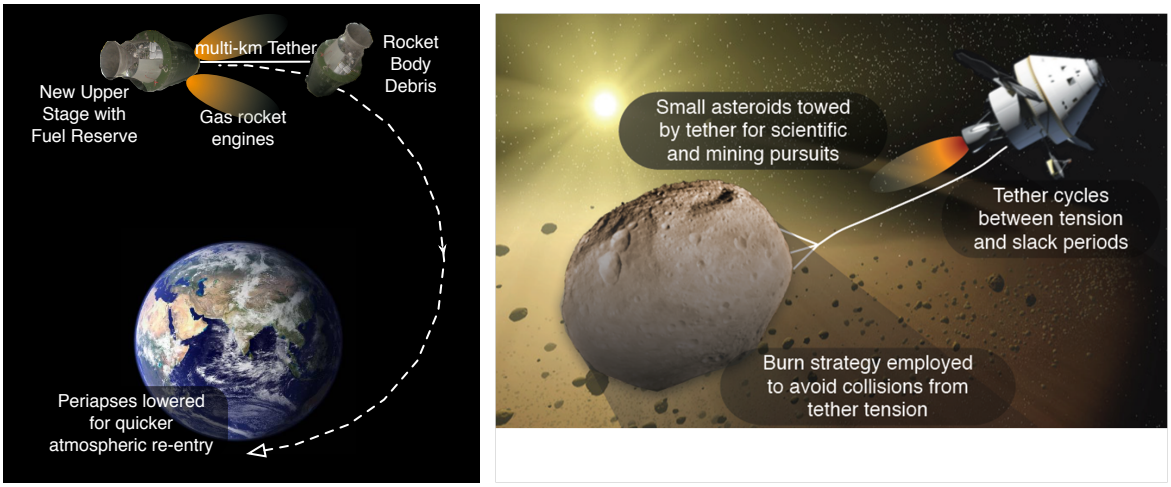

(a) Tethered ADR concept with rocket bodies

(b) Tethered Tug with a small asteroid

Figure 1.8: Examples of tethered tug concepts

1.2.1 System Description

LEO ADR translates technically into changing debris' orbital momentum to lower their periapses. Some proposed ADR methods[2, 10, 34, 69, 70, 87] utilize harpoons, mechanical grapples, or nets to grab the debris object. This is done so that the active tugging system does not need to directly interface with large, tumbling debris which could be a dangerous process. While the study of the debris capture system is beyond the scope of this research, all of these methods are likely to use tethers to connect the debris to the ADR craft. Tethers are a very efficient way to change the orbital momentum of on-orbit objects.

This research considers a specific engineering solution to ADR. The proposed concept is a mechanical debris towing system, shown in Figure 1.8(a). The concept uses a tether with one end attached to a vehicle with thrusting capabilities, known as the tug. The other end of the tether is attached to the debris object.

A tethered tug system could also be utilized for missions other than ADR, as shown in Figure 1.8(b).

The basic principles and dynamics correspond to satellite servicing or even asteroid towing. For satellite servicing, the towing vehicle could maneuver the target object to a desired orbit. NASA also has many plans to retrieve an asteroid as described in the NASA FY2014 Complete Budget[2] . There have been studies[23] of mission concepts to bring a small asteroid near to Earth for further investigation and resource harvesting. Earth protection from asteroid collisions has been a recent topic of discussion. Towing asteroids may be applicable to moving asteroids that may impact Earth.[24,51] A tethered system could be utilized for these mission plans.

Returning to ADR, one ideal model for this system is for the tug to be a rocket that is assumed to have deployed its payload and completed its primary mission.[50] Its secondary mission goal is to use the remaining fuel reserves to rendezvous with a debris object of similar orbital parameters. After attaching a tether to the debris object, the tug thrusts, lowering the periapsis of both objects. The general concept, originally developed by Dr. Trushlyakov from Omsk State University and shown in Figure 1.8(a), will change the periapsis so that drag forces cause both objects to deorbit within 25 years. Depending upon initial starting altitude and amount of reserve fuel available to the active upper stage, the debris-tug system could be deorbited within half an orbit (direct re-entry).[34,50,87]

This concept is advantageous because it utilizes a rocket that is already going to fly and deliver a satellite to orbit. Therefore this launch is not solely for the ADR mission. Further, it is likely that the rocket's payload will require an orbit in which many debris objects are already orbiting. Figure 1.2.1 shows high-priority targets for ADR, and many of them are in heavily used orbits. These orbits are likely locations for the launch vehicle/tug to fly to. It is therefore probable that the tug will be relatively close to debris that is most important to remove from orbit. The tethered-tug debris architecture provides a cost-effective ADR system because it deorbits two pieces of potential debris for each mission from orbits that are the highest in debris density.

Any tethered tug system, independent of mission, presents challenging rotational and translational dynamics and control behavior. Tethers have not been used or studied in a high force, high thrust environment. Some of the top-level challenges include:

[2] http://www.nasa.gov/news/budget/index.html

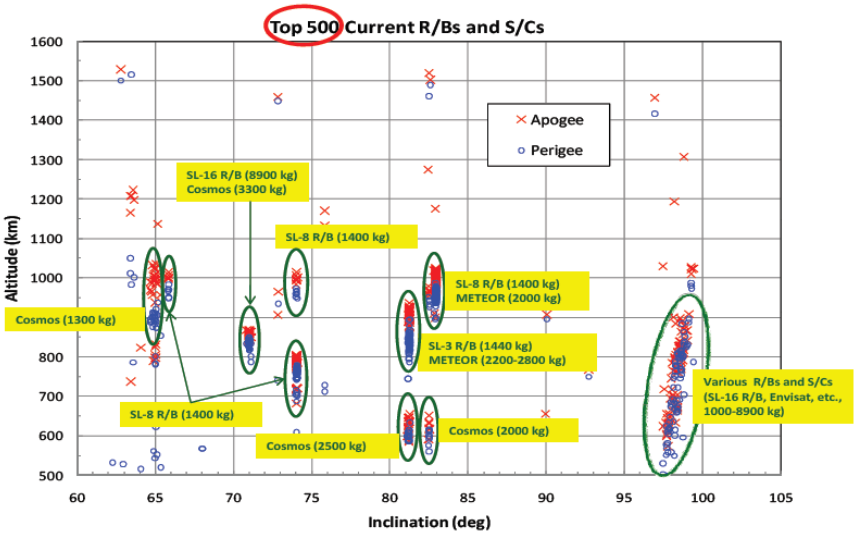

Figure 1.9: Top 500 Objects for ADR[47]

- Collision avoidance between end masses
- Understanding the system's translational and rotational motion
- Starting the thrust maneuver with a slack tether, causing whipping
- Unintentionally inducing rotational motion caused by off-centered tether attachment location
- Uncertainty in the system properties, such as debris mass

1.2.2 Motivation of Research

Rendezvous and attaching to debris receives a lot of research attention. While rendezvous and uncooperative docking remain challenging topics, all these studies consider the process of ADR 'completed' once docking has occurred. This thesis considers the research niche that is not studied: what to do with debris after capturing it. Again, since many capture concepts explicitly, or implicitly, use tethers, it makes sense to study how to perform maneuvers with a tethered system.

The tethered-tug concept requires study of a tethered system with two large end bodies. The flexing motion and modes of the tether itself are of interest to determine how it interacts with the large end masses.

Simulations are run in deep space and on-orbit environments. Deep space simulations allow for a detailed analysis on how idealized input shaping controls impact the post-burn relative motion, without the complication of orbital motion and perturbations. This allows for the post-burn dynamics to be studied subject to unknown debris mass properties and considering unmodeled higher order tether modes. Deep space is also applicable to asteroid retrieval as differential gravity is essentially negligible for close objects in such large heliocentric orbits. On-orbit simulations are conducted to determine flight-like behavior of the system and verify that control methods utilized produce desirable behavior for the ADR scenario.

Tethers have been studied and developed for years. However, little work has been performed in exploring their possible use as a towing mechanism and more effort is required in the study of tether-to-rigid body dynamics. Further, towing will generally induce large forces on the tether creating challenging thrust and post-thrust system dynamics. Tethers behave in a non-linear manner because they only apply a force while in tension. They are also very sensitive to whipping due to the sudden onset of a tension force. The challenging environments and dynamics that a tethered towing system must operate in, thus, require more detailed analysis.

The system is represented with large rigid body end masses and a lumped mass model of the tether is used (Chapter 2.2). Because this research focuses on the end body response, and is not a detailed analysis of the tether motion, the lumped mass model is acceptable. The lumped mass model still allows for nonlinear tether deflections to occur, along with higher order flexible tether modes and the simulation of slack tether behavior. Since the lumped mass model captures all of these behaviors, it provides an effective means to study tethered towing.

1.3 Literature Review

1.3.1 Active Debris Removal Related Research

There are numerous studies that relate to ADR and the technologies required for ADR. There are several primary avenues of study that relate to an ADR mission: rendezvous, on-orbit servicing, and capture. These research areas have huge bodies of work but the literature review focuses on studies that are relevant

to this dissertation.

One of the most difficult phases of an ADR mission will be the capture of debris. The most obvious method is to have the towing vehicle approach and mechanically dock to the object in question. Docking with the target vehicle has merit because it has been demonstrated many times. The basic principles behind this process have been around since Gemini[12] and have been practiced many times since in the world of human spaceflight. The Russian Progress vehicle has been used very successfully for rendezvous and docking for several decades on Mir and Salyut[3] . International Space Station servicing also has led to continued development in these processes with a multitude of vehicles such as Astrium's Automated Transfer Vehicle (ATV), Orbital Sciences' Cygnus module along with SpaceX's Dragon capsule and, again, the Russian Progress module. Several on-orbit missions have pushed the boundaries of this process by taking the human out of the loop. Specifically, Defense Advanced Research Projects Agency's (DARPA) Orbital Express[25] is a mission that demonstrated rendezvous, docking, and on-orbit servicing in 2007. MIT's SPHERES[55] program, and the Air Force's XSS-11[93] have also conducted autonomous rendezvous and docking on-orbit.

Unfortunately, the majority of these programs consider cooperative rendezvous and docking. Debris rotation rates can vary widely but may generally be on the order of a few degrees per second[68] for objects that have been on orbit for several years. This provides very challenging docking requirements on an ADR mission to not only dock but slow the rotation of the debris in order to perform maneuvers. Further, approaching a tumbling object adds extra risk to the tug vehicle. This has promoted the study of new technologies and methods for keeping the tow separated from the debris.

Many of these concepts are creating exciting technology developments. Several concepts propose touch-less force application such as ion-beam thrusting on the debris,[9] or electrostatic towing.[73] A large number of mechanical systems are also proposed such as grappling with an actuated 'arm', nets, and harpoons. Astrium is developing some of the most promising mechanisms that have undergone some testing. Figure 1.10 demonstrates several of these.

The net capture concept,[70] Figure 1.10(a), literally deploys a net around the object of interest. A net is attractive because it provides distributed loading to the debris when a maneuver is performed. Nets

[3] http://www.astronautix.com/craft/progress.htm

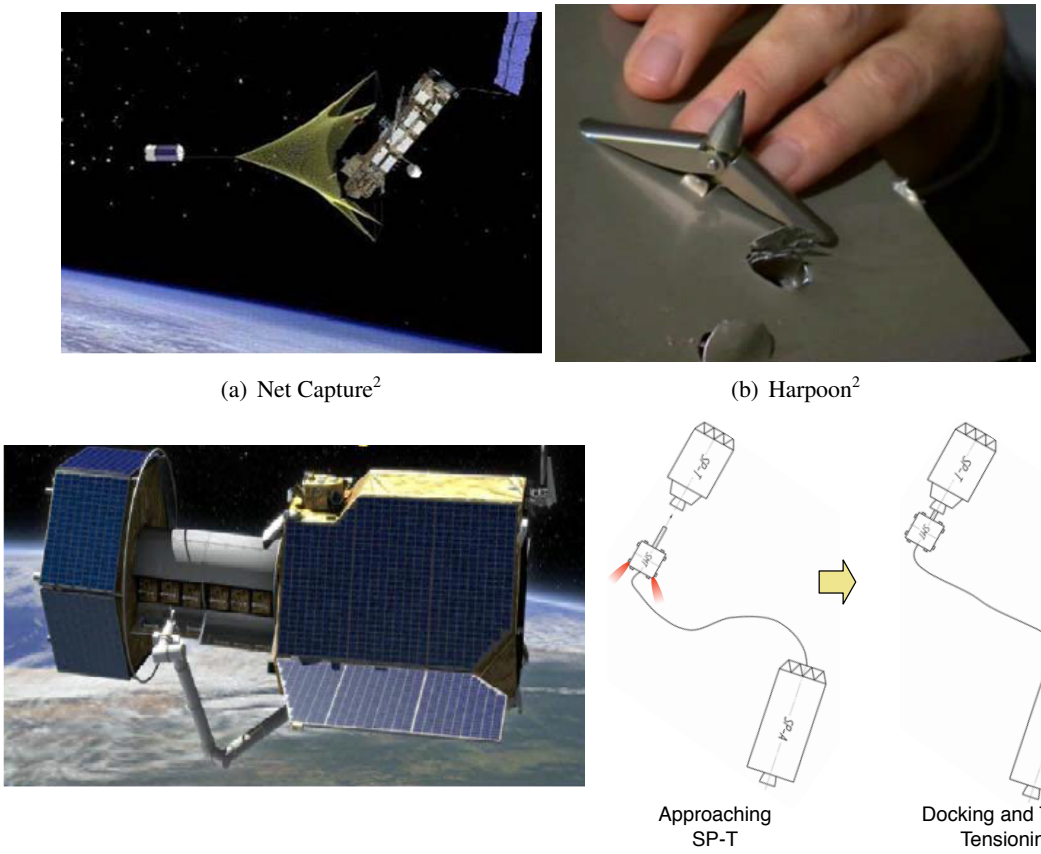

(a) Net Capture[2] (b) Harpoon[2]

(c) Grappling Arm[2] (d) Mini-capture vehicle[34]

Figure 1.10: Debris Capture Concepts

also have the advantage of ensnaring appendages of the debris, such as solar panels. Finally, nets do allow for the debris to have some rotational motion and could provide rotation damping as well, depending upon the towing strategy and the net properties. The net concept has been tested in micro-gravity flights and in vacuum deployments, making their technical readiness level relatively high compared to most debris capture systems. Very recent work has considered how a net capture may actually perform on orbit and how the system behaves once maneuvered with a tether-net.[8] The study by Benvenuto et. al.[8] is directly related to the research performed in this thesis and provides a good external verification that the dynamics seen are very similar to what is presented in following chapters. Still, net capture technology requires further study and testing because net orbital dynamics are challenging and the ability to capture a tumbling object without breaking appendages is a concern.

Harpooning debris may also provide a reasonable capture mechanism,[69] shown in Figure 1.10(b). The tested harpoon systems have been shown to penetrate various surfaces and can withstand large loads, such as thrust loads that would be applied by the tethered-tug system. Harpoons also allow for separation distance between the tug and debris, increasing safety. Finally, harpoons can also can operate properly even with debris rotation, making them an attractive design.

Finally, there are grappling devices designed to grip the debris, while maintaining some distance from the tug. These systems fall into two main categories: arms (Figure 1.10(c)) and mini-capture vehicles (Figure 1.10(d)). Arms allow for articulated capture of an object on the debris. Arms also make it easier for manipulation of the debris once capture has occurred. The mini-capture vehicle has a mechanism that interfaces with spent rocket nozzles[87] attached to a tether. These systems allow for potentially more secure attachment to the debris, but encounter many of the issues of uncooperative docking. Provided the mini-capture vehicle can attach to the debris, it does allow for spin rates while keeping the tug safely at a distance due to the tether.

In a separate proposed ADR mission concept by CNES (the French space agency), it was envisioned that towing debris through the use of a tether could be very effective.[10] The tether would be tolerant to center of gravity offsets, fuel sloshing, and any other challenging dynamic response from debris. The study also identifies that a Soyuz vehicle, or similarly large launch vehicle, would be required for an ADR mission. These independent conclusions plus the frequent use of tethers in the net, harpoon and mini-capture vehicle concepts provide motivation for the study of the tethered-tug concept.

The original tethered-tug concept was developed by Dr. Valery Trushlyakov and explored in the papers "The Use of Adapted Upper Stages for the Removal of Satellite and Rocket Body Debris from Unstable Orbital Regions"[50] and "Tethered Tug for Large LEO Debris Removal".[34] The second paper by Jasper, Seubert, Schaub, Trushlyakov and Yutkin, provided the first analysis of towing in space. This paper originally considered the use of the mini-capture vehicle, but nets or tethers may be just as effective. The research has since expanded to include the work recorded in this thesis.

1.3.2 Previous Tether Research

Space tether applications have been studied for years[13,15,36] and have shown promise. Space tethers also have flight heritage with several space shuttle missions and the Small Expendable Deployer System (SEDS)[14] missions which demonstrated a tether deployment of 20 kilometers and closed-loop tether deployment. However, these missions have been preliminary demonstration missions and have not executed many of the tasks required by ADR and towing. Tether applications still require extensive study because of the limited scope to these missions. (It is interesting to note that the first SEDS payload had its tether severed by debris.[67] This originally made the prospect of using tethers appear doubtful due to an apparently high collision probability. However, numerous on-orbit tethered missions have flown since SEDS and not experienced a debris hit, therefore making the probably of collision much lower than originally expected, although it is not negligible.[5,6,62])

The analysis of tethered systems (also known as Tethered Systems in Space or TSS) is often broken into three models to describe tether motion: continuum, finite element, and discrete mass models.[90] Continuum models usually consider partial differential equations and the solutions to these are either impossible to analytically solve or beyond the scope of this research. Finite element models (FEM) can produce high-accuracy results, however their proper implementation can be difficult and FEM is generally computationally intensive. This research focuses on the gross behavior of large end bodies attached through a space tether which can be adequately described with a discrete mass model.

Discrete mass, or lumped mass, models are used frequently. Reference 40 creates a discrete mass model to describe a distributed, tethered infrared telescope. Their system differs from the tethered-tug because it is a rotating, variable tether length system. Further, the model only considers small point masses on the ends of the tethers. The tethered-tug research considers a very different formation with rigid body end masses, providing different, challenging dynamics. Williams[90] provides a very similar discrete mass model to what is used within this thesis research, however Williams' tether is designed as a space elevator anchored to the Earth. The towing system explored here focuses on tether lengths that are much smaller with vastly different end mass behavior. Tethers have been used underwater for years, and there are even similar discrete

mass models developed for these underwater tethers.[11,20,21] However buoyancy, surface wave motion, and other environmental inputs create different dynamics. The model developed for this research is capable of modeling higher-order tether modes while capturing large rigid end body motion on both ends of the tether. Further, the model focuses on towing large bodies, something that has not been studied.

Electrodynamic tethers are often proposed for ADR concepts and they have been studied extensively.[40,63,89] Electrodynamic tethers rely on using differential charging along the tether to create an electron flow, creating a magnetic field that can be controlled to change orbital altitude through the Lorentz force. While this technology is promising, it operates in a fundamentally different way from the tethered-tug concept by utilizing the Earth's magnetic field, instead of towing debris with chemical propulsion. Further, electrodynamic tethers operate in significantly lower force environments and are therefore not directly applicable to this research.

In the past, tethers have been considered as a mechanism for changing a satellite's orbit, like the tethered-tug system is required to do. Various concepts use tethers for momentum exchange where tethered end masses spin about the system's center of gravity. One of the masses is then released and thrown into a different, desired orbit. The concepts generally look at LEO to GTO or lunar injection orbits.[16,28,29,83] While these concepts generally consider relatively large force environments, 'momentum exchange' is different than the tethered-tug premise. With a momentum exchange device, in order to conserve momentum, as one object is thrown into a higher orbit, the other object is thrown to a lower orbit. This is specifically not desirable for an ADR system since both objects should ideally be removed from orbit. Further, these studies generally do not consider slack tethers, something that is a reality for the towing architecture.

1.4 Research Intent

1.4.1 Goals

The goal of this research is to describe and control the motion of the tether-tug system while avoiding collisions between the end masses. The primary fundamental questions are:

(1) How does a tether interact with rigid masses on both ends after a large thrust maneuver?

(2) Can the potential for collisions between end bodies be reduced through open-loop control shaping?

(3) How does variability in tether and debris properties affect performance to lower periapses?

(4) What motions and orientations occur between the end masses because of input shaping?

(5) If a tether is slack before thrusting, does it severely increase collision potential?

Investigating the fundamental questions help to determine if tethered towing is actually a safe and viable option for ADR, satellite servicing or asteroid retrieval. This research focuses on the end mass and tether dynamics and control. The process and mechanism by which the tether attaches to the debris (or functioning satellite or asteroid) is not considered due to the significant and unique challenges docking presents.

The specific research goals are as follows:

- *Research Goal 1*: Model the rigid body-to-tether interaction
- *Research Goal 2*: Examine the tether system's ideal motion with a taut tether and an aligned CG-to-tether attachment point
- *Research Goal 3*: Investigate the tether system's non-ideal motion with a slack tether and an offset CG-to-tether attachment point

Goal 1 focuses on analytic and numerical model development of the tethered-tug system. Goal 2 is used not only to study the behavior, but to develop input-shaped controls to properly maneuver the system and explore tether properties. Goal 3 looks at how the system and controls behave in more realistic and challenging conditions.

1.4.2 Scope

The research comprising this thesis is heavily focused in astrodynamics and will consist of computer simulation-based studies. While the tether plays a significant role in the system behavior, much of the focus is placed on the end body motion as opposed to the tether. This is because the end bodies are much more

massive and capable of creating debris. The purpose of this system is to maneuver both objects without causing a collision, thus performance is based upon end body behavior.

A constraint is placed on the system throughout the dissertation, that the end bodies shall not collide. This is a conservative approach to avoiding debris creation because the relative velocities between the end bodies will generally be small. It is unlikely low velocity end body collisions will have enough energy to produce additional debris. Further, if a collision occurs after the periapsis lowering maneuver is performed, the entire system has a lowered lifetime, including any debris caused by an end body collision.

It is assumed that the maneuver does not cause a direct re-entry of both objects. A direct re-entry simplifies much of the behavior because there is not enough time to see much interaction of the system components before they burn up. Long duration behavior is not considered primarily because focus is placed on *how* to maneuver the system instead of behavior after months or years.

Rendezvous and docking/attachment are their own, unique challenges that are actively being researched. It is assumed that these processes have already occurred and the system is ready for further maneuvering.

Finally, the economic and political challenges associated with this system, and ADR in general, will not be addressed. There are tremendous hurdles to be overcome in both these areas before ADR can become a reality.[4,31,52,75] The author has had many conversations with a variety of people in the community about these challenges and while the topic is of interest, this discussion does not concisely fit into the thesis. It can be said though, that there is an aversion to funding ADR systems due to the fact that they can easily be considered weapons systems. Further, there is still considerable debate among funding agencies and policy makers that ADR is necessary (versus continued mitigation). Clearly, these are complicated issues that require their own contemplation and, again, are not addressed beyond this point.

1.4.3 Contributions

The work in this thesis has been collected from these publishings on the tethered-tug system:

- L. E. Z. Jasper and H. Schaub, "Tether Design Considerations for Large Thrust Debris De-orbit Burns," AAS/AIAA Spaceflight Mechanics Meeting, Santa Fe, New Mexico, January 26-30, 2014.

- L. E. Z. Jasper and H. Schaub, "Discretized Input Shaping for a Large Thrust Tethered Debris Object," AAS/AIAA Spaceflight Mechanics Meeting, Santa Fe, New Mexico, January 26-30, 2014.
- L. E. Z. Jasper and H. Schaub, "Input Shaped Large Thrust Maneuver with a Tethered Debris Object," Acta Astronautica, Vol 96, March - April 2014, pp. 128 - 137.
- Lee E. Z. Jasper and Hanspeter Schaub, "Input Shaped Large Thrust Maneuver with a Tethered Debris Object," 6th European Conference on Space Debris, Darmstadt, Germany, April 22 - 25, 2013.
- L. E. Z. Jasper, C. R. Seubert, H. Schaub, T. Valery and E. Yutkin, "Tethered Tug for Large LEO Debris Removal," AAS Spaceflight Mechanics Meeting, Charleston, January 29 - February 2, 2012. Paper No. AAS 12-252.
- L. E. Z. Jasper, H. Schaub, "Discretized Input Shaping for a Large Thrust Tethered Debris Object," In preparation.

Other publishings related to orbital debris research, but not specifically concerning the tethered-tug concept, and therefore not addressed in this thesis:

- H. Schaub and L. E. Z. Jasper, "Circular Orbit Radius Control Using Electrostatic Actuation for 2-Craft Configurations," AAS/AIAA Astrodynamics Specialist Conference, Girdwood, Alaska, July 31 - August 4, 2011. Paper No. AAS 11-498.
- L. E. Z. Jasper and H. Schaub, "Effective Sphere Modeling for Electrostatic Forces on a Three-Dimensional Spacecraft Shape," AAS/AIAA Astrodynamics Specialist Conference, Girdwood, Alaska, July 31 - August 4, 2011. Paper No. AAS 11-465.
- H. Schaub and L. E. Z. Jasper, "Orbit Boosting Maneuvers for 2-Craft Coulomb Formations," AIAA Journal of Guidance, Control and Dynamics, Vol. 36, No. 1, Jan.-March 2013, pp. 74-82.
- Jasper, L. E. Z. and Schaub, H., "Effective Sphere Modeling for Electrostatic Forces on Three-Dimensional Spacecraft Shapes," Adventures on the Interface of Mechanics and Control, K. T.

Alfriend, M. Akella, J. E. Hurtado, J. Juang, and J. D. Turner, Tech Science Press, Duluth, Georgia, 2012, pp. 267-298.

- L. E. Z. Jasper, P. Anderson and H. Schaub, "Economic and Risk Challenges of Operating in the Current Space Debris Environment," Submitted to 3rd workshop on Space Debris Modeling and Remediation in Paris, CNES-HW, Paris, France, June 16-18, 2014

- L. E. Z. Jasper, P. Anderson and H. Schaub, "Cost and risk assessment for spacecraft operation decisions caused by the space debris environment," Submitted to the 65th International Astronautical Congress, Toronto, Canada, Sept. 29 - Oct. 3, 2014.

1.5 Thesis Outline

The thesis is organized into 6 chapters. While the first chapter gives introductory material and motivation for the research, the remaining chapters describe the results from the research. Chapter 2 describes the model and simulation software used for this research. Chapter 3 describes the control methods devised for the tethered-tug system and their performance. Variability of the system due to changes to tether properties is explored in Chapter 4. A high-level description of the tether design space is identified given desirable system behavior. Next, Chapter 5 demonstrates the losses of performance due to a slack tether prior to maneuvering, and induced rotations in the end bodies. Finally, Chapter 6 ends the thesis by providing the final conclusions in Chapter 6.1 and Chapter 6.2 highlights possible continuations of this research.

Chapter 2

Modeling the Rigid Body-to-Tether Interaction

The tether system model and simulation software is described in this chapter. First, a brief explanation of the simulation is given, describing its capabilities. Next, the tether model is described, analyzed, and verified. Finally, the concept's parameters, such as masses considered, are given.

2.1 Simulation Software Architecture

The simulation software is designed to model orbital and attitude motion of rigid bodies. It is written in C as was originally made for Coulomb Structure research.[72,76] However, it has been modified for tethered-tug analysis. The software is based upon inertial propagation of all bodies. Because all accelerations are applied in the inertial frame (Earth centered), there are no truncations or linearizations applied to the forces used. It should be emphasized that while Section 2.2 discusses the tether model and linearizes it for analysis, the software does *not* linearize the dynamics, allowing for full 3 degree-of-freedom motion. Again, the software also models rigid body motion allowing for attitude dynamics to be studied. However, bodies can be specified as point masses making their radii zero, effectively removing inertia, attitude, and rotation rate dependences.

The simulation can model multiple types of forces. Gravitational forces include two-body, as well as J_2 - J_6 gravity harmonics. Of course tether forces are also applied, only while the tether is in tension. The model is also capable of accounting for Electrostatic/Coulomb forces and Solar Radiation Pressure. These forces are not used in this thesis. Finally, control inputs are also allowed giving the user the ability to apply torques and forces to any craft/body simulated. Any of these forces can be enabled or disabled, allowing for

various environments to be considered, like deep space where the gravitational parameter is zero.

The integrator used is a Runge-Kutta 4-5 method with both fixed and variable step sizes. This was originally chosen for the Coulomb Structure research however it is sufficient for the dynamics present in this thesis. Section 2.2.3 further describes verification of the simulation and the modifications made to it for this research.

2.2 Tethered-Tug System Model

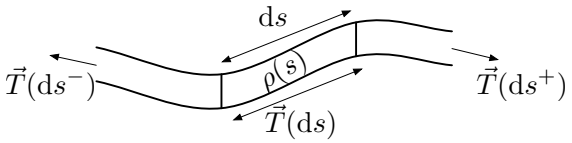

Figure 2.1: Segment of a string model of a tether

To study the tethered-tug system, a model is necessary to capture tether motion and rigid end body motion. The first question to answer when conducting this research is to determine the tether model to be used. Modeling the tether as a string, as shown in Figure 2.1, can achieve high accuracy results. Eq. (2.1)[3] is the full partial differential equation for a string model of a tether:

$$\rho \frac{\partial^2 \boldsymbol{R}}{\partial t^2} = \frac{\partial \boldsymbol{T}}{\partial s} - \frac{\mu \rho \boldsymbol{R}}{R^3} + \boldsymbol{F} \tag{2.1}$$

where ρ is the density of a given element, $\boldsymbol{R}$ is the position vector of a given element, $\boldsymbol{T}$ is the tension force over the element, s is the distance along the tether, t is the time, μ is the Earth's gravitational constant, and $\boldsymbol{F}$ represents external forces. This is difficult to analytically solve and a Finite Element Model (FEM) is often used.

As described in Chapter 1.3 it is commonly accepted to remove the added complexity of using FEM solved string dynamics and to discretize the tether into lumped masses with visco-elastic spring forces between each. Because this research focuses on the end body response, instead of the specific tether dynamics, the lumped mass model is a reasonable approximation. The discretized mass model can be seen in Figure 2.2. Note that the end bodies are rigid, 6 degree-of-freedom (DOF) large bodies, and the tether masses

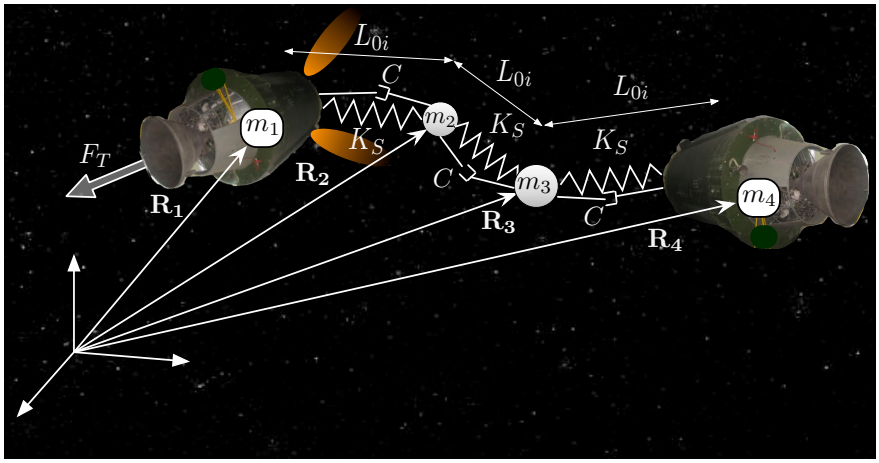

Figure 2.2: Discretized tether model example with 2 tether masses

are treated like point masses. The visco-elastic model is described in more detail in the following sections including its derivation, an Eigenvalue analysis, verification of the software, and a description of the two primary simulation types.

2.2.1 Equations of Motion

The tether model used approximates the tether as multiple lumped masses attached by visco-elastic (spring) forces to rigid end bodies. These end bodies have the ability to translate and rotate, and the lumped masses are considered point masses. The tether model is easily linearized and therefore well suited to linear, second order differential equation analysis, such as Eigenvalue (natural frequency) analysis. This section derives the equations of motion for the system.

2.2.1.1 Tether Equations of Motion

The tethered-tug system consists of a tow vehicle that can thrust, the object to be towed, and a tether between the two (Figure 1.8). The tug and the towed object are modeled as rigid bodies that can rotate and translate. The tether is discretized into multiple lumped point masses connected by visco-elastic forces, as shown in Figure 2.2.

The tether is made taut for many of the studies in this thesis because slack in the tether causes ampli-

fied responses, and whipping behavior. However, Chapter 5 does explore both initial slack in the tether and spinning end bodies. The tug has active attitude control while thrusting and all the thrust is applied in the in-track/along-track direction. The attitude control is turned off when the thruster is off.

Discretized mass models for tethers are commonly used.[11,20,21,40,90] However, none of these have considered the process of towing with a tether, in space, with similar end body sizes. The translational equations of motion, caused by the tether, for the system in Figure 2.2 can be expressed as

$$\begin{aligned}
\ddot{\boldsymbol{R}}_i &= \tfrac{1}{m_i}\left(K_S(|\boldsymbol{R}_{i+1}-\boldsymbol{R}_i|-L_{0,i})\hat{\boldsymbol{e}}_i + \tfrac{C}{L_0}(|\dot{\boldsymbol{R}}_{i+1}-\dot{\boldsymbol{R}}_i|)\hat{\boldsymbol{e}}_i\right)\\
\ddot{\boldsymbol{R}}_{i+1} &= \tfrac{1}{m_{i+1}}\left(K_S(|\boldsymbol{R}_{i+2}-\boldsymbol{R}_{i+1}|-L_{0,i+1})\hat{\boldsymbol{e}}_{i+1} + \tfrac{C}{L_0}(|\dot{\boldsymbol{R}}_{i+2}-\dot{\boldsymbol{R}}_{i+1}|)\hat{\boldsymbol{e}}_{i+1} - m_i\ddot{\boldsymbol{R}}_i\right)\\
&\vdots\\
\ddot{\boldsymbol{R}}_N &= \tfrac{1}{m_N}\left(-K_S(|\boldsymbol{R}_N-\boldsymbol{R}_{N-1}|-L_{0,N})\hat{\boldsymbol{e}}_{N-1} - \tfrac{C}{L_0}(|\dot{\boldsymbol{R}}_N-\dot{\boldsymbol{R}}_{N-1}|)\hat{\boldsymbol{e}}_{N-1}\right)
\end{aligned} \tag{2.2}$$

where N is the number of masses and $\hat{e}$ is the unit vector the tether force is applied along, defined as

$$\hat{\boldsymbol{e}}_i = \frac{\boldsymbol{R}_{i+1}-\boldsymbol{R}_i}{|\boldsymbol{R}_{i+1}-\boldsymbol{R}_i|} \tag{2.3}$$

$\boldsymbol{R}_i$ is the i^{th} mass's position, $L_{0,i}$ is the unstretched tether length of segment i, m_i is the mass, C is the damping coefficient, K_S is the spring constant, and L_0 is the total unstretched tether length. These are only part of the equations of motion used for the numerical simulation used in this thesis. Gravity and the thrust control acceleration are also present as well as the rigid body dynamics for the tug and debris. Thrust is also applied to the tug mass.

The natural frequency ω_n of the system can be found by taking the three-dimensional model in Figure 2.2 and simplifying it to a one-dimensional problem, as in Figure 2.3.

The separation between the bodies can now be expressed as

$$\begin{aligned}
L_i &= |\boldsymbol{R}_{i+1}-\boldsymbol{R}_i| - L_0\\
L_i &= x_{i+1}-x_i-L_0\\
\dot{L}_i &= \dot{x}_{i+1}-\dot{x}_i\\
\ddot{L}_i &= \ddot{x}_{i+1}-\ddot{x}_i
\end{aligned} \tag{2.4}$$

assuming all unstretched tether lengths, L_0, are the same. Using the one dimensional set-up in Eq. (2.4), the discrete mass model in a state space representation is given in Eq. (2.5). Here n is the number of links

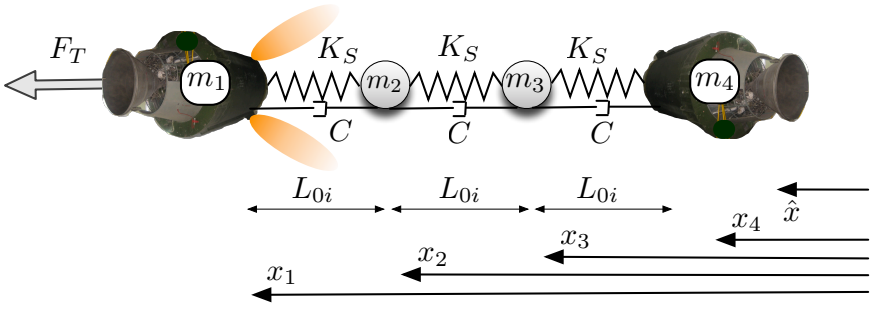

Figure 2.3: Discretized tether model example with 2 tether masses

between each mass. Therefore, if there are four masses ($N = 4$), there are three tether links and $n = 3$.

$$\dot{\boldsymbol{X}} = [A]\boldsymbol{X} + [B]\boldsymbol{u} \tag{2.5}$$

The variables in Eq. 2.5 are given below.

$$\boldsymbol{X}_{2n\times 1} = \begin{bmatrix} L_1 \\ \vdots \\ L_n \\ \dot{L}_1 \\ \vdots \\ \vdots \\ \dot{L}_n \end{bmatrix} \quad [B]_{2n\times 1} = \begin{bmatrix} 0 \\ \vdots \\ 0_n \\ 1 \\ 0_2 \\ \vdots \\ 0_n \end{bmatrix} \quad \boldsymbol{u} = \frac{F_T}{m_1}$$

F_T is the thrust force, applied only to m_1. The matrix $[A]$ can be broken up into four smaller matrices:

$$[A]_{2n\times 2n} = \begin{bmatrix} [0]_{n\times n} & [I]_{n\times n} \\ [A_{2,1}]_{n\times n} & [A_{2,2}]_{n\times n} \end{bmatrix}$$

The acceleration caused by the visco-elastic spring force is given in Eq. 2.6, which is entirely position dependent.

$$[A_{2,1}] = K_S[M] \tag{2.6}$$

with

$$[M] = \begin{bmatrix} -\frac{(m_i+m_{i+1})}{m_i m_{i+1}} & \frac{1}{m_{i+1}} & 0_{n-1} & \cdots & 0_n \\ \frac{1}{m_{i+1}} & -\frac{(m_{i+1}+m_{i+2})}{m_{i+1}m_{i+2}} & \frac{1}{m_{i+2}} & \ddots & \vdots \\ 0_{n-1} & \ddots & \ddots & \ddots & 0_{n-1} \\ \vdots & \ddots & \frac{1}{m_{n-1}} & -\frac{(m_{n-1}+m_n)}{m_{n-1}m_n} & \frac{1}{m_n} \\ 0_n & \cdots & 0_{n-1} & \frac{1}{m_n} & -\frac{(m_n+m_{n+1})}{m_n m_{n+1}} \end{bmatrix} \tag{2.7}$$

Again, m_i is each body's mass and the spring constant K_S is defined in Eq. (2.8).

$$K_S = \frac{EA}{L_0} \tag{2.8}$$

with units of $\frac{N}{m}$. Here L_0 is the initial, unstretched (equidistant) length of the tether between each mass, E is the Young's modulus of elasticity for the tether, and A is the cross sectional area of the tether. Because Eq. (2.5) models a tether as a spring, it is only active while the tether is in tension. When the separation distance is less than L_0, all spring and damping forces go to zero.

Without damping $[A_{2,2}] = [0]_{n\times n}$. Using a strain based damping model[90]

$$\epsilon_i = \frac{|\boldsymbol{R}_{i+1} - \boldsymbol{R}_i| - L_0}{L_0} = \frac{L_i}{L_0} \tag{2.9}$$

then the strain rate is

$$\dot{\epsilon}_i = \frac{\dot{L}_i}{L_0} \tag{2.10}$$

assuming L_0 is a constant. The force due to damping is then expressed as

$$\boldsymbol{F}_{Di} = C\dot{\epsilon}_i \hat{\boldsymbol{e}}_i \tag{2.11}$$

Here, C ($\frac{kg}{s}$) in Eq. (2.11) is the damping coefficient. With this linear damping model, $[A_{2,2}]$ becomes

$$[A_{2,2}] = \frac{C}{L_0}[M] \tag{2.12}$$

with $[M]$ from Eq. (2.7). This is also only correct while in tension. There is no damping present while the separation between two masses is less than L_0.

2.2.1.2 Rotational Motion Control of the Tug Vehicle

Because the tether can induce a torque and rotation on the thrusting body, a simple Lyapunov feedback control is developed to maintain the thrusting body's heading (and therefore the thrust) in the along-track direction. This control is only active while the thrust is on. The attitude feedback control is not the focus of this research and is only given for completeness. Other than the discussion in this section, the control is not analyzed for performance and the process by which this control could be applied is not considered.

The Lyapunov function, shown in Eq. (2.13), is positive definite and its derivative is negative definite if the constraint of $-\boldsymbol{\omega}^T[P]\boldsymbol{\omega}$ is used.[71]

$$V = \frac{1}{2}\boldsymbol{\omega}^T[I]\boldsymbol{\omega} + 2K_\sigma \ln(1 + \boldsymbol{\sigma}^T\boldsymbol{\sigma}) \tag{2.13}$$

Here, $\boldsymbol{\omega}$ is the angular velocity of the tug body, $\bar{\sigma}$ is the attitude, represented as Modified Rodriguez Parameters (MRPs), $[I]$ is the inertia of the tug, and K_σ is a positive scalar. This then leads to the control feedback torque in Eq. (2.14).

$$\boldsymbol{\tau}_c = \boldsymbol{\omega} \times [I]\boldsymbol{\omega} - [P]\boldsymbol{\omega} - K_\sigma\boldsymbol{\sigma} - \boldsymbol{\tau}_{ext} \tag{2.14}$$

In this expression, $[P]$ is a positive definite gain matrix, $\boldsymbol{\tau}_{ext}$ are external torques, and $\boldsymbol{\tau}_c$ are the control torques. Combining Eq. (2.13) and Eq. (2.14) produces the closed loop dynamics

$$\dot{\boldsymbol{\omega}} = [I]^{-1}(-[P]\boldsymbol{\omega} - K_\sigma\boldsymbol{\sigma} - \boldsymbol{\tau}_{ext}) \tag{2.15}$$

Here $\boldsymbol{\tau}_{ext}$ is considered to be zero because the external torques applied to the system are relatively small and have no major influence over the several minutes that the thrust occurs.

The gain values for $[P]$ and K_σ are computed using linear system theory as described in Reference 71. If $[P]$, K_σ and $[I]$ are assumed to be diagonal then the rotational dynamics for each axis can be written as

$$\begin{pmatrix} \dot{\sigma_i} \\ \dot{\omega_i} \end{pmatrix} = \begin{bmatrix} 0 & \frac{1}{4} \\ -\frac{K_\sigma}{I_i} & -\frac{P_i}{I_i} \end{bmatrix} \begin{pmatrix} \sigma_i \\ \omega_i \end{pmatrix}$$

where i is a particular rotational axis (1, 2, 3). From linear control theory, Eq. (2.15) will produce a natural frequency of

$$\omega_{ni} = \sqrt{\frac{K_\sigma}{4I_i}} \tag{2.16}$$

and a damping coefficient of

$$\zeta_i = \frac{P_i}{\sqrt{K_\sigma I_i}} \tag{2.17}$$

Because the first fundamental modes of the tether system are known from Eq. (2.22), Eq. (2.23) and Eq. (2.24), the gain K_σ should be chosen so that the rotational control does not excite the tether. Therefore Eq. (2.16) can be rewritten so that the gain can be selected given a natural frequency that is reasonably different from the tether modes.

$$K_\sigma = 4 I_i \omega_{ni}^2 \tag{2.18}$$

Similarly, the rotational control will be chosen to be critically damped. This results in $\zeta_i = 1$ or the gain selection of

$$P_i = \sqrt{K_{\sigma i} I_i} \tag{2.19}$$

Given the masses and the tether properties in Table 2.1 and the tether modes from the three body system in Eq. (2.24), the Eigen frequencies turn out to be 0.19 Hz and 3.43 Hz. Therefore, the rotational control should be chosen to not be near these values. Selecting $\omega_{ni} = 0.01\ Hz$ for all axes allows for the rotational control natural frequency to be over an order of magnitude slower than the tether modes. Using $\omega_{ni} = 0.01\ Hz$ Eq. (2.18) yields:

$$K_\sigma = 161 \tag{2.20}$$

and Eq. (2.19) yields

$$P = \begin{bmatrix} 1283 & 0 & 0 \\ 0 & 1283 & 0 \\ 0 & 0 & 673 \end{bmatrix} \tag{2.21}$$

2.2.2 Modal Analysis

There are four primary control types that have been considered for the tethered-tug system:

- Step input
- Notch Filter

- Posicast
- Bang-off-bang

The first, is a step input that thrusts in the along-track direction for the duration required to achieve a desired Δv. This is effective at changing the orbital parameters of the tug and debris but because it is a step input, all frequencies of tether are excited. This is undesirable as the collision potential between the objects is increased, along with larger tether tensions.

To reduce collision potential, other control methods are utilized to avoid collision between the end bodies. These control methods are designed to avoid exciting the natural modes of the tethered tug system. Most of the controls, therefore, require knowledge of the system's Eigenvalues. Thus, this section presents an example of the Eigenvalue analysis.

The other control types considered are open-loop input shaping on the thrust's step profile. These controls are further discussed in Chapter 3 however they include a continuous notch profile, and impulsive methods such as discrete, Posicast, and bang-off-bang profiles. The notch control[33] highly attenuates, in the frequency domain, undesirable modes of the tether system. The discrete control[32] is simply a discretization of the notch control. The Posicast control[32] properly times varying thrust amplitudes so that it does not excite the system. Finally, the bang-off-bang[32] control properly accelerates the masses so that there is little relative motion between the bodies during the maneuver.

Performing an Eigen value analysis on the system in Eq. (2.5), the fundamental mode of the system can be found. As an example, the Eigen-frequencies ω_d of a three body (single tether mass) system are found by solving for the roots of Eq. (2.22).

$$z_0 + z_1\omega_d + z_2\omega_d^2 + z_3\omega_d^3 + z_4\omega_d^4 = 0 \tag{2.22}$$

where

$$
\begin{aligned}
z_0 = &\quad K_S^2 m_1 + K_S^2 m_2 + K_S^2 m_3 \\
z_1 = &\quad 2CK_S m_1 + 2CK_S m_2 + 2CK_S m_3 \\
z_2 = &\quad C^2 m_1 + C^2 m_2 + C^2 m_3 + K_S m_1 m_2 + 2K_S m_1 m_3 + k m_2 m_3 \\
z_3 = &\quad C m_1 m_2 + 2C m_1 m_3 + C m_2 m_3 \\
z_4 = &\quad m_1 m_2 m_3
\end{aligned}
$$

The undamped natural frequencies (ω_n) can be found by setting $C = 0\ \frac{kg}{s}$. As an example, the Eigenvalues of two rigid bodies connected by a massless tether are:

$$
\omega_n = \begin{pmatrix} 0 \\ 0 \\ -\sqrt{\frac{K_S(m_1+m_2)}{m_1 m_2}} \\ \sqrt{\frac{K_S(m_1+m_2)}{m_1 m_2}} \end{pmatrix} \tag{2.23}
$$

The Eigen-frequencies ω_n of a three body (single tether mass) system are:

$$
\omega_n = \begin{pmatrix} 0 \\ 0 \\ \pm\sqrt{K_S Z_1 + K_S Z_2} \\ \pm\sqrt{K_S Z_3 + K_S Z_4} \end{pmatrix} \tag{2.24}
$$

where

$$
\begin{aligned}
Z_1 = &\quad \frac{(m_2 m_3 + m_1(m_2+2m_3))}{2m_1 m_2 m_3} \\
Z_2 = &\quad \frac{\sqrt{m_1^2 m_2^2 - 2m_1 m_2^2 m_3 + (4m_1^2 + m_2^2) m_3^2}}{2m_1 m_2 m_3} \\
Z_3 = &\quad \frac{(-2m_1 m_3 - m_2(m_1+m_3)}{2m_1 m_2 m_3} \\
Z_4 = &\quad \frac{\sqrt{-2m_1 m_2^2 m_3 + m_2^2 m_3^2 + m_1^2(m_2^2+4m_3^2)}}{2m_1 m_2 m_3}
\end{aligned}
$$

Note that this analytic solution to the Eigen frequencies can be used to approximate the first modes of the massive tether independent of the number of discretized masses actually used. Therefore, the first mode of the system with only one tether node is the same as the system with many tether nodes, assuming the masses are unchanged.

The repeated 0 roots relate to the DC offset present in the formulation of Eq. (2.5). Because Eq. (2.5) is formulated from the positions of the bodies, the equations naturally assume that zero tether force corresponds to separation distances between the masses that add up to the full tether length (i.e. L_0). Therefore the bodies have a constant, DC offset in their positions. The complex pair(s) in Eq. (2.23) and Eq. (2.24) represent the purely oscillatory motion, as expected from a spring-mass system. Eq. (2.24) has two sets of complex pairs due to the fact that a three body (single tether node) system has two modes: one from the full tether length is the first mode and one from the addition of the tether mass, causing a higher frequency.

Unfortunately, it becomes very difficult to analytically solve for the Eigenvalues and frequencies of the tether as more nodes are added. The Abel-Ruffini theorem demonstrates that there are no general algebraic solutions to polynomials of degree five and higher.[7,59] This means that it is not likely that the full set of Eigenvalues for tether discretizations beyond three or four nodes is analytically achievable. Also, as the number of nodes, n, increases, so does the integration time. However, this is not a major concern because the majority of the energy and dynamics of the system come from the first few modes, or Eigenvalues. Therefore, the primary modes of interest can be analytically computed for any system. Further, these modes will be the same, independent of the number of discretized nodes placed on the tether.

2.2.3 Verification of Model

With a complicated software model such as this, it is necessary to verify that it is physically realistic. This is done two ways, first by verification with a FEM method and second by conservation of energy and momentum.

2.2.3.1 Tethered Coulomb Structure Model Verification

The discrete tether mass system is compared to a FEM of a repulsive, Coulomb-force system. This system, known as the Tethered Coulomb Structure (TCS),[76] models several spheres with equal potential on each and explores the dynamics of the structure in multiple environments. The FEM compared two rigid end bodies, connected by a continuous tether, in various rotational initial conditions. An example is shown in Figure 2.4(a) where an initial rotation induces motion of the end masses and deflection of the massive

tether.

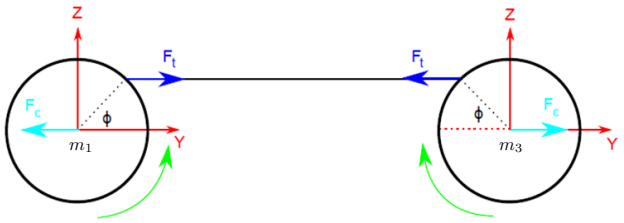

(a) Continuous tether[72]

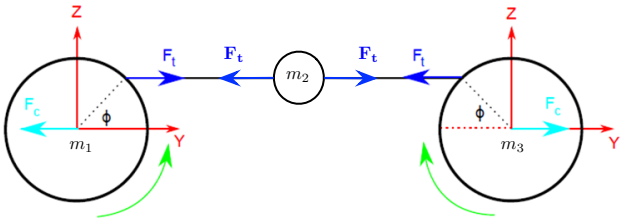

(b) Single discretized tether mass

Figure 2.4: TCS rotational test model. Voltages applied to rigid end bodies

The discrete tether model is compared against the FEM model using a single tether mass and equivalent end body rotational conditions (Figure 2.4(b)). The FEM model and the discrete tether model responses are very similar in both timing and displacements of the tether and bodies. For example, the FEM maximum rotation angle of the bodies is seen to be about 58.34 degrees occurring at 235 seconds, while the discrete tether model shows a rotation of 54.88 degrees occurring at 236 seconds. The energy and FEM verifications helped to demonstrate that the tether model was properly implemented and provided reasonable answers.

2.2.3.2 Conservation of Energy

The kinetic, potential, and rotational energy profiles are also computed by the software at each time step. This is done for each body and then summed to obtain the total system energy. The system's energy is

computed using the following four energies:

$$\begin{aligned} \text{gravitational} = & \quad \sum_{i=1}^{N} -\frac{\mu}{|\boldsymbol{R}_i|} m_i \\ \text{spring} = & \quad \tfrac{1}{2} K_S \sum_{i=1}^{n} |\boldsymbol{R}_{i+1} - \boldsymbol{R}_i|^2 \\ \text{translational kinetic} = & \quad \tfrac{1}{2} \sum_{i=1}^{N} m_i |\dot{\boldsymbol{R}}_{i+1} - \dot{\boldsymbol{R}}_i|^2 \\ \text{rotational kinetic} = & \quad \tfrac{1}{2} \sum_{i=1}^{N} \boldsymbol{\omega}_i^T [I]_i \boldsymbol{\omega}_i \end{aligned} \tag{2.25}$$

Thrust is always applied to this system, and this is known to cause a change to the energy. Thus, to check that energy is conserved, the system energy is considered just after the thrust is turned off.

In order to characterize the energy, a two body (no tether mass) model is used. The initial conditions for the end bodies are taken from the system values just after a thrust maneuver has occurred and the thrust force has reached zero. The simulation is then run using the Runge-Kutta 4-5 variable step integrator at the following time steps: 1/100$^{\text{th}}$ s, 1/64$^{\text{th}}$ s, 1/32$^{\text{nd}}$ s, 1/16$^{\text{th}}$ s, 1/8$^{\text{th}}$ s, 1/4$^{\text{th}}$ s, 1 s, 2 s, 4 s, 8 s, 16 s, and 32 s. The changes in energy correspond to changes over two orbits.

Figure 2.5 shows the results from the energy study. Figure 2.2.3.3 shows the most positive and negative change in energy for each integration time step. Figure 2.5(b) shows the maximum magnitude of the energy change. Figure 2.2.3.3 demonstrates that integrator time steps of over 1 s experience energy changes in the tens to hundreds of Joules. Further, some of the larger time steps experience unbounded growth in some states, causing unrealistic motion. Therefore, smaller time steps are required. Figure 2.5(b) shows a dramatic reduction in energy change with the 1/4$^{\text{th}}$ s, 1/8$^{\text{th}}$ s, and 1/16$^{\text{th}}$ s time steps achieving a change of 0.58 J at a step size of1/16$^{\text{th}}$ s. However, the smallest time steps experience a slight increase in energy change, all hitting about 2 J. This suggests that the 1/100$^{\text{th}}$ s, 1/64$^{\text{th}}$ s, 1/32$^{\text{nd}}$ s time steps have maximized the integrator performance and may begin to accumulate more floating point error than error due to integrator accuracy.

It turns out that the fixed step RK 5 integrator conserves energy better in some cases, however it does take longer to run. Often, energy is conserved to on the order of 1×10^{-2} J for deep space and orbital simulations. This integrator is used in tandem with the variable step RK 4-5 integrator, depending upon which conserves overall energy best.

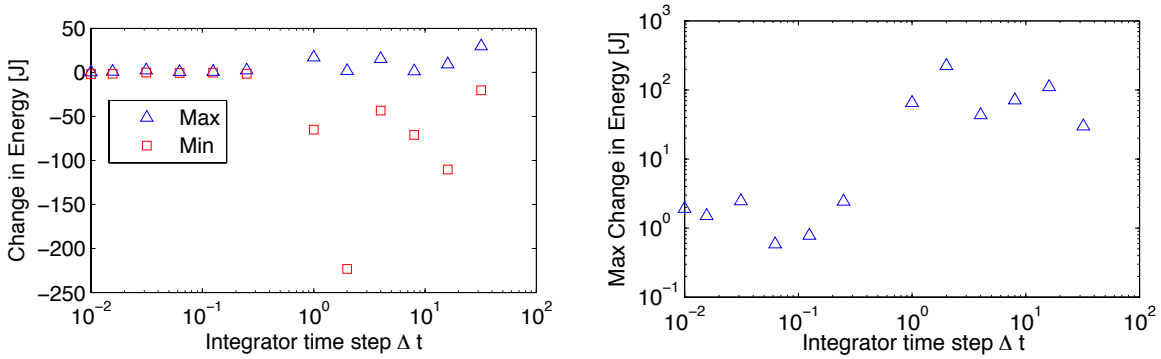

(a) Most positive and negative energy changes

(b) Largest magnitude energy change

Figure 2.5: Energy change in simulation due to integration step size, 2 orbits. Maximum energy of system $\approx 100 \times 10^{11}$ J.

2.2.3.3 Conservation of Momentum

Momentum conservation is also considered for the model used. The system's total momentum is defined as:

$$\boldsymbol{H} = \sum_{i=1}^{N} \boldsymbol{R}_i \times m_i \dot{\boldsymbol{R}} + [IB]([I]_i \boldsymbol{\omega}_i) \tag{2.26}$$

where $[IB]$ is the rotation matrix between the body frame and the inertial frame, assuming the position and velocity vectors are expressed in the inertial frame. In deep space, angular momentum for the system is conserved to within 1×10^{-3} N-s or better. Figure 2.6 demonstrates the change in momentum for initially rotating end-bodies.

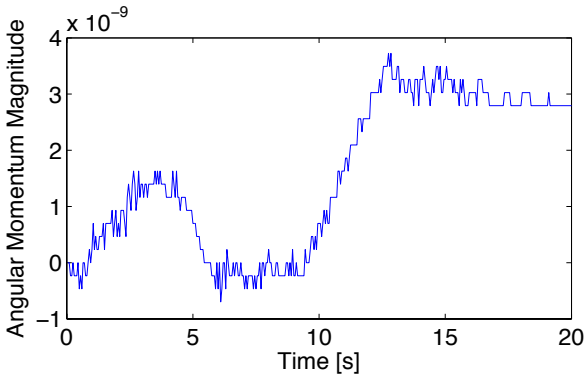

Figure 2.6: Angular momentum change for 6^o/sec end body rotation rate in deep space. Maximum momentum of system $\approx 2 \times 10^6$ N-s.

2.2.4 Number of Tether Discretizations

One obvious question about the model concerns how many tether nodes should be used. Discretizing the tether into many, small lumped-masses should more accurately predict the behavior of the tether. However, the tether mass is relatively small compared to the end bodies. Since the tether mass is small, it is not expected that lumped-masses should greatly influence the overall behavior significantly. While adding nodes allows for a higher modes, and in some ways more tether-like behavior, it also creates longer integration times and worse energy and momentum conservation performance. These things coupled can actually cause significant computational issues.

It turns out that using multiple tether masses does not actually cause major variation in motion. Figure 2.7 shows how the behavior of the system varies with only end bodies, one, and two tether masses. Figures 2.7(a) and 2.7(b) show that the overall response is very similar between the cases shown. Figures 2.7(c) and 2.7(d) show how the energy changes over the simulation. The end body only simulation conserves energy to 2×10^{-2} J but adding several nodes causes energy variation on the order of 5 J. (It was seen that the variable step RK 4-5 saw many hundreds of Joules of energy change on orbit when more than the end bodies were considered. This caused the shift to using a fixed step method with small time steps, which is often used for orbital simulations.)

This leads to the conclusion that over relatively short duration, the behavior is primarily described by the end body motion. Further, this research is most concerned with end body behavior (to avoid collisions) and not exact tether performance, therefore the tether model does not require extreme fidelity. Finally, it turns out that input shaping control only requires knowledge of the first mode of the system (see Chapter 3). For simplicity, the number of tether nodes used within this thesis is limited to two nodes or less.

2.2.5 Deep Space Simulations

There are two overarching simulation types: deep space and on-orbit. For deep space, the simulation software model simply has the gravity turned off. This allows for pure tether-to-rigid body motion to be studied. Oscillation rates, control performance and tether mass motion can all be observed as they naturally

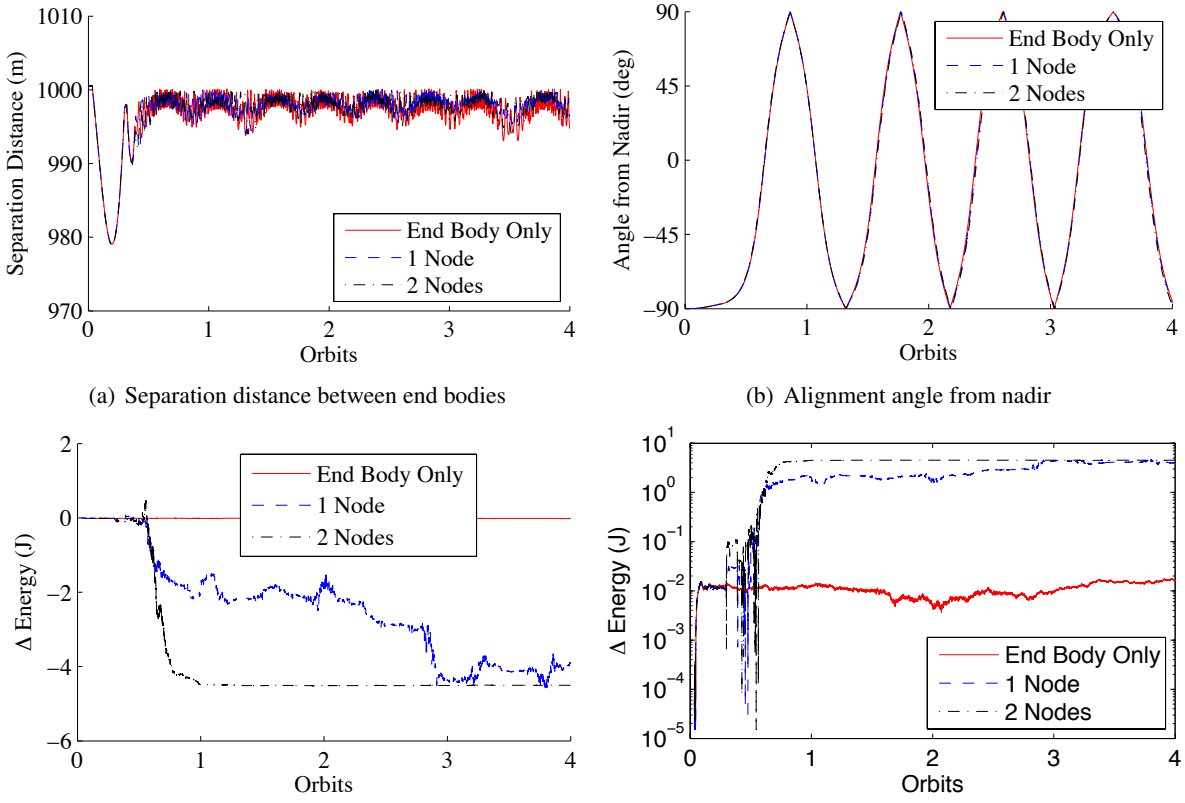

(a) Separation distance between end bodies

(b) Alignment angle from nadir

(c) Energy change post-thrust

(d) Energy change post-thrust, log scale

Figure 2.7: System performance variation due to multiple tether masses

occur. This gives significant insight into how to control the system and the potential for collision between the bodies. Because Eq. (2.5) is the equation of motion, linear system analysis can be easily performed (see Chapter 2.2.2), including Eigen mode analysis, allowing for significant knowledge gains about the behavior. Deep space simulations are also generally applicable to towing in large, heliocentric orbits where the gravitational field is weaker than near massive bodies. This is particularly applicable to asteroid towing missions where relative motion is more dominant than the orbital motion, in short term time scales.

2.2.6 Orbital Simulations

Orbital simulations demonstrate how well the controls and system perform in a realistic setting for satellite servicing and the ADR mission concepts. Several unexpected results have occurred, primarily that collisions are not as likely in orbit and that gravity gradient orientations can occur (maximizing the distance

between tug and tow mass). While deep space simulations are key to understanding the system, the orbital simulations comprise a larger portion of the research.

2.3 Baseline Concept Parameters

(a) Soyuz upper stage - the tug

(b) Second stage of SLV Cosmos-3M[34] - the debris

Figure 2.8: Upper stage rocket bodies used for this study

For this thesis the tug, debris, tether, and simulation parameters are given in Table 2.1. The mass and inertia values for the tug are similar to the Soyuz upper stage rocket (Figure 2.8(a)[1]) and the debris values are close to the Cosmos-3M second stage (Figure 2.8(b)). Kevlar is used as the tether material because it is commonly used in tether analysis[14] and the diameter of 3 mm is chosen to withstand the stresses experienced. A ∼2000 N thrust is chosen to be representative for the Soyuz upper stage thrusters while achieving the worst case, maximum tension in the tether at the time of engine cutoff.[34] Note that the 'step-input' thrust linearly ramps on and off, to and from the max thrust over a period of 1 second. The Δv capability is based upon the fuel reserves that may be available in the Soyuz after delivering a payload to orbit. Finally, the starting altitude of 800 km is based upon the known high density of Cosmos rocket bodies at that altitude and the fact that they are considered high priority targets for ADR.[47]

If Eq. 2.24 is analyzed given the values in Table 2.1, the natural frequencies of the system are obtained.

[1] http://www.arianespace.com
[2] http://www.matweb.com/index.aspx

Table 2.1: Vehicle, Tether and Simulation Parameters

Tug Mass	2500 kg
Tug Inertia	diag[10208, 10208, 2813] kg m^2
Tug Radius	1.5 m
Debris Mass	1500 kg
Debris Inertia	diag[1285, 6829, 6812] kg m^2
Debris Radius	1.2 m
Tether Length	1000 m equal space between masses
Tether Material	Kevlar
E	1470 GPa
Tether Yield Stress	3.54 GPa
Tether Diameter	3.2 mm
Tether Density	1470 kg/m^{32}
Thrust	2009 N
Δv	100 m/s
Starting Altitude	800 km (circular)

It is interesting to note that the fundamental frequency is the same between the two-body, three-body, or four-body cases. This turns out to be (for two bodies: $m_1 = 2500$ kg, $m_2 = 1500$ kg; for three bodies: $m_1 = 2500$ kg, $m_2 = 11.82$ kg, and $m_3 = 1500$ kg, for four bodies: $m_1 = 2500$ kg, $m_{2a} + m_{2b} = 5.91 + 5.91 = 11.82$ kg, and $m_3 = 1500$ kg) $\omega_{n1} = 0.19$ Hz. The three node case also has its second mode at $\omega_{n2} = 3.43$ Hz. The first mode is of greatest concern and is the frequency that all input-shaping methods consider in Chapter 3.

Chapter 3

Open-Loop Input Shaping for the Tethered-Tug System

No active debris removal system should create debris in orbit. Safety is highly important for any ADR system and the creation of even small debris from a larger body should be unacceptable. With respect to the tethered-tug system, safety is defined through collision avoidance between the end bodies. Collision between these two bodies, even at fairly low relative speeds is likely to cause some particulates. The ill effects of a post-burn collision are minimized because all objects will have a lower periapsis, and shorter orbital lifetime. But, this is still an undesirable situation. Therefore, the system must be designed to maintain separation between the end bodies.

Unfortunately, the fact that the two end bodies are tethered means that collision is a risk for the system. During the thrusting maneuver the tether is strained. When the thrust is no longer present the tether will restore itself to zero strain, pulling the tug and debris together. Because the tether only pulls on the masses when in tension, and does not provide a 'pushing' force when in compression, collisions between the large end-masses becomes possible. It therefore is important to study the complex system dynamics between high-force and slack tether motion and to control those dynamics.

3.1 Un-Shaped Input: the Step Input

The possibility of collision is illustrated in Figure 3.1 which demonstrates that a step input to achieve a $\Delta v = 100$ m/s in deep space results in collisions. The simulation used to produce Figure 3.1 uses two discrete tether masses. This behavior is discussed in greater detail in the following sections and in References 34 and 33. Therefore, it is important to reduce strain and relative motion between the bodies to

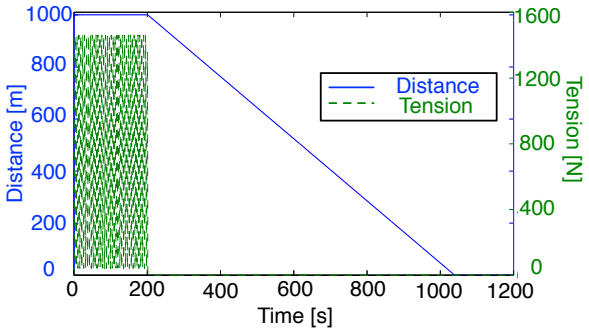

Figure 3.1: Relative motion and tether tension between tug and debris for a step input. Thrust duration of 200 s. Deep space

remove collision potential.

There are several ways to avoid collisions between the end bodies. One obvious method is to design the thruster control output to reduce the end body relative motion. This is done through open-loop input shaping of the thrust profile.

3.2 Description of Input Shaping

Input shaping is based upon the concept of modifying a desired input into a system such that it does not excite the system. An input shaped control or thrust profile can be designed so the primary natural frequency(ies) of the flexible body are not excited by the control input.[77,80] Figure 3.2 shows the open-loop control, S, that is based upon the modeled linear system dynamics $H(s)$.

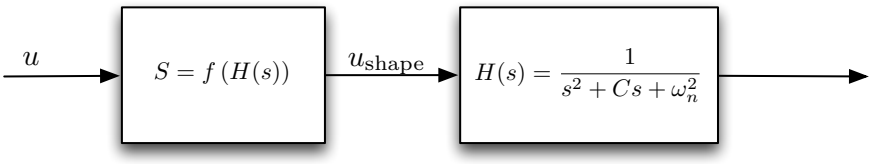

Figure 3.2: Open-loop control block diagram

Several input shaping methods have been developed and applied to cranes used to lift and maneuver loads at the end of a cable. There have been multiple studies of input shaping on flexible bodies, primarily led by Singhose or Singh.[42,77–82] Watanabe et. al and Singhose have considered input shaping for tethered

systems[80,89] but do not attempt velocity control or consider multiple input-shaping techniques.

For input shaping, the flexible system is simplified and modeled as a linear system, so that the natural frequencies of the system can be identified. As an open loop control, only a priori knowledge of the modes of the system is used to design the controller. With this information, many input shaping controls essentially place zeros over the poles of the flexible system, removing the oscillatory behavior. Of course, zero-pole cancellation is susceptible to the accuracy of the model. However, robustness of input shaping techniques have been studied[33,77] and are discussed below.

Figure 3.3 shows the thrusting profiles considered in this thesis including the baseline step input (Figure 3.3(a)), a continuously notched input (Figure 3.3(b)), a discretized notch profile (that looks similar to Figure 3.3(c)), a Posicast controller (Figure 3.3(c)), and an impulsive/bang-bang method (Figure 3.3(d)).

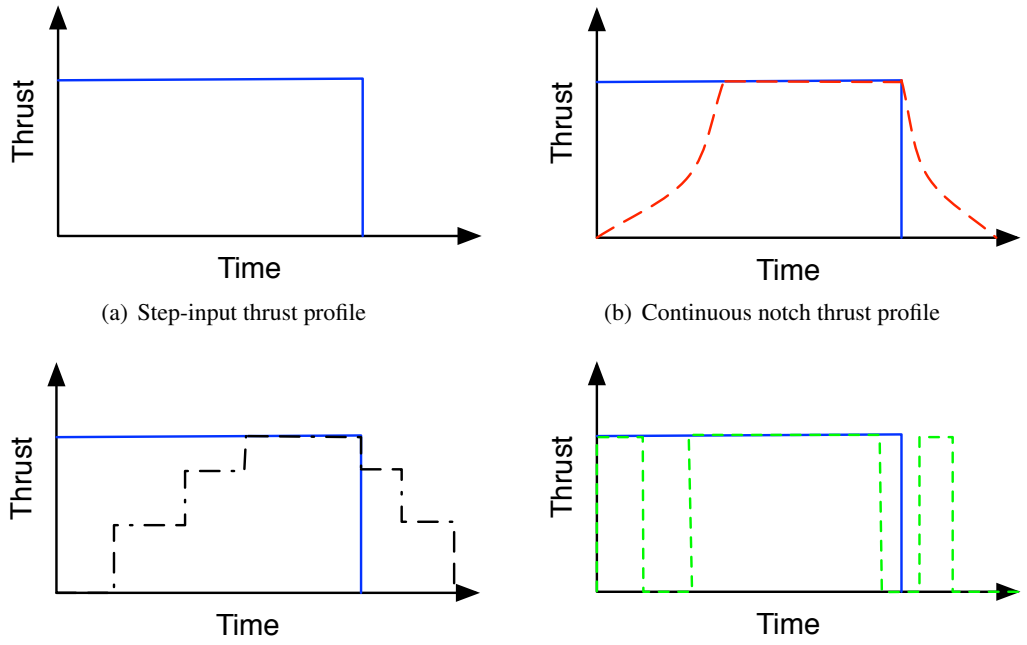

(a) Step-input thrust profile

(b) Continuous notch thrust profile

(c) Discretized notch and Posicast thrust profile

(d) Bang-off-bang thrust profile

Figure 3.3: Example thrust profiles considered

The step input in Figure 3.3(a) is produced by specifying the thrust, T, the mass of the system M, and the amount of Δv capability. The duration of the step profile, Δt, is then computed.

$$\Delta t = \frac{M}{T}\Delta v$$

Because the step profile excites all modes, shaped inputs are required to remove this excitation. The thrust applied can be continuously varied to minimize relative motion between the end bodies,[33] shown in Figure 3.3(b). However, this continuous, smooth thrust profile is difficult to achievable by current-day rocket engines. It is possible that solid motor fuel core designs could be made to continuously vary the thrust, but this requires very specific and smooth burn rates which is a challenge. This motivates exploring discretized, Posicast, and bang-bang input shaping thrust profiles that are more realistic. The discretized thruster profile, Figure 3.3(c), could be implemented with a cluster of thrusters. For example, having 3 thrusters that can be turned on individually would provide 3 discrete levels of thrust. The bang-bang thruster profile, Figure 3.3(d), with time delays would be suitable for a single on-off thruster implementation.

This chapter explores the use of all the thrust profiles in Figure 3.3 and their merits and shortcomings. First, the continuous notch profile is presented. Next, this chapter expands upon the impulsive input shaping studies of Watanabe et. al[89] and Singhose[80] by analyzing convolution of multiple delay transfer functions, a Posicast system, and how such an open-loop deorbiting thrust profile is applicable for space-based towing applications. Bang-bang input shaping is also explored in high-thrust environments with rigid body end masses. Further, the continuous notch profile presented by Reference 33 is discretized so that only a set of discrete thrust-level steps are implemented. The later is considered as a simple reference case to illustrate the benefits of the more rigorous discrete-step and bang-bang input shaping profiles. The effectiveness of the input shaping methods is analyzed in deep-space simulations to understand the difference in performance between each method. On-orbit studies are then explored to consider the low Earth orbit ADR application.

3.3 Notch Filter Input Shaping

3.3.1 Concept

Input shaping is a common way to remove an undesired frequency response in a linear system.[46,79] For this specific application, a notch filter is used to remove, or highly attenuate, the natural frequency of the tethered system, as shown in Figure 3.4. In signal processing[30] a signal can be removed by applying a notch filter at the signal frequency. This however causes lag in the system, as shown by the phase shift. For

the tethered-tug system this only translates to slightly longer thrusting times. As stated in Section 3.2, the notch filter effectively translates to placing a zero over the pole of the system. The design of the notch filter and its performance is given in the following discussion.

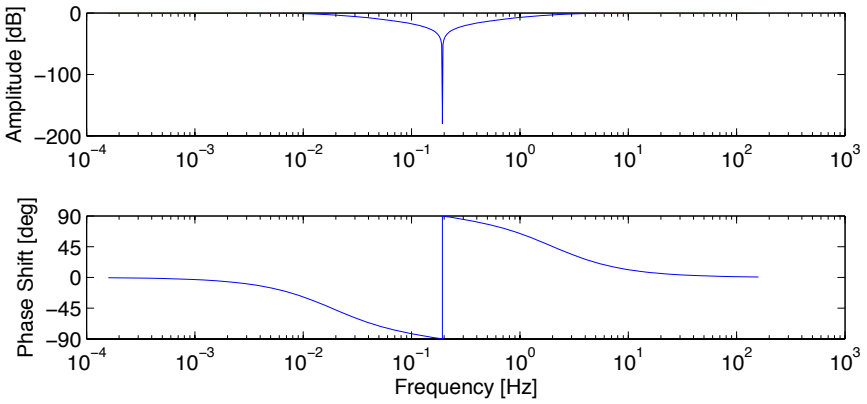

Figure 3.4: Bode plot demonstrating notch frequency response

3.3.2 Design

In the frequency domain, a first order notch filter is defined as:

$$g(s) = \frac{s^2 + \omega_c^2}{s^2 + \mathrm{BW}s + \omega_c^2} \tag{3.1}$$

where s is the frequency, ω_c is the cut-off or notch frequency, and BW is the bandwidth of the notch filter. Converting the frequency domain equation to the discrete time domain using the trapezoidal difference rule,[88] the notch filter can be written as shown in Eq. 3.2.

$$\begin{aligned} y_k = \frac{1}{4+2\mathrm{BW}h+h^2\omega_c^2}\big(&y_{k-1}(8-2h^2\omega_c^2) + y_{k-2}(-4+2\mathrm{BW}h-h^2\omega_c^2) + x_k(4+h^2\omega_c^2) + \\ &x_{k-1}(-8+2h^2\omega_c^2) + x_{k-2}(4+h^2\omega_c^2)\big) \end{aligned} \tag{3.2}$$

Here, y_k is the latest value of the shaped input from the filter and y_{k-i} is the $k-i^{\text{th}}$ value. x_k is the latest desired input into the system and x_{k-i} is the $k-i^{\text{th}}$ desired value. h is the time step of the discrete time system where most simulations use a time step of 0.25 s therefore $h = 0.25$.

It is also helpful to be able to notch multiple frequencies at once. This is simply created by multiplying multiple notch filters together, in the frequency domain, that have different cut-off frequencies. An example

of a double notch filter is given in Eq. (3.3)

$$g(s) = \frac{(s^2 + \omega_{c1}^2)(s^2 + \omega_{c2}^2)}{(s^2 + \mathrm{BW}_1 s + \omega_{c1}^2)(s^2 + \mathrm{BW}_2 s + \omega_{c2}^2)} \tag{3.3}$$

ω_{c1} is the first cut-off or notch frequency, ω_{c2} is the second cut-off or notch frequency, and BW1 and BW2 are the bandwidths for each notch. Eq. (3.3) is converted into the discrete time domain the same way as Eq. (3.2) and is given in Eq. (3.4).

$$\begin{aligned} y_k = & \frac{1}{(4+2\mathrm{BW}_1 h+h^2\omega_{c1}^2)(4+2\mathrm{BW}_2 h+h^2\omega_{c2}^2)} \\ & \Big(y_{k-1}(-4(-16+\mathrm{BW}_2 h(-4+h^2\omega_{c1}^2)+h^4\omega_{c1}^2\omega_{c2}^2+\mathrm{BW}_1 h(-4+h^2\omega_{c2}^2)))+ \\ & y_{k-2}(-96+8\mathrm{BW}_1\mathrm{BW}_2 h^2-6h^4\omega_{c1}^2\omega_{c2}^2+8h^2(\omega_{c1}^2+\omega_{c2}^2))+ \\ & y_{k-3}(4(16+\mathrm{BW}_2 h(-4+h^2\omega_{c1}^2)-h^4\omega_{c1}^2\omega_{c2}^2+\mathrm{BW}_1 h(-4+h^2\omega_{c2}^2)))+ \\ & y_{k-4}((-4+2\mathrm{BW}_1 h-h^2\omega_{c1}^2)(4-2\mathrm{BW}_2 h+h^2\omega_{c2}^2))+ \\ & x_k((4+h^2\omega_{c1}^2)(4+h^2\omega_{c2}^2))+ \\ & x_{k-1}(-64+4h^4\omega_{c1}^2\omega_{c2}^2)+ \\ & x_{k-2}(96+6h^4\omega_{c1}^2\omega_{c2}^2-8h^2(\omega_{c1}^2+\omega_{c2}^2))+ \\ & x_{k-3}(-64+4h^4\omega_{c1}^2\omega_{c2}^2)+ \\ & x_{k-4}((4+h^2\omega_{c1}^2)(4+h^2\omega_{c2}^2))\Big) \end{aligned} \tag{3.4}$$

In order to properly reduce motion between the tug and debris, the system's natural frequencies (Eigen values) must be known. Because the tether system is modeled as a linear spring when in tension, Eigen value analysis lends itself perfectly to this model. This is discussed further in Section 2.2.2.

3.3.3 Adding Robustness

It is likely that the mass of the debris is not well known. Based upon the Two-Line Element (TLE) catalog of tracked satellites, the general information about the object is probably available (rocket body or satellite, basic specifications of size and mass, etc.) however the exact information may not be available or missing. Mass is one of the most important and least well known parameters. Depending upon fuel remaining and passivation methods used by the operators, mass may vary noticeably.

This means that the Eigenvalues in Eq. (2.22), (2.23), or (2.24) are not well known and they can change from what is expected, lowering the effectiveness of the notch filter. The Eigen values are a function of multiple of the system properties, shown in Eq. (3.5).

$$\lambda = \omega_d = f(m_{\text{tug}}, m_2, m_3, ..., m_{\text{debris}}, E, A, L_0, C) \tag{3.5}$$

The linear sensitivity of the natural frequency to changes in debris mass is found by taking the partial derivative of the Eigenvalues with respect to the debris mass (m_{debris}). The partial is then evaluated at the expected value (given in Table 2.1, where the expected debris mass $m_{\text{debris }E} = 1500$ kg). Eq. (3.6), shows the linear change in the natural frequency given the true debris mass, $m_{\text{debris }T}$.

$$\Delta\omega_d(m_{\text{debris }T}) = \left.\frac{\partial\omega_d}{\partial m_{\text{debris}}}\right|_{K_S, m_{\text{tug}}, m_2, ..., m_{\text{debris }E}} (m_{\text{debris }T} - m_{\text{debris }E}) \tag{3.6}$$

Note that ω_d is the damped natural frequency which becomes the purely oscillatory natural frequency ω_n if C is zero in Eq. 3.5.

For a three body example with one tether mass and no damping, the sensitivity to the natural frequencies in Eq. (2.24) is given below. Here, $m_1 = m_{\text{tug}}$, $m_2 = m_{\text{tether}}$, and $m_3 = m_{\text{debris}}$. For the first pair of non-zero Eigenvalues the sensitivity expressions become:

$$\frac{\partial\omega_n}{\partial m_3} = \pm\frac{K_S\left(m_1m_2 - m_2m_3 + \sqrt{m_1^2m_2^2 - 2m_1m_2^2m_3 + (4m_1^2+m_2^2)m_3^2}\right)}{2m_3^2\sqrt{-4m_1m_2^2m_3 + 2m_2^2m_3^2 + 2m_1^2(m_2^2+4m_3^2)}} * \frac{\sqrt{m_1m_2m_3}}{\sqrt{-K_S\left(m_2m_3 + m_1(m_2+2m_3) + \sqrt{m_1^2m_2^2 - 2m_1m_2^2m_3 + (4m_1^2+m_2^2)m_3^2}\right)}} \tag{3.7}$$

and second pair of non-zero Eigenvalues are:

$$\frac{\partial\omega_n}{\partial m_3} = \pm\frac{K_S\left(-m_1m_2 + m_2m_3 + \sqrt{m_1^2m_2^2 - 2m_1m_2^2m_3 + (4m_1^2+m_2^2)m_3^2}\right)}{2m_3^2\sqrt{-4m_1m_2^2m_3 + 2m_2^2m_3^2 + 2m_1^2(m_2^2+4m_3^2)}} * \frac{\sqrt{m_1m_2m_3}}{\sqrt{K_S\left(-2m_1m_3 - m_2(m_1+m_3) + \sqrt{-2m_1m_2^2m_3 + m_2^2m_3^2 + m_1^2(m_2^2+4m_3^2)m_3^2}\right)}} \tag{3.8}$$

Evaluating Eq. (3.7) and Eq. (3.8) from $m_3 = 600$ kg to 2400 kg, Figure 3.5(a) shows that the mass of the debris can vary by 900 kg (60%) and it will only change the first mode by 0.034 Hz. The second mode in Figure 3.5(b) is even more insensitive and changes by only 0.002 Hz. Because the first mode contains the most energy and creates the most relative motion between masses, this mode will be focused on. (Notching

multiple modes was tested however no significant reduction in end body motion was experienced leading to the conclusion that the first mode should be the focus.)

Given the tether properties, masses of the tug and debris, the first mode should occur near 0.19 Hz. It turns out that a variance of 0.034 Hz in the first mode is enough to cause the notch filter to have noticeable, but relatively small, performance problems. One robust method to avoid sensitivity issues is to add a second notch in the region of the first mode.

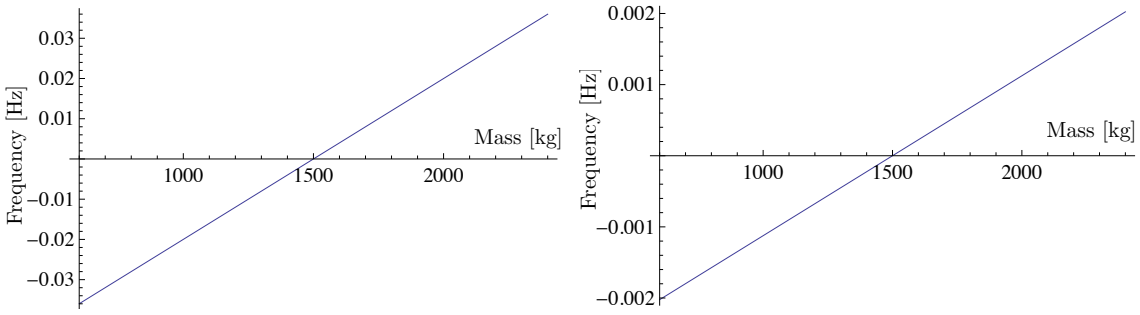

(a) First mode ($\omega_n = 0.19$ Hz) (b) Second mode ($\omega_n = 3.43$ Hz)

Figure 3.5: Sensitivity of the tether-mass system's first two fundamental modes to imperfect debris mass knowledge

To design a double notch around the first mode, Figure 3.5(a) is used to determine the potential range over which the first mode can vary. When two notches are placed near each other, they effectively attenuate a range of frequencies. This behavior can be seen in Figure 3.6 where frequencies 0.14 Hz – 0.22 Hz are very heavily notched. While there is reduced attenuation between these two frequencies it is still very large, peaking near -58 dB (half way between the notched range, at 0.18 Hz). This is sufficient to reduce the first mode's energy while being robust to knowledge errors in the debris mass. The results of notch input shaping are discussed further in Sections 3.3.4 and 3.3.5.

While the debris mass will be the least well known, the tether spring constant may have variability as well. Because the natural frequencies are very dependent upon this parameter (K_S), it is important to consider. Using a similar linear sensitivity analysis as in Eq. (3.6), the system's natural frequency response to variable material properties is:

$$\Delta\omega_n(K_{S\,T}) = \left.\frac{\partial\omega_n}{\partial K_S}\right|_{K_{S\,E},m_{\text{tug}},m_2,\ldots,m_{\text{debris }E}} (K_{S\,T} - K_{S\,E}) \tag{3.9}$$

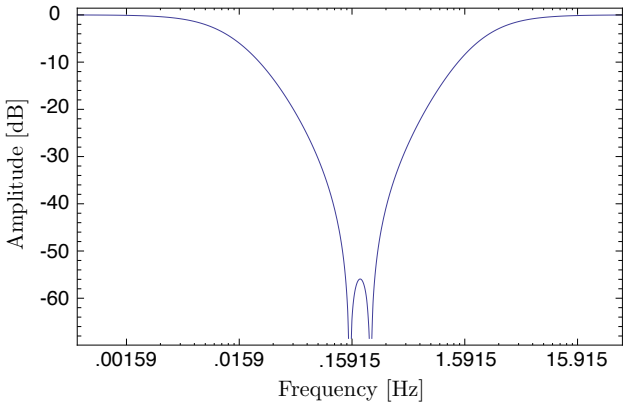

Figure 3.6: Double notch centered about first fundamental mode of system

Evaluating Eq. (3.9) across a 20% change from the expected spring constant ($K_{Se} \approx 4,100$ N/m, between each node), Figure 3.7 is obtained. Note that a 20% change in spring constant is approximately equal to a Young's Modulus change of 34 GPa or a 0.7 mm change in the radius of the tether, both fairly large numbers. However, these can be considered worst case and they achieve similar variability in the natural frequency as a 500 kg change in debris mass. These results are further discussed in Section 3.3.4.

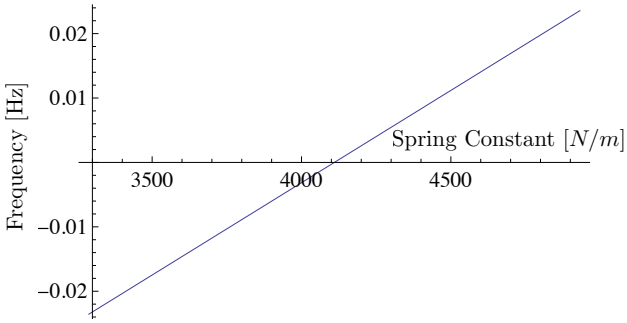

Figure 3.7: Sensitivity of the tether-mass system's first fundamental mode ($\omega_n = 0.17$ Hz) to variable spring constant

Figure 3.8 demonstrates the continuous notch thrust profiles compared to the step input. This step input is the input that is shaped by the notch. Notching does cause phase lag in the thrust profiles and the system responses. Therefore the thrust period of a step input is shorter than a single or double notch. It takes the step input (no shaping) about 201 seconds to achieve a $\Delta v = 100$ m/s while the single notch takes 238 seconds and the double notch 283 seconds to reach within about 1% of a 0 N thrust. This means that it takes

less than five minutes for any of these methods to perform their burn, a time duration which is short when considering an orbital period of around 90 minutes in LEO.

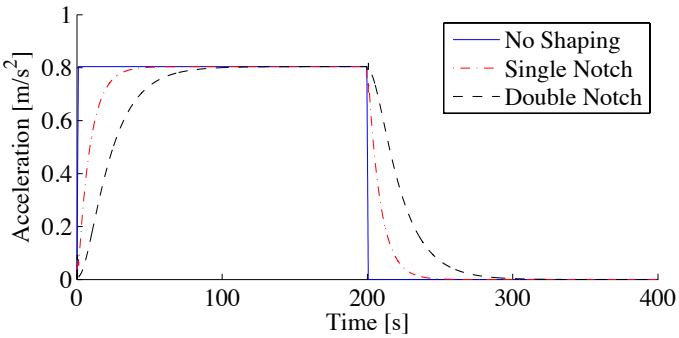

Figure 3.8: Thrust profiles with different input shaping techniques

3.3.4 Deep Space Performance

Deep space performance is given to show how the profiles work in a simplified environment that may also be applicable to some towing scenarios. Note that the simulations shown utilize the following:

- The trapezoidal difference method is used to go from the frequency domain to discrete time, for the notch filter input-shapers
- The attitude on the tug (m_1) is maintained while thrusting occurs
- The Δv applied is equal to 100 m/s. Based upon input-shaping method, this can vary the thrusting duration
- Two tether masses and two rigid end bodies are used for this study

To demonstrate why input shaping (notching) is required, consider Figure 3.1 where no shaping method is used during thrusting. Here the thruster cuts off at $\Delta v = 100$ m/s while there still is tension in the tether. The restoring spring force in the tether will pull all masses together and eventually cause a collision, as seen beyond 1000 s in Figure 3.1. It therefore becomes imperative to reduce the remaining tether tension to stop post thrust relative motion between the masses.

As an alternate control method, the thrust profile is filtered so that the fundamental frequencies of the tethered system are removed. Using a notch filter (Eq. (3.1)), the first fundamental mode, shown in Figure 3.9(a) at $\omega_n = 0.19$ Hz, is removed and the behavior becomes much more desirable. Figure 3.10 and Figure 3.9(b) show the improvement in the post thrust dynamics. In this case, the notching shown in Figure 3.9(b) presents an ideal situation where all system parameters are well known. The relative motion between the tug and the first discrete tether mass is significantly reduced, Figure 3.10, and there is less than a meter of relative drift between the two. This result is very similar for the relative motion between the other tether masses and the debris. Figure 3.9(b) demonstrates the dramatic difference in the response profile. The fundamental mode, seen as the first peak in Figure 3.9(a), is heavily attenuated in Figure 3.9(b).

Figure 3.11 compares the tether mass frequency responses. Note that this response is very similar between both tether masses modeled, therefore only one set of plots is shown. The tether masses are shown here to generally move and oscillate at higher frequencies than the larger rigid bodies. The notching has less of an effect on their behavior however there are subtle reductions in the profile below 1 Hz in Figure 3.11(b). Figure 3.12 compares the debris behavior between the step input and notched thrust profiles. In Figure 3.12(b) it is also obvious that the first mode at 0.19 Hz has been significantly attenuated, as desired.

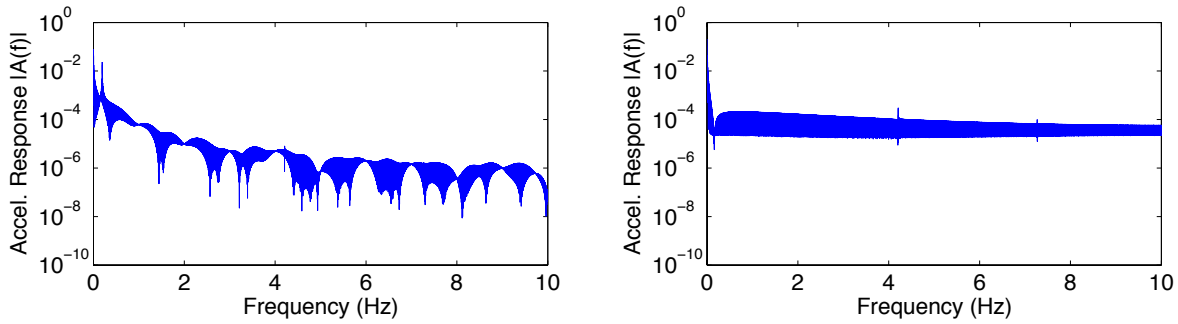

(a) Step-input thrust profile

(b) Notch at $\omega_c = 0.19$Hz

Figure 3.9: **Tug** vehicle frequency response to 2009 N thrust, with 2 discrete tether masses. Deep space

If knowledge of the debris mass is in error, then the performance of the single notch is reduced. Using a double notch, as described in Section 3.3.3, while including errors in debris mass knowledge, significant reductions in relative motion are still produced (Figure 3.13). Figure 3.13(a) shows the single notch placed at the expected, but incorrect, natural frequency. This causes a small but noticeable collapse of the system.

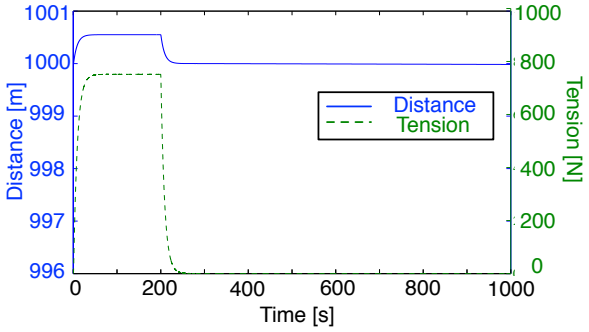

Figure 3.10: Relative motion and tether tension response between tug and debris for a single notch with the cut off frequency at the first mode. 2009 N thrust, with 2 discrete tether masses. Deep space

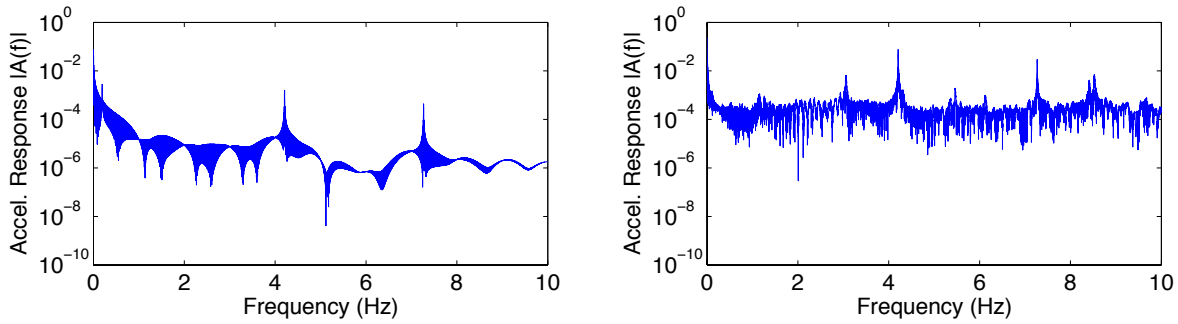

(a) Step-input thrust profile

(b) Notch at $\omega_c = 0.19$Hz

Figure 3.11: **Tether mass** frequency response to 2009 N thrust, with 2 discrete tether masses. Deep space

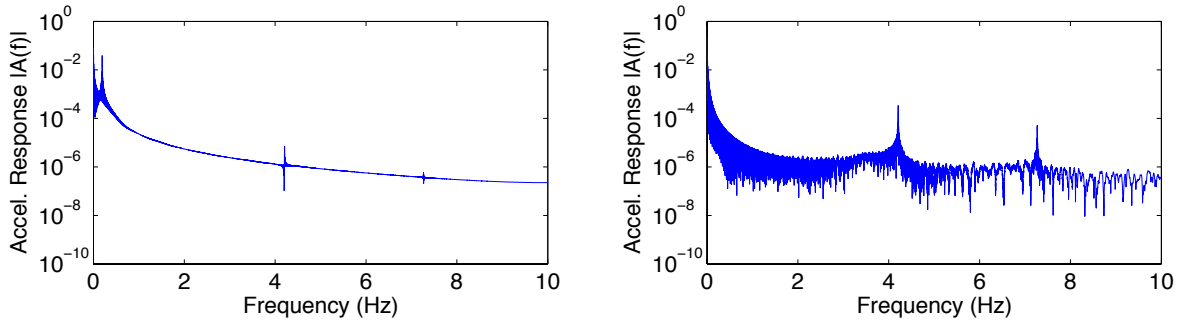

(a) Step-input thrust profile

(b) Notch at $\omega_c = 0.19$Hz

Figure 3.12: **Debris** object frequency response to 2009 N thrust, with 2 discrete tether masses. Deep space

Conversely, Figure 3.13(b) shows that the double notch effectively reduces the motion between the masses, even though the exact natural frequency is not well known. It turns out that the relative motion of the masses are reduced nearly as well as the perfect single notch of Figure 3.10. The performance difference between

the single notch and the double notch spanning a wide range of frequencies can be seen in Figure 3.14. The double notch experiences more attenuation of the first mode, compared to the improperly placed single notch. The double notch frequency response does see less attenuation near 0.2 Hz, in the same location as the 'hump' in Figure 3.6, which is expected.

If knowledge of the debris mass is in error, then the performance of the single notch is reduced. Using a double notch, as described in Section 3.3.3, while including errors in debris mass knowledge, significant reductions in relative motion are still produced (Figure 3.13). Figure 3.13(a) shows that the single notch placed at the expected, but incorrect, natural frequency experiences small but noticeable collapse of the system. Conversely, Figure 3.13(b) shows that the double notch effectively reduces the motion between the masses, even though the exact natural frequency is not well known. It turns out that the relative motion of the masses are reduced nearly as well as the perfect single notch of Figure 3.10. The performance difference between the single notch and the double notch spanning a wide range of frequencies can be seen in Figure 3.14. The double notch experiences more attenuation of the first mode, compared to the improperly placed single notch. The double notch frequency response does see less attenuation near 0.2 Hz, in the same location as the 'hump' in Figure 3.6, which is expected.

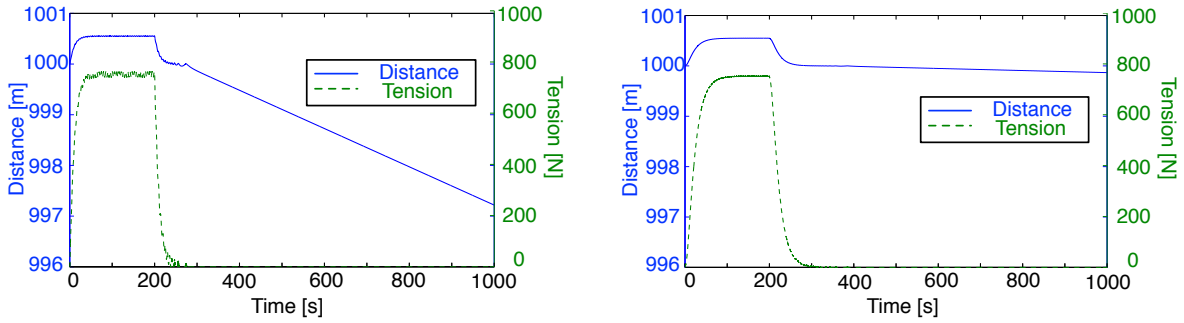

(a) Single notch, $\omega_c = 0.17$Hz

(b) Double notch spanning $0.14 \leq \omega_c \leq 0.22$Hz

Figure 3.13: Relative motion and tether tension response between tug and debris for an expected debris mass of 2000 kg ($\omega_n = 0.17$ Hz), actual mass is 1500 kg ($\omega_n = 0.19$ Hz). 2009 N thrust, with 2 discrete tether masses. Deep space

When the input shaping capabilities are compared between the single and double notch for spring constant variability (Figure 3.15), it can again be seen that the double notch successfully reduces the relative

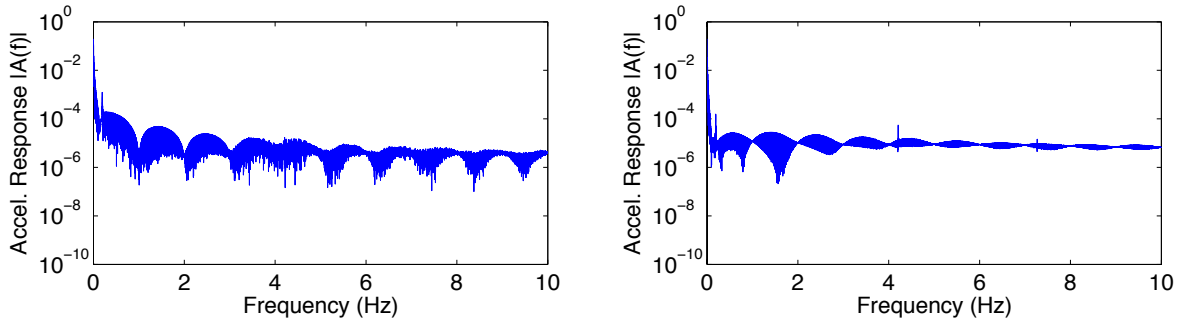

(a) Single notch, $\omega_c = 0.17$Hz (b) Double notch spanning $0.14 \leq \omega_c \leq 0.22$Hz

Figure 3.14: **Tug** vehicle frequency response with 2 discrete tether masses. Expected $\omega_n = 0.17$ Hz, actual $\omega_n = 0.19$ Hz. Deep space

motion between the two end bodies (Figure 3.15(b)) when compared to the single notch (Figure 3.15(a)).

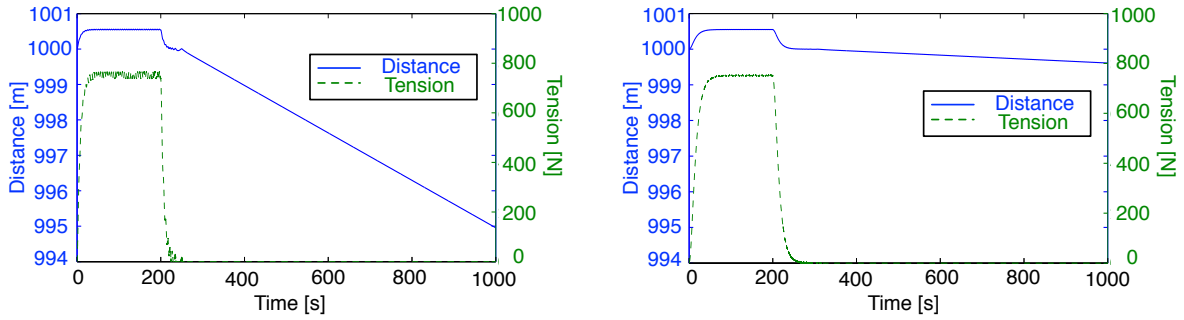

(a) Single notch, $\omega_c = 0.17$Hz (b) Double notch spanning $0.15 \leq \omega_c \leq 0.25$Hz

Figure 3.15: Tug vehicle frequency response to Spring Constant K_S variability with 2 discrete tether masses. Expected $\omega_n = 0.17$ Hz, actual $\omega_n = 0.21$ Hz. Deep space

This demonstrates that the double notch spanning the possible range of the first mode can effectively reduce collision potential between the masses with large uncertainties in the debris mass and tether material properties. This also demonstrates that the first mode is the most important because nearly all relative motion is stopped by notching only the first mode, while leaving the other modes unshaped. Tether models can become very complex, as they use partial differential equations and finite element solvers. It is significant to determine that the first mode is the only mode that needs to be notched because it is the most simple mode to model, estimate, and analyze, simplifying the control analysis.

3.3.5 On-orbit Performance

Deep space simulations motivate the use of a given thrust profile for on-orbit analyses. However, the orbital dynamics create interesting behavior that is not predicted by deep space analysis, including the tendency toward the formation tumbling end-over-end. Gravity gradient, or nadir oscillations can occur, too.[33]

To show the effectiveness of this method when on-orbit, a four mass (two tether mass) system is used with a double notch spanning across the first mode as shown in Figure 3.6. While the system's actual natural frequency is 0.19 Hz, the double notch allows for uncertainties in debris mass knowledge. The debris and tug craft are started in an 800 km circular orbit and a burn is produced in the anti-velocity direction to lower both object's orbits. A $\Delta v = 100$ m/s lowers the periapsis to about 425 km.

3.3.5.1 On-orbit Results

While the step input thrust profile (Figure 3.16(a)) transitions between periods of tension and slack, with highly dynamic behavior, the double notch (Figure 3.16(b)) experiences a slow and steady drift. The periodic behavior in the drift is from the small eccentricity in the orbit, after the maneuver. This drift is somewhat expected from the deep space results because the relative velocity between the end bodies is quite small and the formation only slowly collapses. This is fairly desirable behavior because the bodies are simply drifting, zeroing tension in the tether and reducing jerk and other strains on the system. If the applied Δv is large enough, the system could de-orbit while the bodies are still drifting, thus avoiding collisions.

The notch also is very beneficial when the end body spin rates are considered. Figure 3.17 shows the norm of the angular velocity of the rigid end bodies. It is clear that the step input causes large rotation rates in the end bodies and the tensioning events also cause large spin up/down behavior. Conversely, the notch's performance in Figure 3.17(b) demonstrates very small rotation rates, only several tenths of a degree per second.

Figure 3.18 helps to demonstrate why the system using the notch thrust profile does not see much relative motion. The end bodies start thrusting aligned with the in-track orbital direction (0^o) and the formation

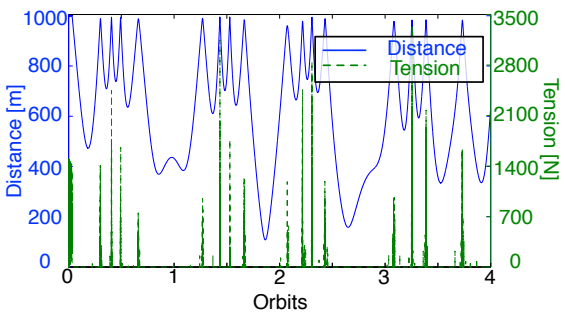

(a) Step-input thrust profile

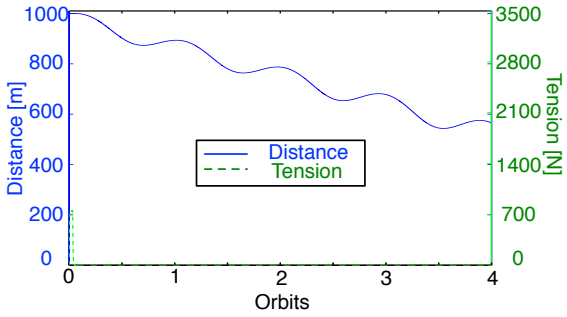

(b) Double notch spanning $.14 \leq \omega_c \leq .22$Hz

Figure 3.16: Relative motion and tether tension response between tug and debris for four orbits. Tether $\omega_n = .19$ Hz. 2009 N thrust, with 2 discrete tether masses. On-orbit

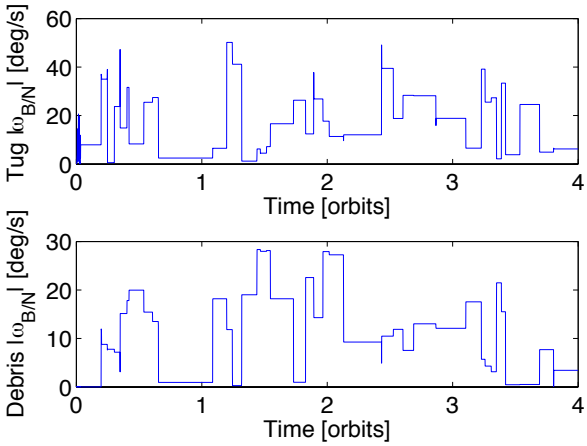

(a) Step-input thrust profile

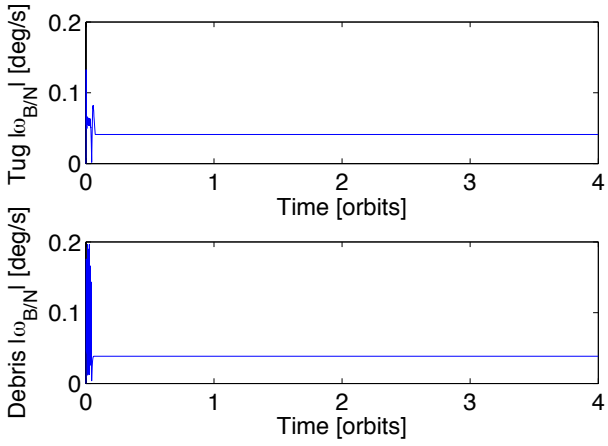

(b) Double notch spanning $.14 \leq \omega_c \leq .22$Hz

Figure 3.17: Notch end body rotation rates over 4 orbits

essentially stays in that orientation. The bodies are just slightly offset in position and slowly drift towards each other. The unshaped/step input ends flipping into an oscillation about the nadir direction, however this oscillation does not appear very constant.

Figure 3.19 – Figure 3.21 show the relative tether frequency responses due to the step-input and notched thrust profiles. In each case, the notched tether response is at least an order of magnitude smaller than the step-input, demonstrating again that there is less motion of the masses and less stress placed on the tether, all desirable traits of the notch. The first mode is easily identified for the step input in Figure 3.19(a) and Figure 3.21(a). The same mode in the notch profiles is attenuated by about two orders of magnitude

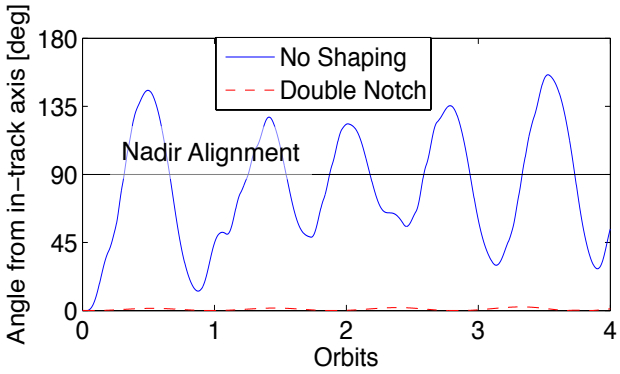

Figure 3.18: Angle from along-track vector. 90^o is the radial vector. On-orbit

and the higher modes are also visible (Figure 3.19(b) and Figure 3.21(b)). Another interesting trend is shown from the frequency response of the tether mass in Figure 3.20. Both of these response amplitudes are relatively high, showing that for their small mass, they experience significant motion. The step input causes such a high noise level, none of the frequencies are obvious in Figure 3.20(a). The frequency plots give another indicator that the notch input-shaper positively affects the motion of the tethered-tug system by reducing the overall motion between the bodies.

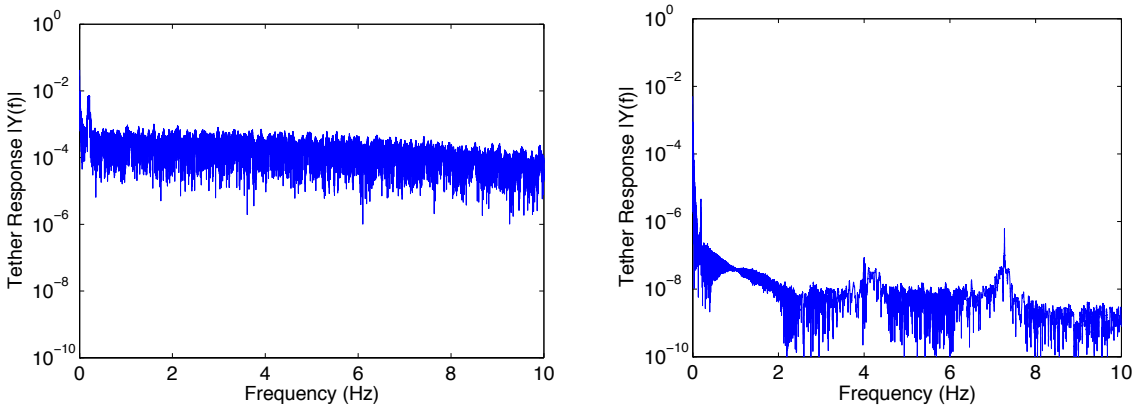

(a) Step-input thrust profile

(b) Double notch spanning $0.14 \leq \omega_c \leq 0.22$Hz

Figure 3.19: On-orbit tug/m_T vehicle frequency response with 2 discrete tether masses. Tether $\omega_n = 0.19$ Hz. On-orbit

Because the end bodies experience a slow drift towards each other when using the notch profile, it is interesting to consider what happens to the formation after a significantly longer duration. Figure 3.22 shows the end body motion, the formation's angle from nadir, the tension, and the rotation rates of the end

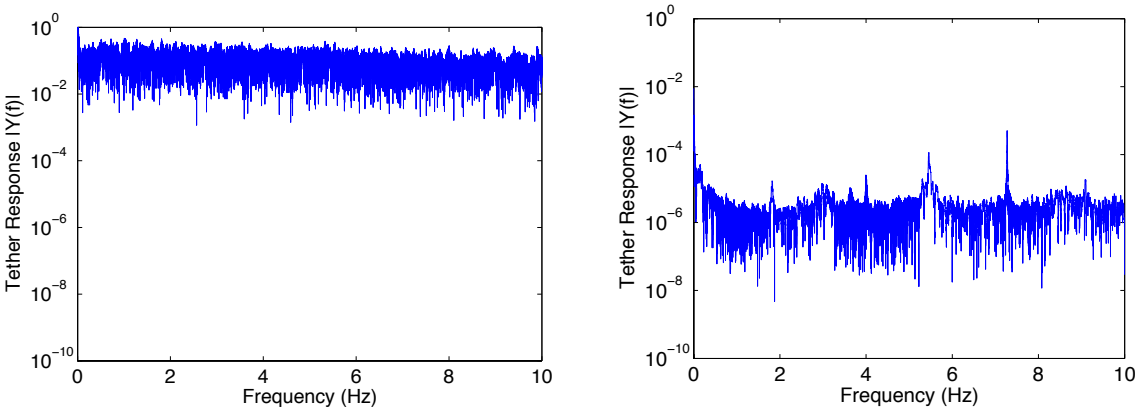

(a) Step-input thrust profile

(b) Double notch spanning $0.14 \leq \omega_c \leq 0.22$Hz

Figure 3.20: On-orbit tether mass frequency response with 2 discrete tether masses. Tether $\omega_n = 0.19$ Hz. On-orbit

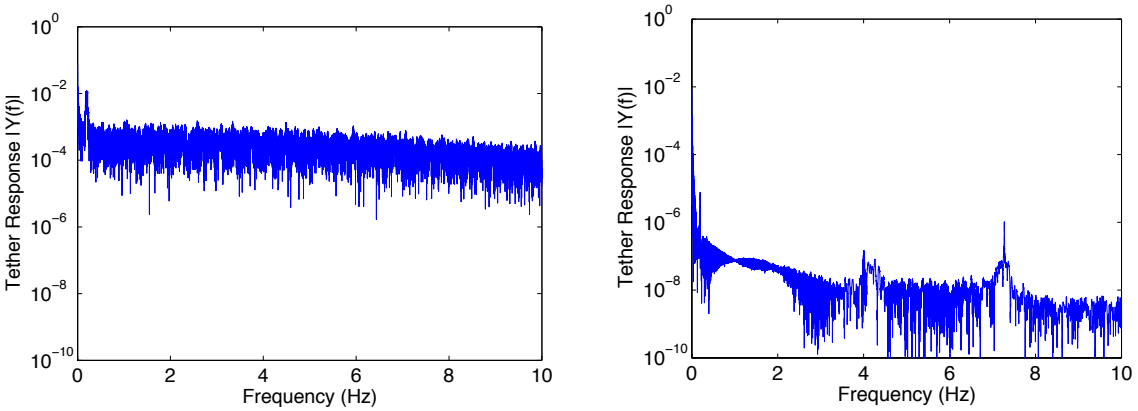

(a) Step-input thrust profile

(b) Double notch spanning $0.14 \leq \omega_c \leq 0.22$Hz

Figure 3.21: On-orbit debris/m_D object frequency response with 2 discrete tether masses. Tether $\omega_n = 0.19$ Hz. On-orbit

bodies. Near orbit 9, Figure 3.22(a) shows the end bodies becoming very close, although they do not contact. The bodies pass by each other and the formation eventually tensions, and then experiences two separate behaviors. The first, occurring between orbits 16 - 20 is a tumble where the formation is spinning end over end. Near orbit 21 the formation experiences a tensioning event and the system changes into a gravity gradient/nadir vector oscillation. (Tumbling or nadir oscillations are defined as the formation rotating about the center of mass either a full 360^o or along the radial/nadir vector of the orbit.) The tensioning event causes fairly high spin rates, as seen by Figure 3.22(b) however future tensionings reduce some of this spinning

motion.

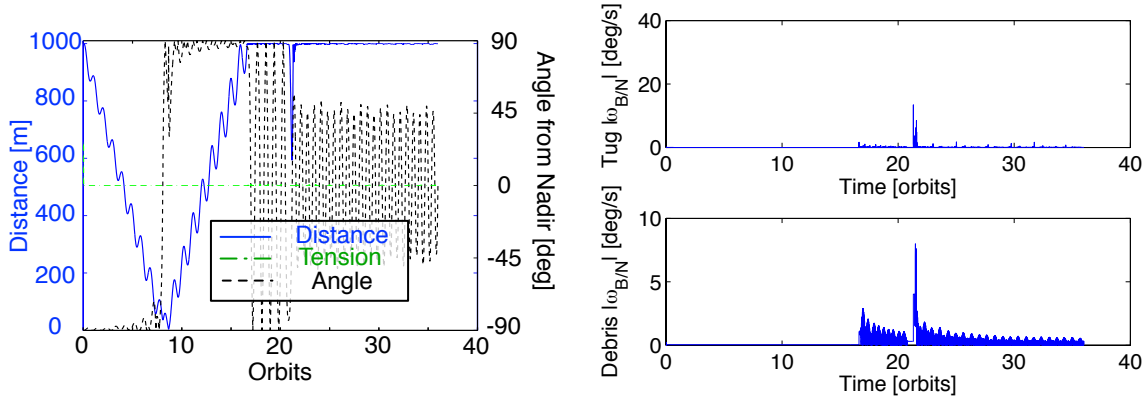

(a) Double notch spanning $.14 \leq \omega_c \leq .22$Hz

(b) Notch end body rotation rates over 4 orbits

Figure 3.22: Behavior of the double notched system over 36 orbits. Tether $\omega_n = .19$ Hz. 2009 N thrust, with 2 discrete tether masses. On-orbit

Unfortunately, this motion is not entirely believable for this system as significant system energy is lost during the integration, starting specifically when the tether re-tensions and tumbling starts. There are still several key take-aways from Figure 3.22. The first is that if the system loses energy, it can settle into a tumbling or gravity gradient oscillation, two motions that guarantee collision avoidance between the end bodies. This type of energy loss could be provided through damping in the system or possibly through atmospheric drag. Therefore, it is hypothesized that the longer the tethered-tug system stays on-orbit, the more likely it would fall into one of these motions. The next take away is that the notch provides good performance over short duration but the close approach is undesirable.

This motivates a slight alteration to the notch profile: once the perigee lowering maneuver has been performed with the notch filter, a short thrust burst in the radial direction to purposely given to initiate formation rotation. Figure 3.23 shows how a half second, 2000 N thrust in the radial direction changes the notch profile's performance. The end bodies maintain their initial separation distance of $L_0 = 1000$ m (Figure 3.23(a)) while getting into a gravity gradient oscillation (Figure 3.23(c)). (This simulation does conserve energy and therefore appears correct.) When re-tensioning does occur, the end bodies can experience large spin rates however the body ends up oscillating due to the tether tensioning. Tumbling of the end bodies occurs however wrapping of the tether with the bodies is not considered and left for future work. In the end,

this appears to be a better implementation of the notch profile to maintain separation distance of the end bodies.

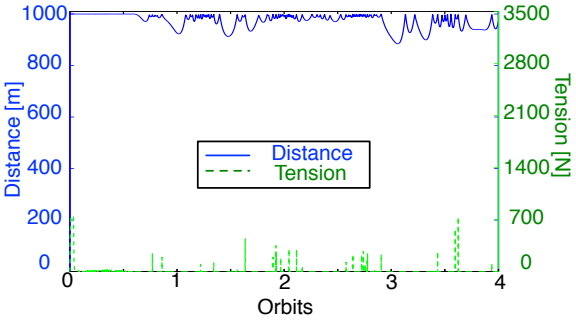

(a) Double notch spanning $.14 \leq \omega_c \leq .22$Hz

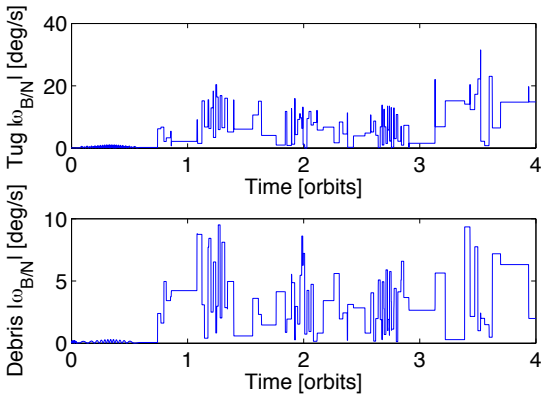

(b) Notch end body rotation rates over 4 orbits

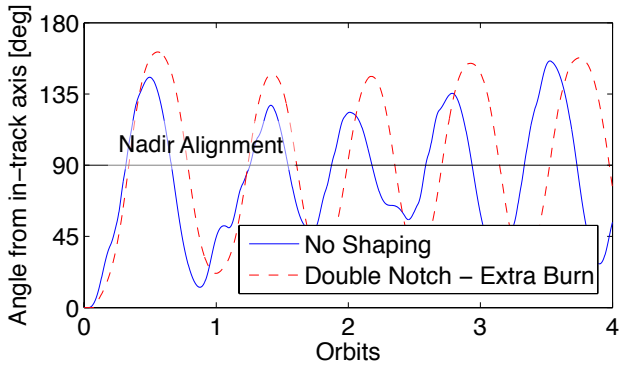

(c) Angle from along-track vector. 90^o is the radial vector

Figure 3.23: Behavior of the double notched system given a 0.5 s radial thrust after notch filtering. Tether $\omega_n = .19$ Hz. 2009 N thrust, with 2 discrete tether masses. On-orbit

3.3.5.2 Reducing Orbital Lifetime

To demonstrate the effectiveness of lowering the system's perigee due to the thrusting maneuver, an orbital lifetime analysis is completed. Assuming the tethered-tug system starts in an 800 km circular orbit, Figure 3.24 shows the impulsive Δv required to achieve a periapsis of a desired altitude. Figure 3.24 also demonstrates approximated capabilities of several launch vehicles' upper stages, assuming a 3% fuel margin for the stage. While the Δv capabilities of the vehicles are likely optimistic, this shows that most large vehicles today can at least reduce orbital lifetime, if not completely de-orbit, the tethered-tug system.

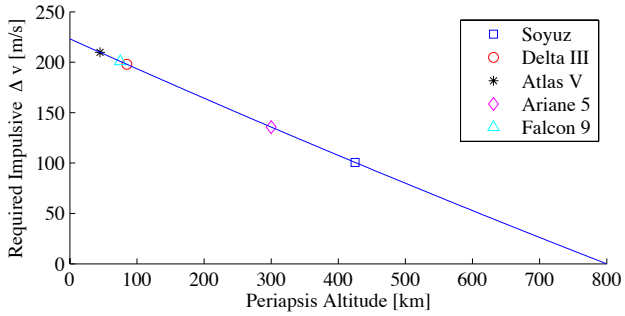

Figure 3.24: Required impulsive Δv to achieve periapsis altitude, given a starting 800 km circular orbit

Table 3.1 presents the lifetime results. On-orbit lifetime is modeled using drag coefficients for cylinders[66] that range between 2.4 and 2.9 assuming the long axis of the cylinders are directly into the ram-vector. The atmospheric temperatures are assumed not to vary significantly. The computation of drag coefficients of general shapes is complex and is still an active area of research. For the purpose of this study, simplified drag coefficients suffice as only approximate decay lifetimes are being determined. The tug and debris are assumed to be cylindrical bodies and the drag force is computed for each object and then summed about the center of mass. The tether is not included in this analysis due to the difficulty of determining the drag coefficient of such a large and thin structure. This means that the lifetimes obtained should actually be less than those given in Table 3.1. The ballistic coefficients under consideration fall between 0.0459 and 0.0555.

If no ADR or mitigation system is used, a circular orbit of about 700 km takes two to three decades to deorbit, a 800 km takes fifty to seventy years to deorbit while a 1000 km orbit takes more than a century.[84] By reducing the periapses to the 300-400km range, the tethered-tug system significantly reduces these time scales to less than 5 years, a major improvement. The elliptical 800 km by 425 km post-burn orbit used in this dissertation (Table 3.1, in bold) deorbits in about 3 years, much shorter than the natural decay rate or the 25 year requirement. If more residual fuel is present, a direct reentry maneuver is also feasible. However, as this table illustrates, using the small Δv to lower the periapsis of the tethered system has a significant impact on the debris' decay time.

Table 3.1: Lifetime of Tethered-Tug system using Jacchia 1977 atmosphere model[44]

Perigee	Apogee	Drag Coefficient	Circ. Orbit at Apogee (years)	Post-Maneuver (years)
350	700	2.4	27.72	0.74
		2.9	25.22	0.57
425	700	2.4	27.72	1.93
		2.9	25.22	1.56
350	800	2.4	73.39	0.99
		2.9	53.84	0.82
425	**800**	**2.4**	**73.39**	**2.71**
		2.9	**53.84**	**2.22**
350	1000	2.4	>100	1.48
		2.9	>100	1.19
425	1000	2.4	>100	4.39
		2.9	>100	3.66

3.3.6 Discretized Double Notch

The discussion so far has assumed that the thruster can provide any desired thrust level required by the notch filter. This is unrealistic for current-day thruster capabilities. Therefore, it is proposed to use the continuous notch thrust profile as a guideline, and then discretize that profile to several distinct thrust levels. The discretized input shaping control assumes the thruster is only capable of a set number of thrust levels. For example, with a cluster of 4 equal thrusters, the open-loop towing control is only capable of stepping the net thrust in 25% increments of the maximum thrust available. This is implemented by having each thruster individually turn on or off at the desired times. The basic algorithm is given in Eq. 3.10.

$$\begin{aligned} \text{step size} &= T_{\text{step}} \\ \text{desired thrust} &= T_{\text{desired}} \\ \tau_{\text{ratio}} &= \text{Mid-Point Rounding}\left(\frac{T_{\text{desired}}}{T_{\text{step}}}\right) \\ T_{\text{applied}} &= \tau_{ratio} * T_{\text{step}} \end{aligned} \tag{3.10}$$

The algorithm uses a simple rounding method. The rounding scheme in Eq. 3.10 uses a mid-point method so that if the desired thrust is greater than 50% of T_{step}, then the applied thrust will jump to the next step size, otherwise the applied thrust remains at the previous level. This causes the desired thrust to be *above* each step size to achieve a new T_{applied} level. The difference between the continuous and discrete applied thrust is demonstrated by Figure 3.25.

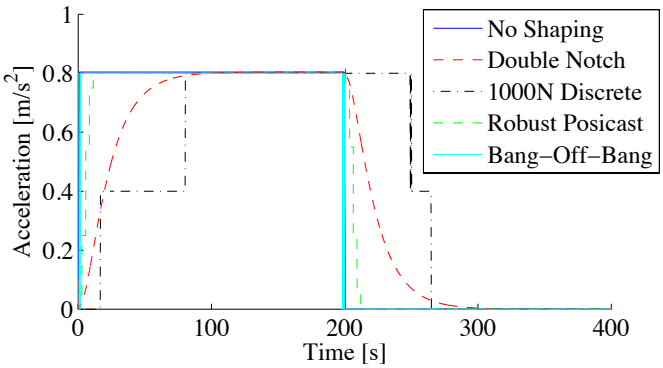

Figure 3.25: Applied thrust profiles with different input shaping techniques

3.3.6.1 Deep Space Discretized Notch Performance

Figure 3.26 shows two discretized notch, system responses. Figure 3.25 gives the profiles used. The continuous notch profile used to generate Figure 3.13(b) has been discretized into 100 N and 1000 N steps, producing Figure 3.26. The 100 N step size was chosen to study a relatively small discretization that could follow the desired continuous profile somewhat effectively. The 1000 N step size was chosen because it is much more likely that a realistic thruster is capable of a small range of different thrusts. A ∼2000 N thrust could be attained by coupling two, 1000 N thrusters and turning them on at desirable times.

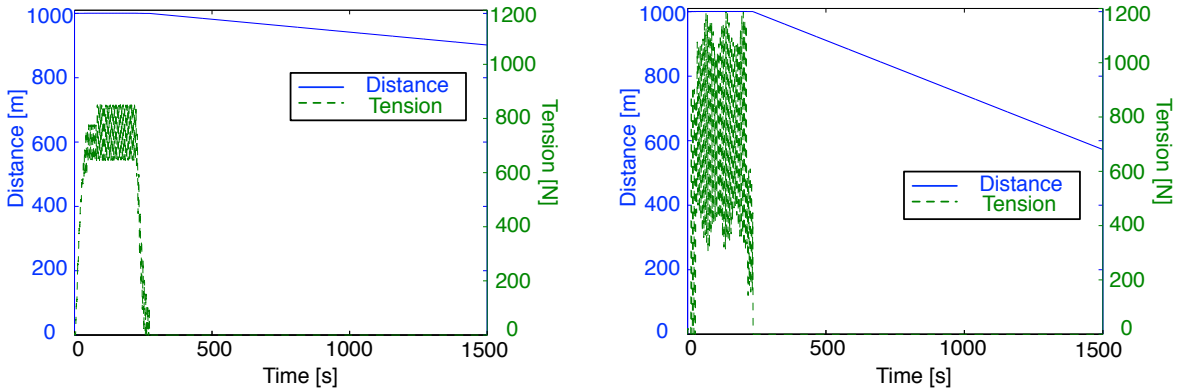

(a) 100 N step *discrete* double notch spanning $.14 \leq \omega_c \leq .22$Hz

(b) 1000 N step *discrete* double notch spanning $.14 \leq \omega_c \leq .22$Hz, collision at about 1000 s

Figure 3.26: Relative motion and tether tension response between tug and debris using a *discretized notch* profile. Expected debris mass of 2000 kg ($\omega_n = .17$ Hz), actual mass is 1500 kg ($\omega_n = .19$ Hz). 2009 N thrust, with 2 discrete tether masses. Deep space

Altering the continuous thrust profiles to discrete steps is moderately effective in reducing post-burn relative velocity even when introducing these discrete thrusting steps. The 100 N discretization sees greater than 900 m of separation between the two end bodies, showing that there was only a small amount of tension remaining in the tether at the end of the thrusting duration. However, the much cruder 1000 N discretization of the continuous thrust profile experiences much more relative motion, and the system collapses to 570 m after 1500 s. This shows the 1000 N discretization appears to be too crude of a discretization, even though it is more practical for current-day engine capabilities.

Figure 3.27 shows the frequency domain response of the tug mass, given the discretized thrust profiles. With the continuous notch profile, Figure 3.9(a) shows a step input exciting the modes of the tethered-tug system. The primary mode occurs at 0.19 Hz and has a fairly large magnitude. The double notch in Figure 3.14(b) reduces this first mode by about two orders of magnitude in power, thus creating the tiny relative motion in Figure 3.13(b). Conversely, the magnitude of the first mode in the 100 N discretized frequency response (Figure 3.27(a)) is only slightly attenuated from the step input. However, this is enough to produce small relative motion, as shown by Figure 3.26(a). The 1000 N discretization response (Figure 3.27(b)) has very little difference from the step input, and therefore experiences a post-burn collision quite quickly.

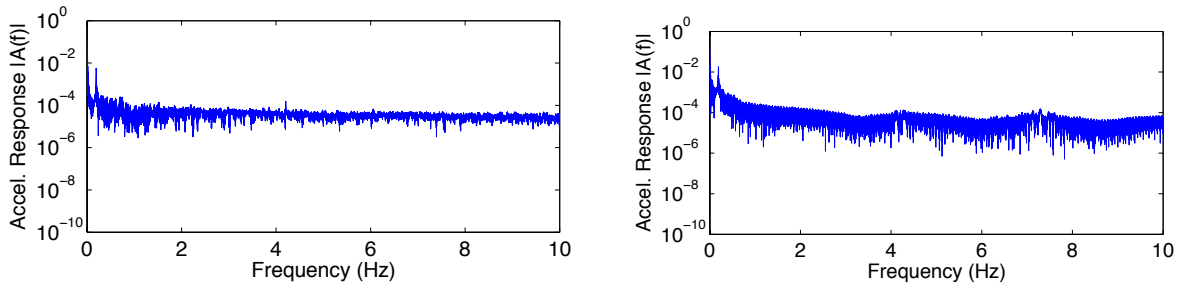

(a) 100 N discretized double notch spanning $.14 \leq \omega_c \leq .22$Hz (b) 1000 N discretized double notch spanning $.14 \leq \omega_c \leq .22$Hz

Figure 3.27: Tug vehicle frequency response to 2009 N thrust, with 2 discrete tether masses. Deep space

It is clear that simply discretizing the notch thrust profile is not overly effective for a deep space scenario. Higher levels of discretization are preferred to better approximate the continuous profile, but this defeats the purpose of discretizing: making a more realistic thrust profile. This type of profile should not be used for deep space implementation.

3.3.6.2 On-orbit Discretized Notch Performance

Even though the 100 N discretized thrust profile had better performance in a deep space environment, it is not realistic performance for a thruster. Therefore, the 1000 N discretization is used in the on-orbit analysis. The 1000 N discretized thrust profile is used, unaltered from its deep-space implementation.

Figure 3.28 shows the relative separation distance and tension present in the tethered-tug system for a continuous and discrete notch. (The continuous notch performance is the same from Figure 3.16(b) and is given here for ease of comparison.) As discussed previously the continuous notch tends to drift together. However, as shown by Figure 3.22(a) the two end masses do get very close. What is interesting about the discretized thrust profile, Figure 3.28(b), is that the 1000 N discretized thrust that did not work well in deep space, performs moderately in orbit, maintaining more separation distance between end bodies. This is likely due to larger differences in relative motion post-maneuver that cause the two craft to stay further separated.

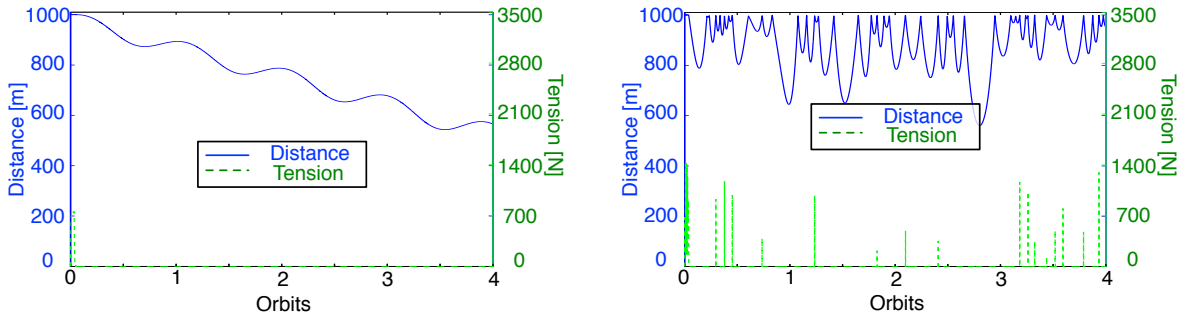

(a) *Continuous* double notch spanning $.14 \leq \omega_c \leq .22$Hz (b) 1000 N *discretized* double notch spanning $.14 \leq \omega_c \leq .22$Hz

Figure 3.28: Relative motion and tether tension response between tug and debris for four orbits. Tether $\omega_n = .19$ Hz. 2009 N thrust, with 2 discrete tether masses. On-orbit

Unfortunately, the end body rotation rates shown in Figure 3.29 are fairly high, about as high as the step input. This is not unexpected as the discretized notch profile is literally just a set of step inputs that excite motion in the system.

Figure 3.30 shows the angle between the end masses and their alignment to nadir. Using that angle as a metric for how well each thrusting method achieves the nadir alignment, it is clear that the 1000 N

discretized notch does oscillate about nadir. But, it is not clear that this method achieves gravity gradient any better than a step input, and it is certainly worse than the continuous notch that is induced to create formation oscillations.

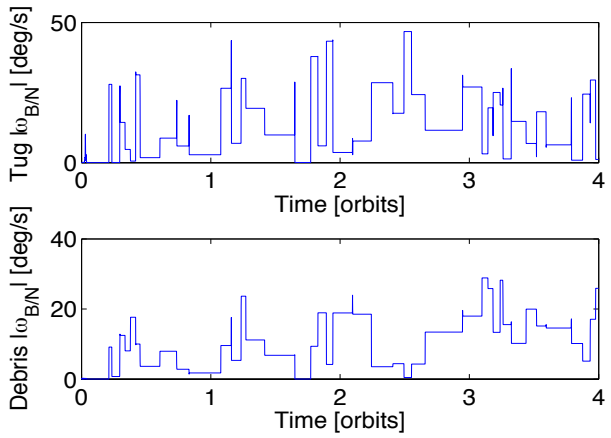

Figure 3.29: Discretized notch end body rotation rates over 4 orbits

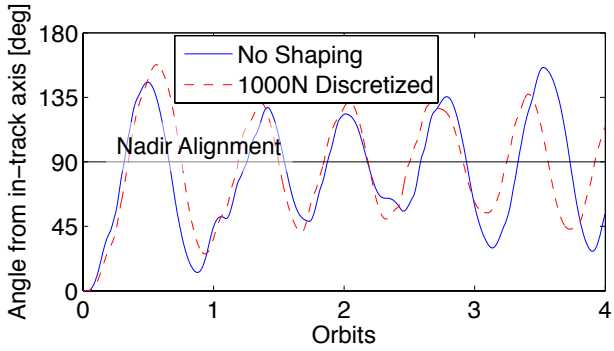

Figure 3.30: Discretized notch angle from along-track vector. 90^o is the radial vector

Therefore, the discretized notch has no guarantee that it could yield better performance than a step input. In the end, simply discretizing the continuous notch control is not overly effective. This motivates the use of a more rigorous impulsive input shaping control design.

3.4 Posicast Input Shaping

3.4.1 Concept

As shown by Singh,[77] a time delay system can be used as an open loop control on a system.

$$A_0 + \sum_{i=1}^{N} A_i e^{-sT_i} = 0 \tag{3.11}$$

where A_i are the amplitudes, T_i are the delay times, and s is the frequency. Singh demonstrates a number of Posicast methods to properly actuate a system, as well as make the control more robust to modeling errors. Singh also generally considers moving a system from one position to another. However, this section expands upon these works by formulating a robust Posicast, open-loop input shaper, that achieves a desired velocity without exciting natural frequencies. Because the first mode of the tethered system has been shown to be the most important,[33] a Posicast controller is developed only for the first mode.

The Posicast input shaping profile operates on the assumption that a step input control/thrust profile is given to the controller. The controller then takes the step and manipulates it so that it does not excite undesirable modes. Physically, this means that each change in the controller amplitude is timed to occur when there is no relative motion in the system, i.e. between the end bodies. The thrust profile created by the Posicast control is shown in Figure 3.25 but in the time scale shown, it is harder to differentiate between the impulsive profiles and the step input. It should be emphasized that the Posicast profile *does* behave similarly to the illustration in Figure 3.3(c).

3.4.2 Design

Assuming there are only two end bodies with a spring force between them, the equations of motion are simplified to:

$$\begin{aligned} \ddot{x}_1 &= \frac{1}{m_1}\left(K(x_2 - x_1 - L_0) - F_T\right) \\ \ddot{x}_2 &= \frac{1}{m_2}\left(-K(x_2 - x_1 - L_0)\right) \end{aligned} \tag{3.12}$$

This model will only recover the first mode of the system, but again, it is the most important to remove. The separation distance between the two end bodies is defined as $L = x_2 - x_1 - L_0$, where L_0 is the unstretched

length, a constant. The resulting tether flexing dynamics is written as

$$\begin{aligned} \ddot{L} = & \quad \ddot{x}_2 - \ddot{x}_1 \\ \ddot{L} = & \quad -K\frac{m_1+m_2}{m_1 m_2}L + \frac{F_T}{m_1} \end{aligned} \tag{3.13}$$

where $\sqrt{K\frac{m_1+m_2}{m_1 m_2}}$ is the natural frequency ω_n of a two body spring-mass system. Taking the Laplace Transform of the system in Eq. (3.13) gives the transfer function

$$H(s) = \frac{L}{u(s)} = \frac{1}{s^2 + K\frac{m_1+m_2}{m_1 m_2}} \tag{3.14}$$

Eq. (3.14) shows that the poles of the system occur at $s = \pm\sqrt{-K\frac{m_1+m_2}{m_1 m_2}} = \pm j\omega_n$, where $j = \sqrt{-1}$.

3.4.2.1 Two Body Example

Jasper et. al[34] demonstrate that a single step input thrust profile could (based upon the tether properties and rigid body end masses) be set to achieve the desired Δv without leaving the tether in tension. It turns out that this is a single amplitude Posicast system. An analytic solution to Eq. (3.13) is easily obtained and is given in Eq. (3.13).

$$L(t) = C_1 \cos(\omega_n t) + C_2 \sin(\omega_n t) + \frac{F_T}{\omega_n^2 m_1} \tag{3.15}$$

If the initial separation distance is assumed to be $L(t = 0) = L_0$ and the initial velocity to be zero, $\dot{L}(t = 0) = 0$, then $C_1 = L_0 - \frac{F_T}{m_1\omega_n^2}$ m, $C_2 = 0$ and the analytic solution for L becomes:

$$L(t) = (L_0 - \frac{F_T}{m_1\omega_n^2})\cos(\omega_n t) + \frac{F_T}{\omega_n^2 m_1} \tag{3.16}$$

Again, this solution is only valid when there is tension in the tether. Eq. (3.16) can provide insight into several of the basic behaviors of the system. If the cosine term reaches its maximum value of 1, then the separation distance simply becomes the initial separation L_0. Therefore, the separation will never become less than L_0 while thrusting. The maximum separation distance (when the cosine term becomes zero) is simply a ratio of the thrust, the natural frequency representing tether material properties, and the tug mass.

Insight into the oscillation periods and general dynamical behavior of the system is obtained through a deep-space analysis. During the constant thrusting period, the two masses oscillate, never approaching

each other closer than the unstretched tether length. When using the step input, the thrust stops whenever the desired Δv is achieved. The thrust force is frequently removed while the tether is still in tension, causing the system to collapse. To demonstrate how the thrusting behavior can be utilized to reduce collision potential, an example deep space simulation is run. Figure 3.31 uses a thrust of 5 kN, $m_1 = 2700$ kg, $m_2 = 1500$ kg and the tether properties of $E = 170$ GPa, $A = 8e^{-6}$ m^2 with an initial separation distance of $L_0 = 1000$ m between the two masses.

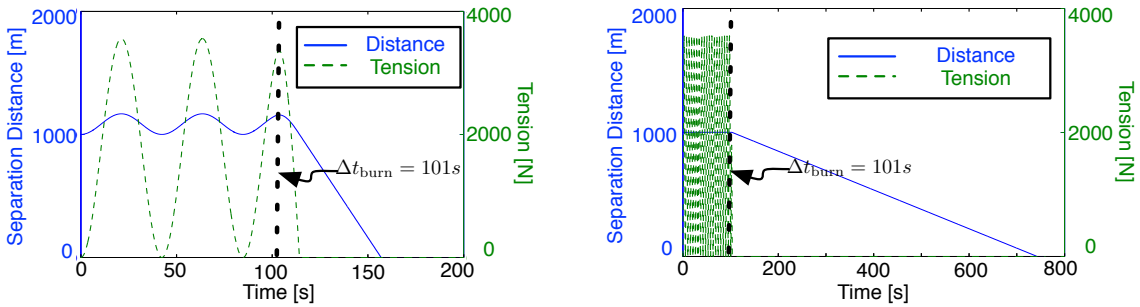

(a) Example motion with E = $3x10^9$ GPa. Collision at 157 s

(b) E = $170x10^9$ GPa. Collision at 741 s

Figure 3.31: Separation distance and tether tension in deep space, $\Delta t_{\text{burn}} = 101$ s, $\Delta v = 120$ m/s. $K_S = 1360$ N/m, T = 5kN

Figure 3.31 shows two different behaviors, Figure 3.31(a) with a low Young's Modulus, shows exaggerated motion, and Figure 3.31(b) shows more realistic motion of the tether system. Figure 3.31(a) demonstrates the periodic motion of both the tether and the tension. Once thrusting stops, remaining tension causes the craft to collapse in on themselves. Figure 3.31(b) behaves similarly, however the maximum separation is much smaller, reaching only about 1003 m due to the higher stiffness. The system then begins to collapse upon itself and collision occurs at about 741 seconds. During the thrusting period, it is important to note that the tether tension is always at or above zero. This corresponds to the separation distance always being at, or greater than, L_0.

The peaks and valleys in the tension and separation distance (Figure 3.31(a)) lines are points when the velocities between the end masses are traveling at equal speed. To achieve the desired Δv and avoid collisions, the 'equal speed points' provide a metric for when to reduce all forces between the masses to zero. One possible option would be to cut the tether at the equal speed points because the acceleration on both

objects will be zero and they will continue at the same relative velocity i.e. zero. This helps to guarantee that collision will not occur. Cutting the tether is not proposed here, however, because a loose ended tether will make tracking difficult and it could be dangerous to leave a loose multi-kilometer tether in orbit for long durations. Therefore, designing a maneuver profile to make the equal speed point coincide with the desired Δv is a reasonable alternative to cutting the tether.

Starting from Eq. (3.16), its time derivative can be taken:

$$\dot{L} = -(L_0 - \frac{F_T}{\omega_n^2 m_1}) \sin(\omega_n t) \tag{3.17}$$

The relative velocity is zero, $\dot{L} = 0$, when the sine expression is zero. A desired Δv can be expressed in terms of the thrust F_T, the system mass $M = m_1 + m_2$, and the burn time Δt.

$$\Delta v = \frac{F_T}{M} \Delta t \tag{3.18}$$

Solving for Δt from Eq. (3.18) and substituting it into Eq. (3.17), an expression for the required thrust to make $\dot{L} = 0$ is found. Here n is any integer.

$$\arcsin 0 = \omega_n t = \omega_n \left(\frac{M}{F_T} \Delta v \right)$$

$$F_T = \frac{\omega_n \Delta v M}{\arcsin 0} = \frac{\omega_n \Delta v M}{n\pi} \tag{3.19}$$

As might be expected, the number of oscillations made during thrusting are directly related to the integer used for n ($20\pi = 10 * 2\pi = 10$ oscillations). Because the system does not start in tension, even n values relate to an unstretched tether, equal speed point. Odd n values relate to maximum stretch, equal speed points therefore, even n values should be used. The relative velocity between the two craft can be all but zeroed simply by selection of thrust and/or time of burn, for a given spring-mass system, thus reducing the likelihood of a collision.

The development given in Eq. (3.15) - (3.19) produce something similar to a single amplitude Posicast system. However, the more rigorous development in the following section produces a more capable control that does not require an analytic solution to the system's motion, as in Eq. (3.15), and it can be made more robust to errors in the system model.

3.4.2.2 Detailed Posicast Design

The most basic Posicast controller uses only one time delay and is solved as an example. A single delay takes the form

$$A_0 + A_1 e^{-sT} = 0 \tag{3.20}$$

Plugging in $s = \pm j\omega_n$ to Eq. (3.20) the exponential term can be written as

$$e^{j\omega_n T} = \cos(\omega_n T) + j\sin(\omega_n T) \tag{3.21}$$

To solve the system, Eq. (3.21) is placed back into Eq. (3.20) and separated into real and imaginary components.

$$\begin{aligned} \text{Real} \qquad & A_0 + A_1\cos(\omega_n T) = 0 \\ \text{Imaginary} \qquad & A_1\sin(\omega_n T) = 0 \end{aligned} \tag{3.22}$$

This quickly results in the solutions for A_0 and T if A_1 is defined to equal 1, the maximum normalized input.

$$\begin{aligned} T &= (2n-1)\tfrac{\pi}{\omega_n} \\ A_0 &= -\cos(\omega_n T) = -\cos\left((2n-1)\pi\right) \end{aligned} \tag{3.23}$$

Note that the time T in Eq. (3.23) relates to the same time it takes to complete n oscillations, as seen in Figure 3.31(a).

3.4.3 Adding Robustness

The time delay control from Eq. (3.20) is very sensitive to modeling errors, therefore several delays are given to make the system more robust. To make the system solvable, Singh[77] specifies that each time delay is only a multiple of the single delay T, from Eq. (3.23). The delay time T can change, however, adding this as a variable gives too many variables for the number of constraints that can be applied to the system. Thus the selection of a constant T is desirable, and comes from Eq. (3.23). The controller designed for the tethered tug system is shown in Eq. (3.24).

$$A_0 + A_1 e^{-sT} + A_2 e^{-2sT} + A_3 e^{-3sT} + A_4 e^{-4sT} = 0 \tag{3.24}$$

To solve this system for the impulse amplitudes, A_i, several equations are required. Note that implementing the system in Eq. (3.24) would require 5 thrusters, one for each amplitude A_i. The real and imaginary parts are found again, as in Eq. (3.22).

$$\begin{aligned} \text{Real} \qquad & A_0 + A_1\cos(\omega_n T) + A_2\cos(2\omega_n T) + A_3\cos(3\omega_n T) + A_4\cos(4\omega_n T) = 0 \\ \text{Imaginary} \qquad & A_1\sin(\omega_n T) + A_2\sin(2\omega_n T) + A_3\sin(3\omega_n T) + A_4\sin(4\omega_n T) = 0 \end{aligned} \tag{3.25}$$

However three more constraints are defined:

$$\begin{aligned} \tfrac{d}{d\omega_n}(\text{Real}) &= 0 \\ \tfrac{d}{d\omega_n}(\text{Imaginary}) &= 0 \\ A_0 + A_1 + A_2 + A_3 + A_4 &= 1 \end{aligned} \tag{3.26}$$

The derivatives of the real and imaginary components of Eq. (3.24) add robustness by reducing the size of the residual vibration in the system after an input has been added (see Figure 3.32). The constraint that all of the amplitudes sum to one is used so that the input is not scaled but equal to its full value after all delays have occurred. Solving this system of equations, the amplitudes are found to be

$$\begin{aligned} A_0 &= \tfrac{1}{16}\csc\left(\tfrac{T\omega_n}{2}\right)^4 \\ A_1 &= -\tfrac{1}{4}\cos(T\omega_n)\csc\left(\tfrac{T\omega_n}{2}\right)^4 \\ A_2 &= \tfrac{1}{8}(2+\cos(2T\omega_n))\csc\left(\tfrac{T\omega_n}{2}\right)^4 \\ A_3 &= -\tfrac{1}{4}\cos(T\omega_n)\csc\left(\tfrac{T\omega_n}{2}\right)^4 \\ A_4 &= \tfrac{1}{16}\csc\left(\tfrac{T\omega_n}{2}\right)^4 \end{aligned} \tag{3.27}$$

To turn this development into a velocity control instead of a position control, the amplitudes from Eq. (3.27) are used at the beginning and end of the step input thrust profile to achieve a ramping on and off as shown in Figure 3.3(c). The amplitudes increase, summing from A_0 to A_4,hold at the maximum amplitude of the input for the thrust duration, and then decrease from A_4 to zero. For example, a three thrust

velocity control would require:

t = 0	Thrust = A_0
t = T	Thrust = $A_0 + A_1$
t = 2 T	Thrust = $A_0 + A_1 + A_2$
t = T_{burn}	Thrust = $A_0 + A_1$
t = T + T_{burn}	Thrust = A_0
t = 2 T + T_{burn}	Thrust = 0

Here, T_{burn} is the approximate burn time required by Eq. (3.18). The duration of the burn is nearly the same as the step input but is extended by $8T$ to account for the ramp on/off behavior.

To demonstrate why a 5 thrust level system is used in Eq. (3.24), versus the two impulse version of Eq. (3.20), their expected vibration amplitudes are compared. These amplitudes can be expressed as:[80]

$$A = \sqrt{\sum_{i=0}^{B}(A_i \cos(\omega_n T_i))^2 + \sum_{i=0}^{B}(A_i \sin(\omega_n T_i))^2} \tag{3.28}$$

where T_i are the times of the impulses A_i and ω_n is the natural frequency. (For the 2 impulse case, i goes to $B = 2$ while i goes to $B = 5$ for the 5 impulse case.) Summing these up over a range of natural frequencies, due to uncertain debris mass, the expected response of each system can be demonstrated. Figure 3.32 shows the percentage remaining vibration in the tethered-tug system, given the two different Posicast controls. It is clear from Figure 3.32 that as debris mass changes, the residual vibration is much smaller for the multi-impulse control, versus the two impulse control. Variations on the order of 40% can be expected from the non-robust method while the robust 5 impulse control only experiences about 0.3% variation across the expected mass range. Thus, the 5 impulse control is a major improvement.

Figure 3.32 also shows the effect of the constraints in Eq. (3.26). The robust Posicast, Figure 3.32(b), has a much more flat response to changes in debris than the 2 thrust level control, Figure 3.32(a). By setting the real and imaginary components of the transfer function to zero the control zeros the system response at the expected system properties. Zeroing the derivatives of the transfer function, flattens the response of the Posicast to a wider range of system properties.

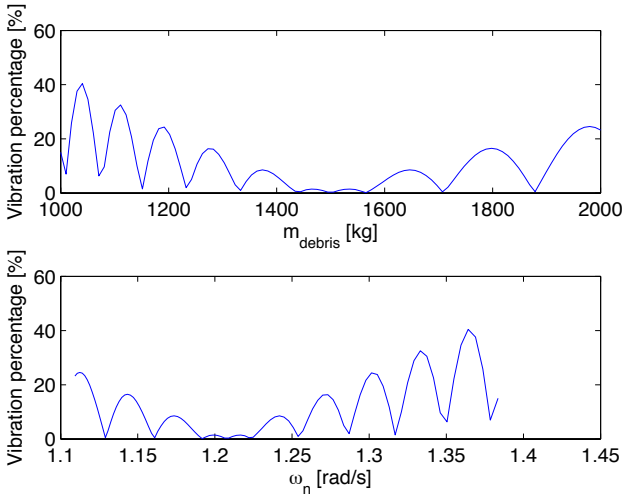

(a) 2 thrust level Posicast, Eq (3.20)

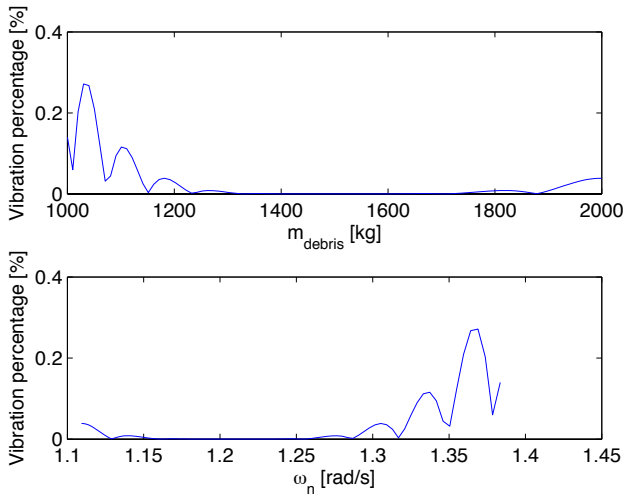

(b) 5 thrust level (robust) Posicast, Eq (3.24)

Figure 3.32: Residual vibration (percentage) from each Posicast method. Debris mass varies between 1000 kg and 2000 kg (nominal at 1500 kg, $\omega_n = 1.21$ rad/s).

3.4.4 Deep Space Performance

Note that the simulations shown utilize the following:

- The attitude on the tug (m_1) is maintained while thrusting occurs
- The Δv applied is equal to 100 m/s. Based upon input-shaping method, this can vary the thrusting duration
- Two tether masses and two rigid end bodies are used for this study

The time T that results from Eq. (3.23) is about 2.83 s and is used to implement the profile of Eq. (3.24). This means that the Posicast amplitudes change, using T as the baseline actuation time. For a five step Posicast system, the ramp on or off takes just over 14 s

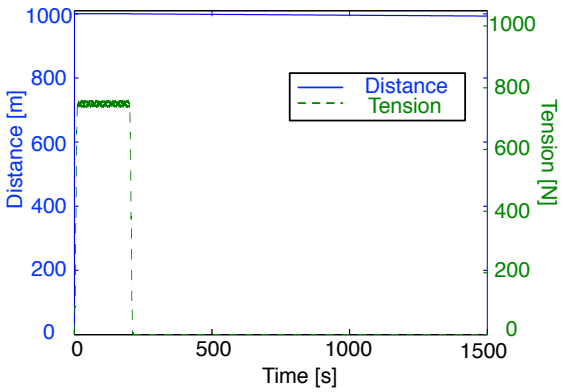

Figure 3.33: Relative motion and tether tension response between tug and debris. *Robust Posicast* thrust shaping, Eq. (3.24). Expected debris mass of 2000 kg ($\omega_n = 0.17$ Hz), actual mass is 1500 kg ($\omega_n = 0.19$ Hz). 2009 N thrust, with 2 discrete tether masses. Deep space

When considering the impulsive input shaping method in Figure 3.33, it can be seen that this thrust profile (Figure 3.25) produces very desirable behavior, even in the presence of a larger debris mass than expected. The Posicast controller only sees about 7 m of drift over the time span considered. These results are exciting because they demonstrate that input shaping controllers can be designed with profiles that are more reasonable for current-day engine capabilities.

Figure 3.34 shows the frequency domain response of the tug mass, given the Posicast thrust profile. Unlike the step input profile in Figure 3.9(a) that excites the modes of the tethered-tug system, Figure 3.34

shows the Posicast frequency response, which shows a very attenuated fundamental mode (0.19 Hz). The Posicast response is comparable to the continuous double notch in Figure 3.14(b). This again demonstrates that impulsive input shaping is a viable method to controlling the tethered-tug system. While some other frequencies do appear amplified, they are not around the fundamental mode of the system, and therefore do not adversely affect the system as modeled.

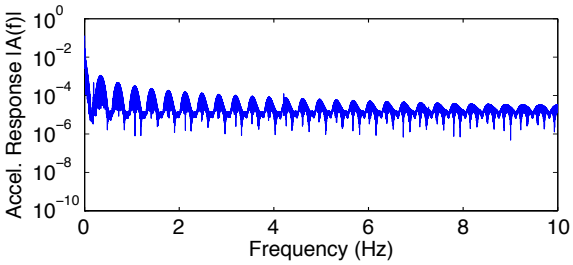

Figure 3.34: Tug vehicle frequency response to *Robust Posicast* 2009 N thrust, with 2 discrete tether masses. Deep space

3.4.5 On-orbit Performance

Taking the Robust Posicast thrust profile, unaltered from the deep-space implementation, on-orbit simulations are run. Figure 3.35 shows the Robust Posicast performance. The control profile again demonstrates admirable performance because the end bodies do not approach each other, as occurs with the continuous double notch in Figure 3.16(b). This is due to the fact that the formation enters into a tumble, shown in Figure 3.37. Further, the Posicast response appears are more benign experiencing lower tension (100 N versus 700 N and 1400 N for the continuous and discrete notch profiles, respectively) and the system quickly settles into a tumble, with end body separations near the full length of the tether.

The rotation rates of the end bodies is also relatively small as shown in Figure 3.36. The rates here are generally less than 5^o/sec but the notch with the radial thrust has some rotation rates between ten to twenty degrees per second and the discretized notch has rates reaching 45^o/sec. While the rates in Figure 3.36 change quickly, it is because the tether is constantly pulling the masses back in alignment so the masses never really complete a full rotation, avoiding the potential of wrapping in the tether.

Figure 3.37 shows the angle between the end masses and their alignment to nadir. The step input (no

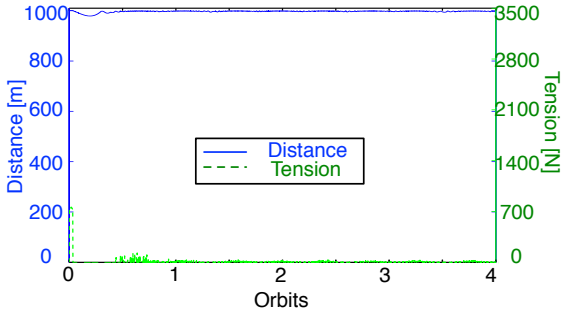

Figure 3.35: *Robust Posicast* relative motion and tether tension response between tug and debris for four orbits. Tether $\omega_n = 0.19$ Hz. 2009 N thrust, with 2 discrete tether masses. On-orbit

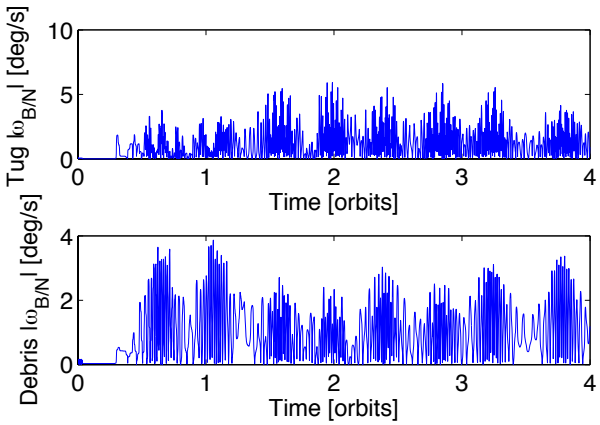

Figure 3.36: *Robust Posicast* end body rotation rates over 4 orbits

shaping) does not reach a steady gravity gradient motion and has much more dynamic response, compared to Figure 3.16.[33] The Robust Posicast profile settles into a tumble quickly ensuring the end masses stay separated.

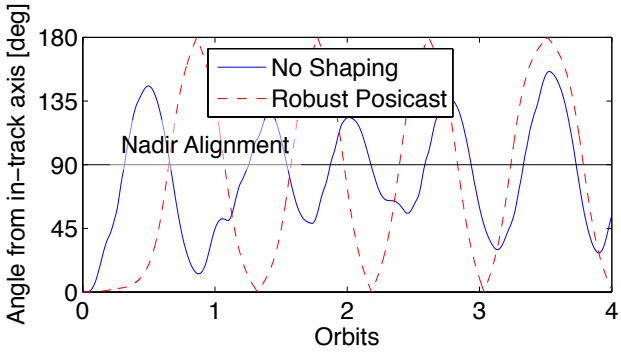

Figure 3.37: *Robust Posicast* angle from along-track vector. 90^o is the radial vector

3.5 Bang-Bang Input Shaping

3.5.1 Concept

The bang-off-bang controller creates a profile that can be implemented by a single thruster that can repeatably be turned on and off. This method also assumes that a step input is given to the controller that is then modified to not excite system modes. Singh[77] demonstrates several ways to create a bang-off-bang controller; however, the basic principle is to find a linear system's state transition matrix and control matrix. Combining these matrices with several constraints, similar to those in Eq. (3.26), yields a system that can be solved as a linear programming problem. Full details are given by Singh, however, an abbreviated derivation is given for clarity. Further, the thrust profile is shown in Figure 3.25 but is better illustrated by Figure 3.3(d).

3.5.2 Design

Given initial and final conditions, $\boldsymbol{x}_0$ and $\boldsymbol{x}_f$ and a system of the form in Eq. (2.5), the problem can be set up as follows. We wish to minimize the maneuver time, so

$$\text{Minimize } f^T t \tag{3.29}$$

where t is the maneuver time vector and f is a vector that defines the given time we wish to minimize. In this case, since it is desired to minimize the total time, f is a vector of zeros except the last value, which is a 1 corresponding to the last time. The continuous linear system of Eq. (2.5) is then discretized, obtaining

$$\boldsymbol{x}_{k+1} = [A_D]\boldsymbol{x}_k + [B_D]\boldsymbol{u}_k \tag{3.30}$$

where $[A_D]$ is the discrete dynamics matrix obtained from Eq. (3.31), $[B_D]$ is the discrete control matrix obtained from Eq. (3.32) and T is the discretization time.

$$[A_D] = e^{AT} \tag{3.31}$$

$$[B_D] = \left(\int_{\tau=0}^{\tau=T} e^{A\tau} d\tau \right) B \tag{3.32}$$

Writing the system in terms of the initial state ($\boldsymbol{x}_0$) gives:

$$\boldsymbol{x}_{k+1} = [A_D]^k \boldsymbol{x}_0 + \sum_{i=1}^{k} [A_D]^{k-i} [B_D] \boldsymbol{u}_i \tag{3.33}$$

Assuming the final and initial state are known, the summation of inputs can be rewritten and solved for as a matrix giving:

$$\begin{bmatrix} [A_D]^{N-1}[B_D] & [A_D]^{N-2}[B_D] & \cdots & [A_D][B_D] & [B_D] \end{bmatrix} \begin{bmatrix} u_1 \\ u_2 \\ \vdots \\ u_N \end{bmatrix} = \boldsymbol{x}_f - [A_D]^N \boldsymbol{x}_0 \tag{3.34}$$

or equivalently

$$[M(A_D, B_D)]\boldsymbol{u} = b(\boldsymbol{x}_0, \boldsymbol{x}_f, [A_D]) \tag{3.35}$$

The system given in Eq. (3.34) allows the user to specify the initial and final conditions ($\boldsymbol{x}_0$, $\boldsymbol{x}_f$) and it is solvable using linear programming techniques, in the form of $M\boldsymbol{u} = b$. However, to be useful as a bang-off-bang system, several additional constraints are required. One is that the inputs end in either zero or one. This is enforced by adding a row to $[M]$ that is all zeros except for the last column, which is a one. The $[b]$ matrix also has an additional value added to the end that is either a zero or one. This allows

for the final control value u_N to be specified as whatever value is designated in $[b]$, off (0) or on (1). The second constraint is on the input sizes. To create a bang-off-bang control, the inputs $\boldsymbol{u}$ are required to be bounded between zero and one. The value of one is used so that the user defined input is used in its entirety and not scaled. For this particular implementation, the system is discretized into more than 300 steps over the minimum cost time determined by the linear programming routine. The large number of discretizations (over only several seconds for each ON or OFF segment) allows accuracy in the solution. If the discretization size were bigger, poor results can ensure.

To create a velocity control bang-off-bang profile, the linear programming problem is solved twice. To begin thrusting while avoiding exciting system modes:

- $\boldsymbol{x}_0 = 0$
- $\boldsymbol{x}_f = L_1$
- The final input u_N is specified to be 1

The value L_1 is defined simply from the approximate separation distances seen from the other control methods, like the continuous notch. The tether usually ends up stretching less than a meter, for a 1000 m tether. The selection of this value does not drastically affect the performance of the system, unless it is larger than the stretch distance possible given the thrust magnitude and the tether material properties. The final control input is kept at one for the burn duration to achieve the desired Δv (computed from Eq. (3.18)). The linear programming problem is then solved again to end thrusting using:

- $\boldsymbol{x}_0 = L_1$
- $\boldsymbol{x}_f = 0$
- The final input u_N is specified to be 0

The beginning and ending bang-off-bang profiles are then placed at the beginning and end of the step input thrust profile. This allows for proper relative motion reduction with the desired Δv. The exact thrust profile used is shown in Figure 3.25 however the switch times are small enough that they are hard to see on the time scale shown. The exact timing is as follows:

- t = 0, ON
- t = 0.6849, OFF
- t = 1.6438, ON
- t = 198.35, OFF
- t = 199.31, ON
- t = 200, OFF

Rocket engines are capable of lighting within fractions of a second, therefore achieving the specific timing of the bang-off-bang is probably possible. However, re-lighting engines is a significant challenge so a bang-off-bang profile would likely require some engine development.

3.5.3 Deep Space Performance

Note that the simulations shown utilize the following:

- The attitude on the tug (m_1) is maintained while thrusting occurs
- The Δv applied is equal to 100 m/s. Based upon input-shaping method, this can vary the thrusting duration
- Two tether masses and two rigid end bodies are used for this study

The time T that results from Eq. (3.23) and is used to implement the profiles of Eq. (3.34) is about 2.83 s. This means that the bang-bang profile switches using T as the baseline actuation time. Figure 3.38 shows the bang-off-bang non-continuous thrust system. Figure 3.25 gives the profile used.

When considering the impulsive input shaping methods in Figure 3.38, it can be seen that this thrust profile (Figure 3.25) produces desirable behavior, similar to the Posicast system. The bang-off-bang profile sees about 100 m of drift, however the debris mass is 500 kg from the expected value and the bang-off-bang profile is not designed to be robust to system model errors. Still, the bang-off-bang profile behaves fairly desirably.

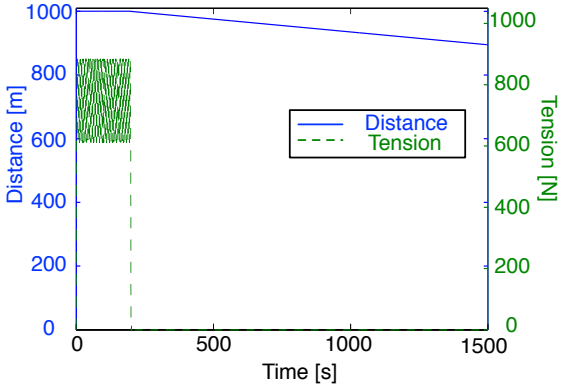

Figure 3.38: Relative motion and tether tension response between tug and debris using a *Bang-off-bang* thrust profile. Expected debris mass of 2000 kg ($\omega_n = 0.17$ Hz), actual mass is 1500 kg ($\omega_n = 0.19$ Hz). 2009 N thrust, with 2 discrete tether masses. Deep space

Figure 3.39 shows the bang-off-bang frequency response which does not see nearly as much attenuation as the Posicast or double notch profile, but it does attenuate the fundamental mode enough to see reduced relative motion between the two bodies, as shown in Figure 3.38. Again, this is due to imperfect debris mass knowledge.

3.5.4 On-orbit Performance

Taking the bang-off-bang thrust profile, unaltered from the deep-space implementation, on-orbit simulations are run. Figure 3.40 shows the bang-off-bang performance. The bang-bang profile sees significant motion between the end bodies, however separation distances remain large. Tensions are also about the same size as those seen in the notch implementation, but larger than the Posicast.

When considering the end body rotation rates in Figure 3.41, it is obvious that they are fairly large. These are again, about the same size as the step input meaning that the end bodies spin quite fast and have the potential to wrap up in the tether.

Figure 3.42 shows the angle between the end masses and their alignment to nadir. The bang-off-bang profile oscillates about the nadir vector but it is not a consistent oscillation, similar to the unshaped input.

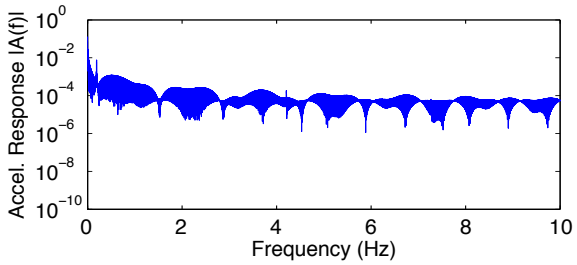

Figure 3.39: Tug vehicle frequency response to a *Bang-off-bang* 2009 N thrust, with 2 discrete tether masses. Deep space

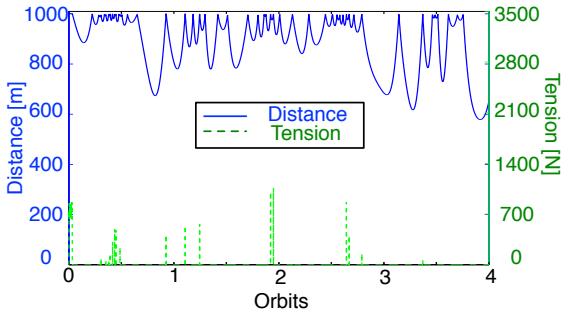

Figure 3.40: *Bang-off-bang* relative motion and tether tension response between tug and debris for four orbits. Tether $\omega_n = 0.19$ Hz. 2009 N thrust, with 2 discrete tether masses. On-orbit

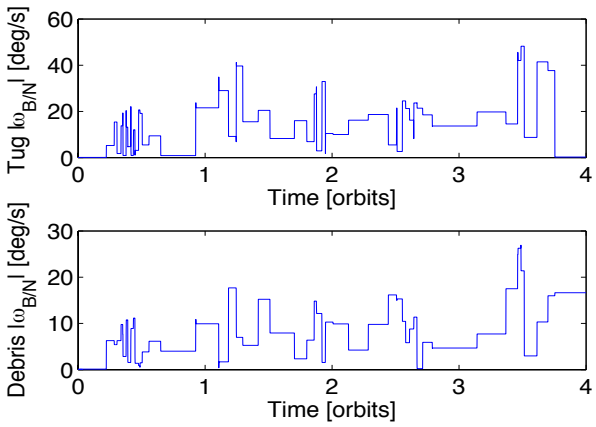

Figure 3.41: *Bang-off-bang* end body rotation rates over 4 orbits

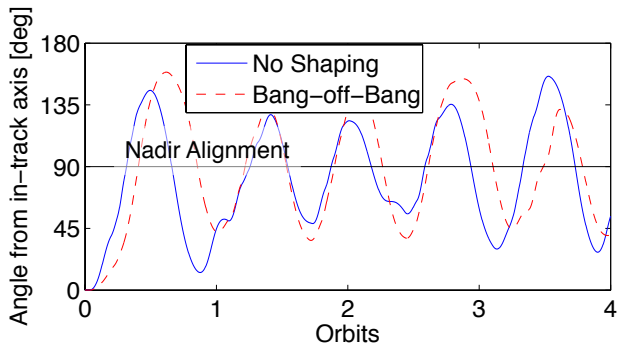

Figure 3.42: Bang-off-bang angle from along-track vector. 90^o is the radial vector

3.6 Conclusions

A step input (impulsive) thrust profile is shown to be inadequate for a tethered ADR system due to the chaotic motion, collision potential, and relatively high tether tensions induced. The excitement of, primarily, the tether's first mode causes the majority of the relative motion between the end bodies. Open-loop input shaping of only the first mode can largely negate relative motion between the end bodies once the thrust maneuver is performed. This helps the system stay separated in deep space, or achieve a tumbling or gravity gradient motion in orbit. While the continuous notch input shaping performs well by limiting relative velocity between end bodies, it still experiences a collapse in the formation over time. This can be corrected by inducing a spin but that adds other complications to the motion, such as high end body spin rates. The impulsive Posicast and bang-off-bang profiles are more achievable for high-thrust rockets. The bang-off-bang profile performs reasonably well in deep space but is not nearly as robust while in orbit. However, the Posicast filter creates desirable tumbling motion, large end body separations, and relatively low end body spin rates. This makes the Posicast control the most attractive input shaping method.

Chapter 4

Tether Design

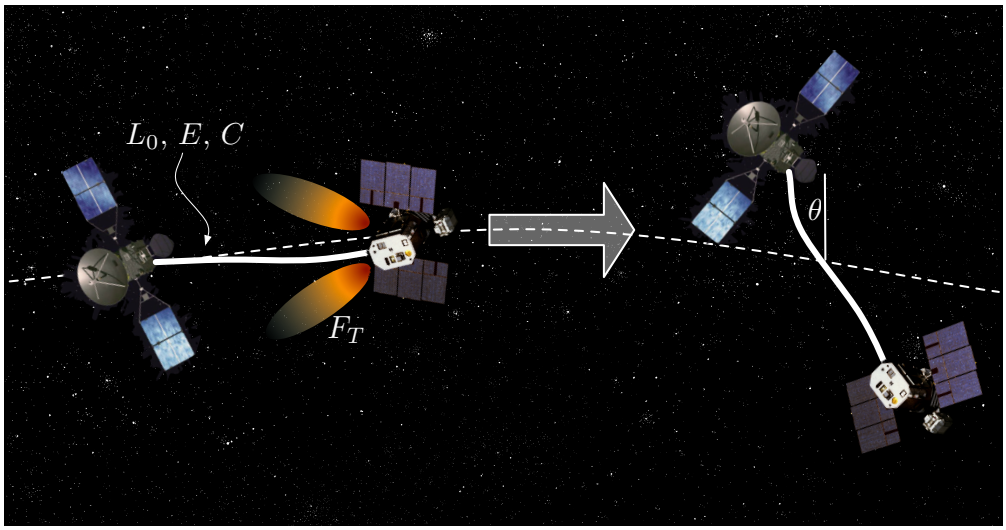

Figure 4.1: Tether properties considered for on orbit towing to achieve gravity gradient oscillation about θ

Using an input shaped control profile yields good results for reduced end body relative motion and collision avoidance as shown in Chapter 3 and References 33 and 32. This chapter expands the discussion and considers how tether properties affect the end body behavior with, and without input shaping. There are three parameters that are directly considered in this chapter and their affects on avoiding collisions. Specifically, tether length, L_0, is considered to see if there is a length that is too short or too long. The tether damping coefficient, C, and modulus of elasticity, E, are considered to see if these parameters can substitute for thrust input shaping so that a step thrust profile can be used. The effect of changes to combinations of these tether properties will be analyzed based upon the desired capability to avoid collisions between the

large end-bodies while achieving a tumbling formation or gravity gradient motion. Figure 4.1 shows the desired behavior of the system and the tether properties that are to be considered.

The system model from Chapter 2 is used, including damping. The robust Posicast is used here because it provided some of the best behavior for the system in Chapter 3.4. When damping is used, both the Posicast and step inputs are considered together to determine how much of an improvement damping provides. First, each tether property is varied individually and the behavior of the system is studied. Then, simultaneous changes to damping and elasticity are explored.

4.1 Considered Tether Properties

The basic properties for the system are given in Table 2.1. These are the baseline values and are varied depending upon the simulation. As each tether property is varied, the change of the fundamental frequency for the system is given in the second column of Table 4.1 - 4.2. This frequency is the frequency used by the input shaping methods (Chapter 3.4). Tether mass changes as the unstretched length changes and the volume of the tether is assumed to be a cylinder.

4.1.1 Length Trade Space

The use of tethers in space has received considerable study.[13,15,36] They have also been demonstrated on orbit with large tether lengths. The Small Expendable Deployer System (SEDS)[14] experiments were launched by NASA on Delta-II rockets. These tethers spanned up to 20 km kilometers. The Space Shuttle Tethered Space System (TSS) missions deployed tethers and TSS-2 reached a tether length of nearly 20 km[191]. Several other missions have shown shorter deployments. It is therefore likely that the tether length for the tethered-tug system can span a large range of distances.

The tether lengths considered are developed based upon safe distance considerations and previous flight missions.[14,19] Based upon the relative motion often seen in previous studies,[33,34] the minimum separation distance between the two end bodies should be at least 100 m. The maximum distance of 10 km is within demonstrated tether lengths from previous flight missions. The natural frequency and change in

[1] http://www.nasa.gov/mission_pages/shuttle/shuttlemissions/archives/sts-75.html

tether mass (Eq. (3.6)) is given in Table 4.1.

Table 4.1: Change in natural frequency, and mass with tether length, L_0. $E = 170$ GPa, $C = 0\ \frac{kg}{s}$

L_0 (m)	ω_n (Hz)	Tether Mass (kg)
100	0.617	1.18
500	0.273	5.91
1000	0.192	11.82
2000	0.136	23.64
5000	0.086	59.11
10000	0.061	118.22

4.1.2 Elasticity Trade Space

Young's modulus of elasticity affects the tether's stiffness, K_S (Eq. (2.8)), therefore it is an important property to consider. Tethers can be made from a variety of materials but the material frequently considered for use in space tethers is Kevlar.[3,13,19,26,41] Assuming Kevlar is the primary load bearing material, it has a fairly wide range of possible moduli to consider. This range has been explored through the use of *www.matweb.com*[2]. The natural frequency, and its sensitivity to change in debris mass (Eq. (3.6)) is given in Table 4.2.

Table 4.2: Change in natural frequency with Young's modulus, E. $L_0 = 1$ km, $C = 0\ \frac{kg}{s}$

E (GPa)	ω_n (Hz)
27	0.0767
60.5	0.115
94	0.143
161	0.187
194.5	0.206
228	0.223

4.1.3 Damping Trade Space

Damping in tethers has received much less attention than the modeling of the undamped dynamics. However, there have been some theoretical, terrestrial, and on orbit experimental analyses done concerning damping.[26,45] Characterizing the damping present in a tether, especially long tethers on orbit is challenging.

[2] http://www.matweb.com/index.aspx

Still, damping ranges can be bounded[10,26] and the value of damping can also potentially be designed to reduce several of the modes of the tether.[45] A potential range of longitudinal damping coefficients is explored for the system.

Unfortunately, there is not much good data on the damping that occurred with tethers that have flown.[3,26] The lower bound on damping is based upon 'structural' properties which depend upon how the tether is built. The upper bound is based upon viscous forces internal to the tether and external forces (such as atmospheric drag). This gives a range on C between 1×10^{-3} and about 1.10, for the tethered-tug system.[26] Materials other than Kevlar, like Zylong have shown natural damping of about 0.08.[10] However, making the assumption that the tether can be designed to achieve various material properties, a wider range will be explored. Specifically, larger values of C will be used. (Achieving a damping of $C = 8$ kg/s may be optimistic but the idea is to determine when damping can have a significant affect.) Longitudinal damping is considered in this thesis and transverse tether damping is set to zero because it is much smaller.

Table 4.3: Change in natural frequency with tether damping, C. $L_0 = 1$ km, $E = 170$ GPa.

C ($\frac{kg}{s}$)	ω_d (Hz)
0.1	0.192470203
1	0.192470203
2	0.192470198
4	0.192470184
8	0.192469904
10	0.192469735

4.2 Modifications to Posicast Control

With damping, the Posicast control is modified slightly. Chapter 3.4 assumes that damping is zero, leaving only oscillatory behavior. With damping the frequency has both real and imaginary components:

$$s = \epsilon \pm j\omega_d \tag{4.1}$$

The robust Posicast control, shown again for ease of reference in Eq. (4.2), is altered to include the addition of the real component of the Eigen value.

$$A_0 + A_1 e^{-sT} + A_2 e^{-2sT} + A_3 e^{-3sT} + A_4 e^{-4sT} = 0 \tag{4.2}$$

The constraints placed on the solution of Eq. (4.2) now become:

$$\begin{aligned} \text{Real} \quad & A_0 + A_1 e^{-\epsilon T}\cos(\omega_d T) + A_2 e^{-2\epsilon T}\cos(2\omega_d T) + A_3 e^{-3\epsilon T}\cos(3\omega_d T) \\ & + A_4 e^{-4\epsilon T}\cos(4\omega_d T) = 0 \\ \text{Imaginary} \quad & A_1 e^{-\epsilon T}\sin(\omega_d T) + A_2 e^{-2\epsilon T}\sin(2\omega_d T) + A_3 e^{-3\epsilon T}\sin(3\omega_d T) \\ & + A_4 e^{-4\epsilon T}\sin(4\omega_d T) = 0 \end{aligned} \tag{4.3}$$

The derivative constraints to flatten the vibration response and add robustness are still:

$$\begin{aligned} \tfrac{\delta}{\delta\omega_d}(\text{Real}) &= 0 \\ \tfrac{\delta}{\delta\omega_d}(\text{Imaginary}) &= 0 \\ A_0 + A_1 + A_2 + A_3 + A_4 &= 1 \end{aligned} \tag{4.4}$$

Finally, the new thrust levels are expressed as:

$$\begin{aligned} A_0 &= \tfrac{1}{(1+e^{2T\epsilon}-2e^{T\epsilon}\cos(T\omega_d))^2} \\ A_1 &= -\tfrac{e^{-T\epsilon}\cos(T\omega_d)}{(\cos(T\omega_d)-\cosh(T\epsilon))^2} \\ A_2 &= \tfrac{2+\cos(2T\omega_d)}{2(\cos(T\omega_d)-\cosh(T\epsilon))^2} \\ A_3 &= -\tfrac{e^{T\epsilon}\cos(T\omega_d)}{(\cos(T\omega_d)-\cosh(T\epsilon))^2} \\ A_4 &= \tfrac{e^{4T\epsilon}}{(1+e^{2T\epsilon}-2e^{T\epsilon}\cos(T\omega_d))^2} \end{aligned} \tag{4.5}$$

4.3 Tether Length

Figure 4.2 and Figure 4.3 show the relative separation of the tether-tug system end bodies, the angle from nadir, and the tether tension for the L_0 lengths in Table 4.1. A nadir/gravity gradient alignment is defined as the tethered-tug system oscillating about the nadir vector (0^o) while maintaining a separation distance between the end bodies of close to L_0. Note that the tension in the tether is scaled in each plot so that it properly fits the 'angle from nadir' axis. Therefore, if the tension is scaled by 0.5 and its value reads 90, the actual tension is 45 N. The tension is zero at an **angle** of 0^o.

Figure 4.2 demonstrates the general motion of the tethered-tug system using a step input compared to Figure 4.3 that uses the Posicast thrust profile. While Figure 4.2 does see some oscillation of the formation about the nadir vector, the separation distance between the end bodies is quite dynamic and the angle from

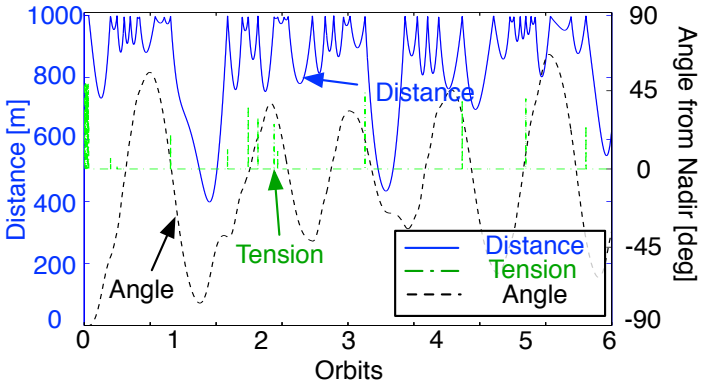

Figure 4.2: Relative motion and tether tension between tug and debris with a *step* input. $L_0 = 1$ km, $E = 170$ GPa and $C = 0\ \frac{kg}{s}$. The debris' expected mass is 1500 kg but it is actually 2000 kg in simulation. Tension scaled by 27.78. Tether length study.

nadir does not reach a consistent motion. The step input therefore this does not achieve tumbling or gravity gradient motion. Conversely, Figure 4.3 shows that some of the distances do achieve desirable motion and many do maintain large separations with small tensions.

Figure 4.3(a) achieves a gravity gradient oscillation fairly quickly. While the end bodies continue to move relative to each other, they remain at nearly L_0. Figure 4.3(b) experiences similar behavior to the unaltered double notch filter in Figure 3.16(b) where the end bodies end up drifting relative to each other. Gravity gradient or tumbling formation motion is partially the result of having some relative velocity in the radial direction, post-thrust. This velocity helps to begin the formation's rotation. The slow drift in Figure 4.3(b) has less of this radial velocity, leaving the end bodies more or less in the along-track direction.

Figures 4.3(c) and 4.3(d) go into a tumble post-thrust, a desirable motion to avoid collision. However for $L_0 = 1$ km, near 4.5 orbits the formation appears to hold at near 90^o (both masses are aligned along-track), allowing the two masses to begin drifting closer together. As the two masses drift and re-tension the formation begins to settle into the desirable nadir motion. It has been observed that transitioning from tumbling to gravity gradient has a corresponding reduction in separation distance. Therefore, it is likely that the 1 km also settles to gravity gradient. However, Figure 4.3(e) and Figure 4.3(f) do not tumble or appear to achieve gravity gradient motion. It is interesting to note that the two furthest distances considered had the

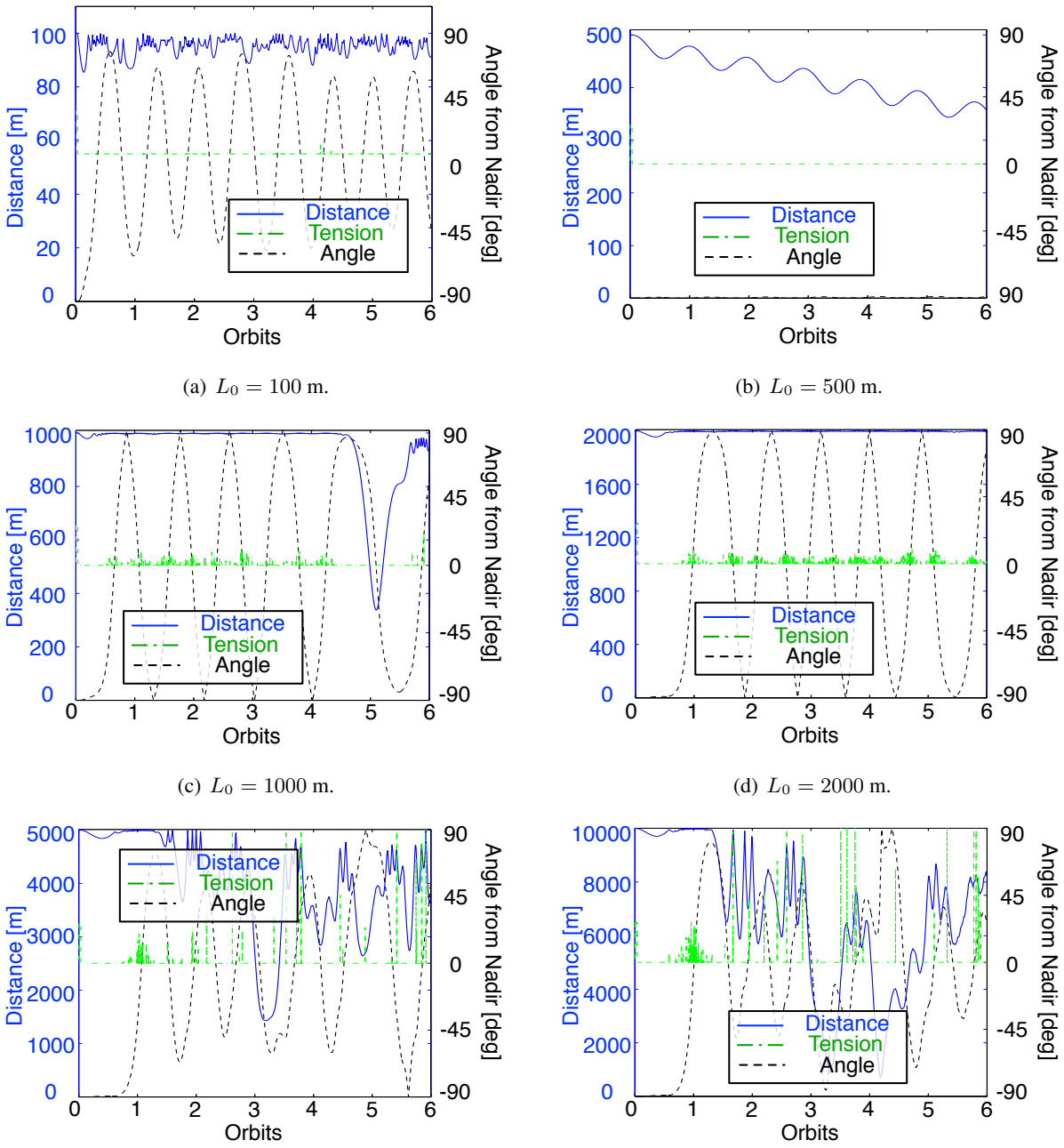

(a) $L_0 = 100$ m.

(b) $L_0 = 500$ m.

(c) $L_0 = 1000$ m.

(d) $L_0 = 2000$ m.

(e) $L_0 = 5000$ m.

(f) $L_0 = 10000$ m.

Figure 4.3: Relative motion and tether tension between tug and debris with a Posicast input. $E = 170$ GPa and $C = 0\ \frac{kg}{s}$. The debris' expected mass is 1500 kg but it is actually 2000 kg in simulation. Tension scaled by 27.78. Tether length study.

closest approaches showing that longer tethers do not guarantee further separation.

An example of the end body rotation rates is given in Figure 4.4. This behavior seems common for the

Posicast control with a tumble or gravity gradient motion. The transition from tumbling to gravity gradient can be seen on this plot as the constant spin rate between about 4.5 and 5.5 orbits. Table 4.4 summarizes

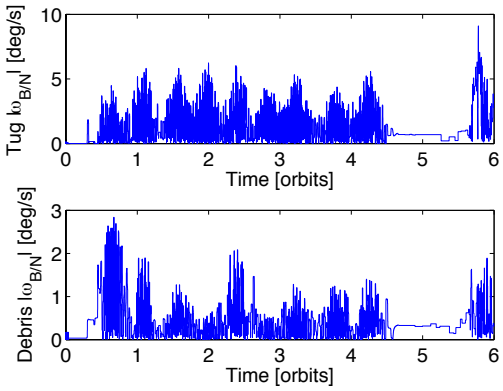

Figure 4.4: Rotation rate of end bodies for $L_0 = 1000$ m tether length study.

the average and standard deviation of the rotation rates from the results in Figure 4.3. The gravity gradient and tumbling rotation rates are all relatively small and the bodies generally do not make full rotations, but oscillate about their attachment point. The drifting end bodies in $L_0 = 500$ m have the smallest rotation rate, as expected. The longer distances see very large spin rates, induced by large tensions spinning up the bodies. This further demonstrates the poor performance of the 5000 m and 10000 m cases.

There are multiple observations made from this study that are summarized in the following paragraphs. First, when the angle becomes large, but the system does not tumble, the separation distance reduces. This is because at large angles the two bodies are nearly aligned in the along-track direction. Any velocity differences will cause drift between the two bodies, thus they begin to approach each other. The end bodies generally have enough distance in the radial direction to pass by each other. Eventually the tether catches them, causing gravity gradient motion. This behavior is consistent throughout all the results for each tether property. Generally, angles above about 70^o seem to cause this collapsing behavior.

Second, major dips in the separation distance only occur while an end body is above, and forward of, the center of mass of the system. Being in a higher orbit than the lower body, the forward body will drift (relatively) backwards. The lower body moves faster and drifts (relatively) forwards. In all simulations, after thrusting the tug always begins with a slightly higher relative velocity than the debris (due to the thruster

Table 4.4: End body rotation rate average and standard deviation for L_0 study. $E = 170$ GPa, $C = 0\ \frac{kg}{s}$

L_0 (m)	Body	Mean $\omega_{B/I}$ (deg/s)	Standard Deviation $\omega_{B/I}$ (deg/s)
100	Tug	0.663	0.505
	Debris	0.450	0.331
500	Tug	0.009	0.004
	Debris	0.080	0.004
1000	Tug	1.463	1.336
	Debris	0.499	0.450
2000	Tug	1.693	1.467
	Debris	1.461	1.190
5000	Tug	35.904	43.008
	Debris	39.538	31.970
10000	Tug	57.101	52.940
	Debris	54.219	44.571

and being in a slightly lower orbit). The tug then naturally increases in orbit altitude and begins swinging over the top of the formation. This causes the initial dip in relative separation distance and the transition to either tumbling or gravity gradient motion.

Third, the transition from a tumbling formation to gravity gradient has been observed to always be accompanied by a large rotation angle, that does not pass 90^o, and a reduction in the separation distance. When the bodies drift apart again and re-tension, they catch and begin the gravity gradient oscillation. The end bodies often experience higher rotation rates, at least temporarily, during the transition.

Fourth, this system is challenging to characterized because the initial conditions do not directly correlate to whether, or when, the formation will transition from a tumble to gravity gradient. This behavior is a complex interaction between position in orbit, relative end body states, and tension in the tether. What is encouraging is that if the system achieves a tumbling or gravity gradient oscillation, it stays that way. Thus, if these conditions can be achieved (through proper input shaping and/or selection of E, C, or L_0) the system reaches a desirable configuration.

The overall results from the length study are given in Table 4.5. A 'close approach' occurs when the end bodies approach each other. (Generally, it has been seen that using a step input causes poor performance, independent of tether length.) The Posicast input shaped thrust profile performs well. Still, not all of the lengths achieve a tumble or gravity gradient motion. It also appears that as tether length gets longer, the performance reduces and more relative motion occurs.

Table 4.5: Summary of tether length, L_0, study. $E = 170$ GPa, $C = 0$ $\frac{kg}{s}$

L_0 (m)	Gravity Gradient/Tumble	Notes
100	Grav. Gradient	
500	No	Drift between end bodies
1000	Tumble to Grav. Gradient	Transitions at 4.5 orbits
2000	Tumble	
5000	No	End body motion w/o oscillation
10000	No	Close approach of 44 m

4.4 Tether Stiffness

Figure 4.5 shows the relative motion, angle from nadir and tether tension of the tether-tug system. Figures 4.5(a), 4.5(c), and 4.5(e) all start in a tumble and begin to transition to gravity gradient motion. However, Figure 4.5(b) has drift between the end bodies, like the notch and the 500 m length results. Conversely, Figures 4.5(d) and 4.5(f) do not appear to settle into any obvious trend. As stated earlier, the timing of any re-tensioning events seems to be particularly important for whether or not the system achieves tumbling or gravity gradient motion.

Table 4.6 gives the average and standard deviation of the rotation rates for each E trial. Similar to the L_0 study, the rotation rates of the gravity gradient/tumbling behavior are relatively small and behave similar to Figure 4.4. The drifting rotation rates for $E = 60.5$ GPa are very small, just like all other drifting scenarios. The more dynamic behavior of $E = 161$ GPa and $E = 228$ GPa have generally higher rotation rates, and large deviations showing that they are undesirable.

Table 4.6: End body rotation rate average and standard deviation for E study. $L_0 = 1000$ m, $C = 0$ $\frac{kg}{s}$

E (GPa)	Body	Mean $\omega_{B/I}$ (deg/s)	Standard Deviation $\omega_{B/I}$ (deg/s)
27	Tug	1.724	1.901
	Debris	1.155	1.144
60.5	Tug	0.010	0.004
	Debris	0.0260	0.006
94	Tug	4.034	7.544
	Debris	1.353	2.365
160	Tug	6.269	6.633
	Debris	4.811	6.139
194.5	Tug	1.538	1.394
	Debris	1.110	0.935
228	Tug	7.888	9.520
	Debris	3.138	4.015

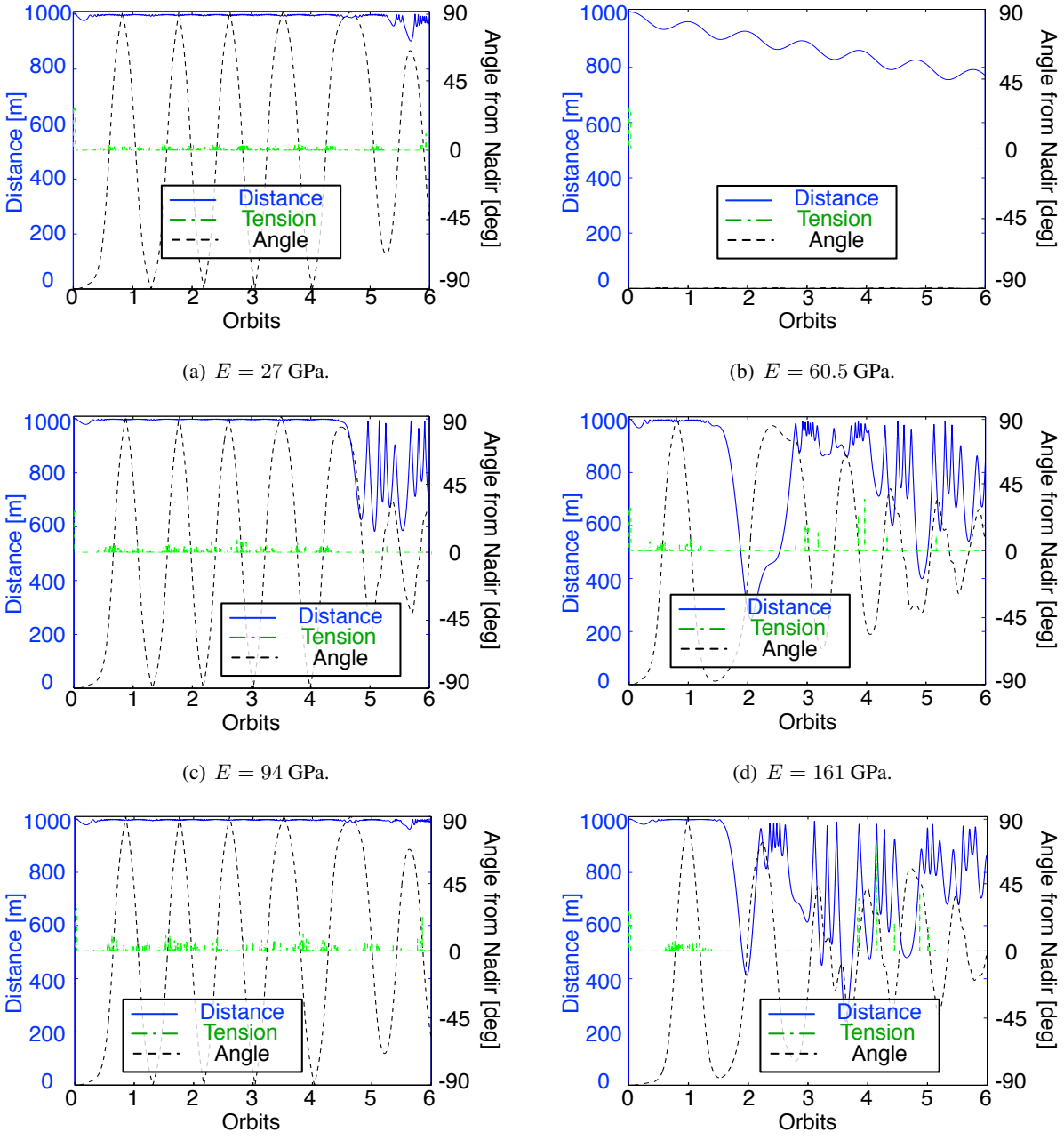

(a) $E = 27$ GPa.

(b) $E = 60.5$ GPa.

(c) $E = 94$ GPa.

(d) $E = 161$ GPa.

(e) $E = 194.5$ GPa.

(f) $E = 228$ GPa.

Figure 4.5: Relative motion and tether tension between tug and debris with a Posicast input. $L_0 = 1$ km, $C = 0\ \frac{kg}{s}$. The debris' expected mass is 1500 kg but it is actually 2000 kg in simulation. Tension scaled by 27.78. Stiffness study.

A summary of the results from the stiffness study are given in Table 4.7. Changes to elasticity does not seem to cause any discernible trends to the motion. Some of the motion is advantageous, some is not.

Table 4.7: Summary of tether stiffness, E, study. $L_0 = 1000$ m, $C = 0$ $\frac{kg}{s}$

E (GPa)	Gravity Gradient/Tumble	Notes
27	Tumble to Grav. Gradient	Transitions at about 5 orbits
60.5	No	Drift between end bodies
94	Tumble to Possible Grav. Gradient	Transitions at about 4.5 orbits
161	No	End body motion w/o constant oscillation
194.5	Tumble to Possible Grav. Gradient	Transitions at about 5 orbits
228	No	End body motion w/o constant oscillation

4.5 Longitudinal Damping

While the length and elasticity studies can produce ideal motion of the system with input shaping, the use of a step input consistently performs poorly. However, with the addition of damping, the step thrust profile may respond much better as damping can remove unwanted motion. This section considers both the robust Posicast and step thrust profiles.

Figure 4.6 shows the response of the system due to a step input with damping. Figure 4.6(a) shows that the undesirable chaotic motion occurs with small damping but higher damping actually does help the system achieve gravity gradient (Figure 4.6(b)). As is summarized in Table 4.10 only the higher damping cases with $C = 8$ and $C = 10$ achieve gravity gradient. This is very different from the step responses without damping which always perform poorly.

Figure 4.7 shows results from the various damping coefficients given in Table 4.3 while using the Posicast thrust profile. The Posicast does perform well with damping achieving a tumbling motion that begins to transition to gravity gradient. As expected, an input shaped thrust profile produces good results however they do not appear appreciably different than those seen for the Posicast results from the L_0 and E studies with similar elasticity or length (Figure 4.3 and Figure 4.5).

Figure 4.8 is shown to demonstrate the change in energy of the system, after the thrust maneuver has been completed, due to damping. This also shows the rotation rates of the end bodies, which behave similarly to the other Posicast rotation rates.

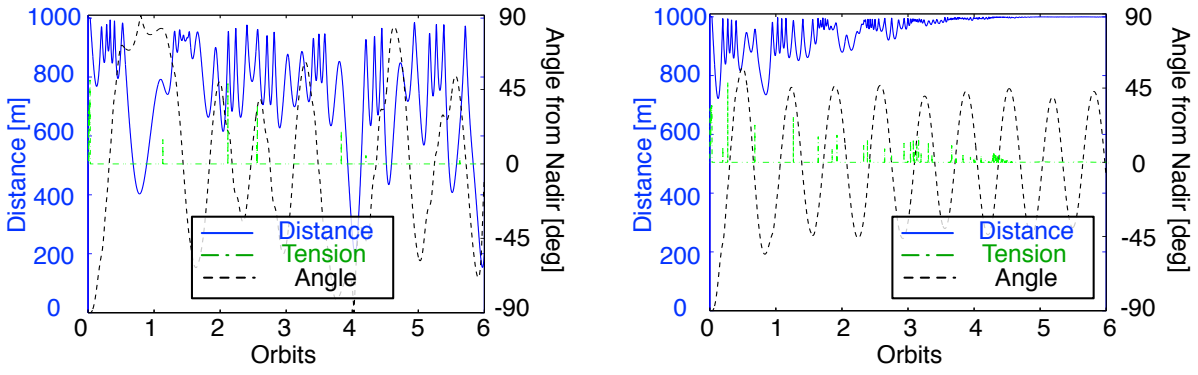

(a) $C = 0.1 \frac{kg}{s}$ (b) $C = 8 \frac{kg}{s}$

Figure 4.6: Relative motion and tether tension between tug and debris with a *step* input. $L_0 = 1$ km, $E = 170$ GPa and $C = 8 \frac{kg}{s}$. The debris' expected mass is 1500 kg but it is actually 2000 kg in simulation. Tension scaled by 27.78. Damping study.

It turns out that input shaping works against damping. Because input shaping is designed to reduce relative motion, and therefore stress in the tether, there is less damping. As damping successfully reduces motion between the end bodies, the tether eventually reaches its unstretched length and tension reaches nearly zero. This eventually causes the formation to behave similarly to a rigid bar, oscillating in orbit without further reduction in motion.

Table 4.9 shows that the average end body rotation rates stay fairly small and within the ranges seen by the previous Posicast simulations. In fact, no overly large rotation rates are experienced showing some of the benefits of the damping present. Similarly, for the step input with high damping ($C = 8$ and $C = 10$), the end body rotation rates are fairly small. Lower damping sees much higher rotation rates (and non-tumbling/gravity gradient motion). But the cases where the step input achieves gravity gradient, small rotation motion also occurs.

Again, it is challenging to produce better metrics than some of these qualitative observations because the system is not only influenced by post-thrust conditions, but also when tensioning occurs. Tension and relative motion of the bodies along with angle from nadir can alter the motion of the system significantly, as seen in all of these studies. Still, it is informative to see that tumbling and gravity gradient motion is a common behavior, aiding collision avoidance.

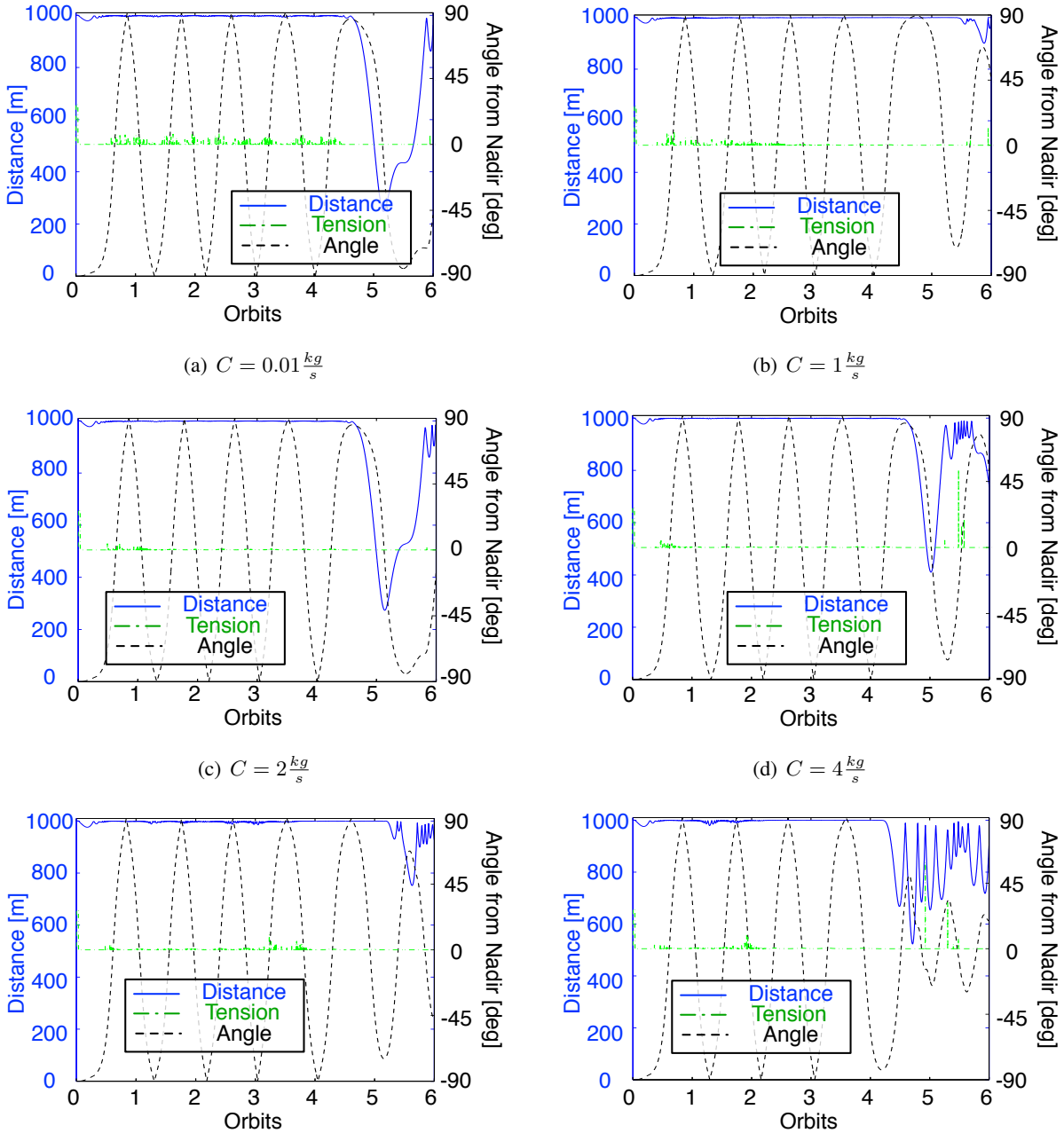

(a) $C = 0.01 \frac{kg}{s}$

(b) $C = 1 \frac{kg}{s}$

(c) $C = 2 \frac{kg}{s}$

(d) $C = 4 \frac{kg}{s}$

(e) $C = 8 \frac{kg}{s}$

(f) $C = 10 \frac{kg}{s}$

Figure 4.7: Relative motion and tether tension between tug and debris with a *Posicast* input. $L_0 = 1$ km, $E = 170$ GPa. The debris' expected mass is 1500 kg but it is actually 2000 kg in simulation. Tension scaled by 27.78. Damping study.

Table 4.8: End body rotation rate average and standard deviation for the *Posicast* profile C study. $L_0 = 1000$ m, $E = 170$ GPa

C (m)	Body	Mean $\omega_{B/I}$ (deg/s)	Standard Deviation $\omega_{B/I}$ (deg/s)
0.1	Tug	0.604	0.601
	Debris	1.002	0.883
1	Tug	1.140	1.133
	Debris	0.643	0.680
2	Tug	0.384	0.772
	Debris	0.614	0.634
4	Tug	0.698	1.004
	Debris	1.426	3.060
8	Tug	1.234	3.235
	Debris	1.297	1.579
10	Tug	2.718	5.315
	Debris	3.022	4.803

Table 4.9: End body rotation rate average and standard deviation for the *step* profile C study. $L_0 = 1000$ m, $E = 170$ GPa

C (m)	Body	Mean $\omega_{B/I}$ (deg/s)	Standard Deviation $\omega_{B/I}$ (deg/s)
0.1	Tug	13.206	9.176
	Debris	6.687	5.361
1	Tug	15.337	12.088
	Debris	12.309	7.082
2	Tug	11.934	6.905
	Debris	12.451	6.186
4	Tug	7.384	5.172
	Debris	7.098	4.005
8	Tug	4.401	5.051
	Debris	3.222	3.616
10	Tug	2.583	2.900
	Debris	2.166	2.490

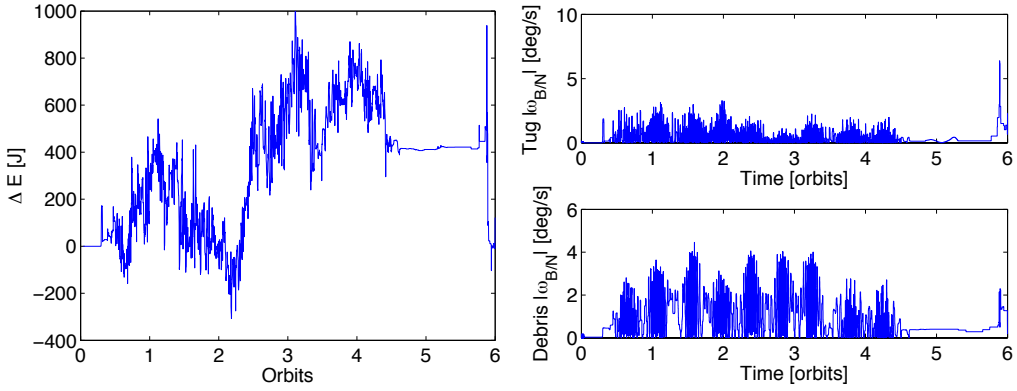

(a) Change in energy

(b) End body rotation rates

Figure 4.8: Example system properties of $C = 0.1\frac{kg}{s}$ for the Posicast control

The summary of the results from the damping study is given in Table 4.10. Generally, larger damping ratios are required for the step input to not require input shaping. All input shaped trials tumble and begin to transition to gravity gradient motion, an ideal scenario.

Table 4.10: Summary of tether damping, C, study. $E = 170$ GPa, $L_0 = 1$ km

C ($\frac{kg}{s}$)	Thrust Profile	Gravity Gradient/Tumble	Notes
0.1	Step	No	End body motion w/o oscillation
0.1	Posicast	Tumble to Possible Grav. Gradient	Transitions before 5 orbits
1	Step	No	Close approach of ≈45 m
1	Posicast	Tumble to Possible Grav. Gradient	Transitions at about 5 orbits
2	Step	No	End body motion but constant oscillation occurs
2	Posicast	Tumble to Possible Grav. Gradient	Transitions before 5 orbits
4	Step	No	End body motion but constant oscillation occurs
4	Posicast	Tumble to Possible Grav. Gradient	Transitions before 5 orbits
8	Step	Yes	
8	Posicast	Tumble to Possible Grav. Gradient	Transitions at about 5 orbits
10	Step	Yes	
10	Posicast	Tumble to Possible Grav. Gradient	Transitions at about 4 orbits

4.6 Stiffness and Damping Study

Due to the promising results of damping with a step input, both Young's modulus and damping are explored together. Note, the tether length is kept constant at $L_0 = 1$ km, because this consistency seems to produce desirable behavior. There are two avenues used to explore the stiffness and damping trade space. First, the system is linearized and E and C are computed to see if it is possible to damp both the longitudinal

motion and the in-plane rotation (gravity gradient oscillations). Then, E and C are swept to determine the behavior of the system over a wide range of applicable values.

4.6.1 Linearized 'Gain' Study

It is desirable to have an idea of the required combination of Young's modulus and damping to properly reduce the motion between the end bodies, while damping the in-plane rotations. Keeping the formation completely aligned gravity gradient along the radial direction is ideal. However, the use of large moduli generally means the system does not flex much and damping is small. The formation quickly settles into behavior similar to a rigid bar, thus inducing gravity gradient oscillations.

In order to get a high-level idea of the Young's modulus and damping coefficient needed to damp *both* in-plane oscillations and tether stretching, the developments of Natarajan and Schaub are followed.[54] Young's modulus and damping are treated like gains and computed to find the lower-bounds on these values. The analysis makes several large assumptions: first is that the tethered-tug motion is in a circular orbit and second is that there are small in-plane oscillations. Of course, after the thrusting maneuver the orbit is no longer circular ($e \approx 0.02$) and the tether often oscillates in the 30^o - 80^o range. Still, the computed Young's modulus and damping should bound these parameters for the system.

Figure 4.9 shows the basic definition of the orbit frame ($\hat{\boldsymbol{o}}$) and the tether frame ($\hat{\boldsymbol{t}}$) aligned along the tether longitudinal axis. The rotation from the orbit frame into this frame is defined by a 3-axis rotation

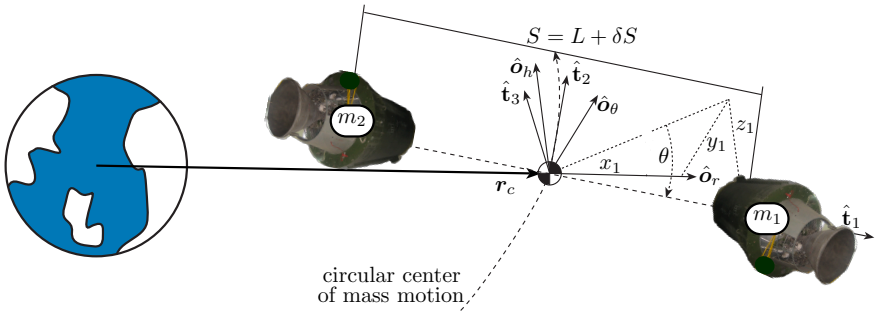

Figure 4.9: Orbit and tether frame definitions using Euler Angles

about the out-of-plane axis ($\hat{o}_h$). The rotation about the longitudinal axis does not affect the dynamics,

to first order. The out-of-plane motion decouples from the in-plane motion, as shown by Reference 54, and is not considered here. Using a massless tether with the tug and debris end bodies, the position of m_1 in the tether frame is represented as $\boldsymbol{\rho}_1 = \left[\frac{m_2}{m_1+m_2}S, 0, 0\right]$ with respect to the center of mass. ($S = \sqrt{\Delta x^2 + \Delta y^2 + \Delta z^2}$, the distance norm.) Therefore, the rotation from the tether frame to the orbit frame is given by Eq. (4.6).

$$\begin{bmatrix} x \\ y \\ z \end{bmatrix} = \begin{bmatrix} \cos(\theta) & \sin(\theta) & 0 \\ -\sin(\theta) & \cos(\theta) & 0 \\ 0 & 0 & 1 \end{bmatrix} \begin{bmatrix} \frac{m_2}{m_1+m_2}S \\ 0 \\ 0 \end{bmatrix} \tag{4.6}$$

Linearizing about small angles and taking derivatives of Eq. (4.6) gives

$$\begin{bmatrix} x \\ y \\ z \end{bmatrix} \approx \frac{m_2}{m_1+m_2} \begin{bmatrix} S \\ S\theta \\ 0 \end{bmatrix} \tag{4.7}$$

$$\begin{bmatrix} \dot{x} \\ \dot{y} \\ \dot{z} \end{bmatrix} \approx \frac{m_2}{m_1+m_2} \begin{bmatrix} \dot{S} \\ \dot{S}\theta + S\dot{\theta} \\ 0 \end{bmatrix} \tag{4.8}$$

From the center of mass, the following relative position vector description must be true:

$$m_1\boldsymbol{\rho}_1 + m_2\boldsymbol{\rho}_2 = 0 \tag{4.9}$$

Taking the center of mass constraint into account, S^2 can be written as:

$$S^2 = \frac{(m_1+m_2)^2}{m_1^2}\left(x_1^2 + y_1^2 + z_1^2\right) \tag{4.10}$$

Taking two derivatives of Eq. (4.10), substituting in the Clohessy-Wiltshire-Hill[17,27] equations, and using Eq. (4.9) to get everything in terms of the position of body 1, the tug, produces:

$$2\dot{S}^2 + 2S\ddot{S} = \frac{2(m_1+m_2)^2}{m_1^2}\left(\dot{x}^2 - 2ny\dot{x} + \dot{y}^2 + 3n^2x^2 + 2nx\dot{y} + \dot{z}^2 - n^2z^2\right) \tag{4.11}$$

Here n is the mean motion of the approximated circular orbit. Eq. (4.7) and Eq. (4.8) are then used to rotate the expression into the spherical tether frame. Eq. (4.11) can be solved for the acceleration of the tether

expansion, $\ddot{S}$. The equation can then be focused on the variation of the tether expansion:

$$S = L_0 + \delta S \tag{4.12}$$

where L_0 is, as before, the unstretched tether length. Plugging Eq. (4.12) into Eq (4.10), linearizing, and then removing higher order terms gives:

$$\delta\ddot{S} = -\frac{1}{L_0 m_1^2 m_2}\left(Cm_1(m_1+m_2)\delta\dot{S} + L_0(K_S m_1(m_1+m_2) - 3m_2^3 n^2)\delta S - 2L_0^2 m_2^3 n\dot{\theta}\right) \tag{4.13}$$

The in-plane rotation is derived by Reference 54 and given here for ease of reference.

$$\ddot{\theta} = -\frac{2n}{L_0}\delta\dot{S} - 3n^2\theta \tag{4.14}$$

The linearized natural frequency of the in-plane oscillations from Eq. (4.14) is $\Omega = \sqrt{3n^2}$. For an 800 km circular orbit, this turns into about 3494 s or one cycle per 0.577 orbits. This period is reasonably consistent with the oscillation rates seen in the other simulations with smaller angle gravity gradient behavior.

In Eq. (4.13), $K_S = \frac{EA}{L_0}$ and C are considered control parameters, essentially like gains. For stability of Eq. (4.13), the natural frequency of this system must be greater than zero and the damping terms must also be greater than, or equal to zero:

$$\frac{K_S m_1(m_1+m_2) - 3m_2^3 n^2}{m_1^2 m_2} > 0 \tag{4.15}$$

$$\frac{C(m_1+m_2)}{L_0 m_1 m_2} \geq 0 \tag{4.16}$$

To allow for the separation distance to damp the in-plane rotations, Eq. (4.15) is solved for E such that this frequency is the same as the in-plane frequency ($\Omega = \sqrt{3n^2}$) resulting in:

$$E = \frac{3L_0 m_2(m_1^2+m_2^2)n^2}{Am_1(m_1+m_2)} \tag{4.17}$$

Eq. (4.16) is then solved for C, using Eq. (4.17) while being equated to the general expression for damping, $2\zeta\Omega$.

$$C = \frac{2\zeta L_0 m_1 m_2\sqrt{\frac{AEm_1^2 + AEm_1m_2 - 3L_0m_2^3n^2}{L_0m_1^2m_2}}}{m_1+m_2} \tag{4.18}$$

Using the values from Table 2.1 for area, end body masses, and a mean orbit altitude of 610 km (mean of 800 km $\times$ 420 km) to get the mean motion n, the elasticity is $E = 555,545$ Pa and the damping is $C = 3,509.95\ \frac{kg}{s}$, when critically damped at $\zeta = 1$. This modulus is much lower than what is generally considered for space tethers. A modulus of $E \approx 0.5$ MPa can be found with some types of rubber, which have considerably lower yield stresses than Kevlar. The damping is much greater than anything studied so far and is not likely possible with existing materials, especially in combination with such a low modulus. Since the value of C varies linearly with ζ, critical damping is not required. However, ζ would need to be in the range of 1×10^{-3} to be within the previously determined damping coefficient range of Table 4.3. Making ζ this small also ensures that the system is under damped and will oscillate for a significant period of time making the orbital motion, end body spin rates, etc. much more important factors, likely reducing the effectiveness of damping. Therefore, material properties alone are not likely to get the formation to achieve a stationary gravity gradient orientation.

Reference 45 also found that properly damping longitudinal modes requires the tether to have a very low stiffness. Not only are these tether properties unachievable by current materials, but highly elastic materials behave poorly with the input shaping filters. The system's natural frequency becomes very low making thrust durations last over many orbits with thrust magnitudes that are on the order of tens of Newtons. This violates the high-thrust premise of the tethered-tug system. Further, significant portions of the Δv and remaining rocket fuel are used stretching the tether, not lowering the periapsis, reducing the overall effectiveness of such extreme tether properties.

It therefore becomes important to consider how the more realistic tether properties behave over a range of elasticity and damping.

4.6.2 Stiffness and Damping Sweeps

Transitioning back to realistic modulus and damping values in Table 4.2 and Table 4.3, Table 4.11 summarizes the behavior of the tethered-tug system as E and C vary. The table shows whether there is a collision, tumbling motion, highly dynamic motion (Figure 4.6(a)), or gravity gradient motion. If there is a close approach, the minimum separation distance is given next to the behavior seen.

This study demonstrates some very encouraging results. A step input thrust profile often causes collisions and does not achieve a tumbling or gravity gradient orientation. The results in Table 4.11 show that with damping, this is not true. With higher damping coefficients, and without input shaping, the step input achieves desirable nadir oscillations. For $C = 4$, it appears that gravity gradient motion is induced, but the end body separation distance does vary somewhat for multiple orbits. It is likely that this damps to gravity gradient. It also appears that elasticity is not a driving factor in the performance of the system. In the end, if damping is at or above $4\ \frac{kg}{s}$ the system likely achieves a taut, gravity gradient behavior.

Table 4.11: Summary of tether stiffness E and damping C study using a *step* input. $L_0 = 1$ km

$C\ \frac{kg}{s}$	$E = 27$ GPa	60.5 GPa	94 GPa	161 GPa	194.5 GPa	228 GPa
0.1	Collision	Dynamic	Dynamic	Dynamic	Dynamic	Dynamic
1	Dynamic, ≈ 26 m	Dynamic	Dynamic	Dynamic, ≈ 30 m	Dynamic	Dynamic
2	Dynamic, ≈ 35 m	Dynamic	Dynamic	Dynamic	Dynamic	Dynamic
4	Grav. Grad?	Grav. Grad?	Grav. Grad?	Grav. Grad?	Grav. Grad?	Grav. Grad?
8	**Grav. Grad**	**Grav. Grad**	**Grav. Grad**	**Grav. Grad**	**Grav. Grad**	**Grav. Grad**
10	**Grav. Grad**	**Grav. Grad**	**Grav. Grad**	**Grav. Grad**	**Grav. Grad**	**Grav. Grad**

4.7 Conclusions

Changing the tether properties can have significant effects on the tethered-tug system in orbit. Various lengths change the system's response to a Posicast thrust profile from drifting, to tumbling, and highly dynamic motion. Longer tether lengths seem to reduce the effectiveness of input shaping. Intermediate and short lengths appear better suited for this system.

Elasticity appears to not have a discernible effect on the behavior of the system. By itself, and with damping, the elasticity did not greatly alter the performance by comparison to changes in C and L_0.

Damping, however, can create drastic changes in the system. Higher damping coefficients can replace the use of input shaping and allow a step input to achieve gravity gradient oscillations. While it does not alter the Posicast behavior significantly, it does make the overall motion and end body spin rates more benign.

Chapter 5

Slack Tethers and Rotational Debris Motion

Chapters 3 and 4 assumed that rotational motion was not induced, effectively making the end masses behave somewhat like point masses while thrusting (even though rotation is allowed). Further, the tether is always assumed to be taut when starting the thrusting maneuver. This chapter considers the effects of the tether being slack before the thrusting maneuver. It also considers how a tether attached to the debris, offset from the debris center of mass, affects the system. Preexisting rotational motion of the debris is also briefly explored. This chapter seeks to describe how the tethered-tug system behaves with less than ideal initial conditions.

5.1 Slack Tethers

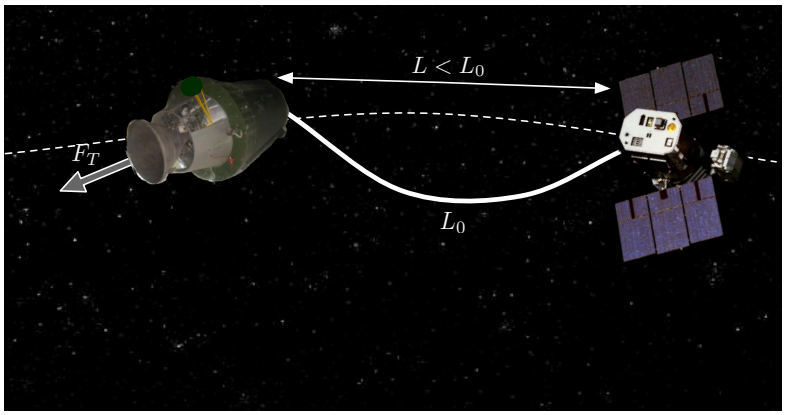

Figure 5.1: Illustration of a slack tether, just prior to thrusting, with a taut length of L_0

5.1.1 Effects of a slack tether

Having a slack tether prior to thrusting (Figure 5.1) can drastically change performance of the system. All previous simulations presented in this paper have assumed that both objects are initially separated by the tether length of L_0. That is, the tether is virtually taut when the thrust starts. Conversely, Figure 5.2 shows how a slack tether amplifies the dynamic response of the system while removing all effects of input shaping. A collision occurs near 400 seconds and the tether force jumps to nearly 27,000 N, not 800 N seen in Figure 3.13(b). This is likely enough to cause the tether to yield and the quick on-set of the force has a large potential to break the connection to the debris (i.e. the harpoon, net, etc.).

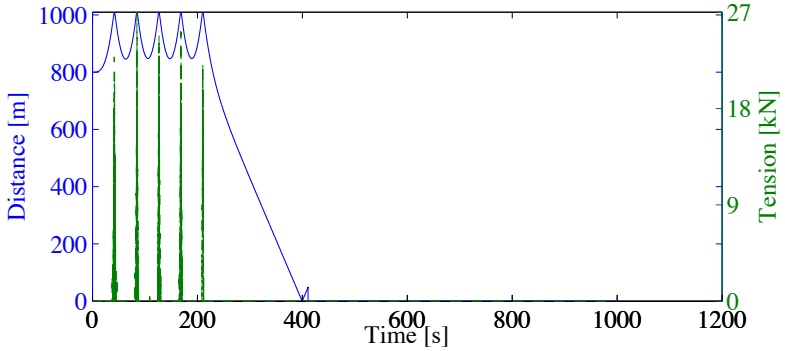

Figure 5.2: Slack tether: 1000 m tether with 200 m of slack. Simulated in deep space with a double notch ($.14 \leq \omega_c \leq .22$ Hz), assuming a debris mass of 2000 kg (actual 1500 kg), 2009 N thrust, 2 discrete tether masses. Deep space

This poor behavior is caused by the fact that the majority of the input shaped thrust profile occurs during the time it takes to remove the slack in the tether and pull it taut. The tether is not effected by desired input shaping profiles. Instead, the tether experiences a large step increase all while the tug is increasing in velocity. This causes the substantial 'whipping' effect seen in Figure 5.2.

A brief sensitivity study is performed to examine the effect of how much slack can be present in the tether without severely altering performance of the input shaping methods. An alternative to the slack tether, a tensioned tether, is also explored.

5.1.2 Input Shaping Methods' Sensitivity to a Slack Tether

5.1.2.1 Deep Space Study

The system is placed in deep space and the three primary input shaping methods are compared for ability to perform with slack in the tether. The distance between the end bodies is taken from $L_0 = 1$ km and reduced by 'X' meters. All bodies start equally spaced.

Table 5.1 shows the results for each input shaping method. The maximum slack distance is determined by the slack possible without the end bodies colliding within 1500 s. If a different simulation duration were used, the maximum slack distance would change. Any larger slack distance causes a collision within 1500 s. While this metric is somewhat arbitrary, the major take-away is that all methods experience collisions fairly quickly. The double notch filter performs the best, being most robust to slack in the tether, however it can only handle 25 m of slack out of 1000 m. The Posicast and Bang-off-bang profiles are highly sensitive to a slack tether and essentially must start with a taut system. This study again demonstrates how amplified the motion between the end bodies becomes with a slack tether.

Table 5.1: Maximum slack possible in tether for a given shaping method. Deep space. $L_0 = 1$ km, the debris mass is 2000 kg (1500 kg expected). Simulation duration of 1500 s.

Input Shape Method	Slack In Tether (m)	Travel Dist. After 1500 s (m)	Max. Tension (N)
Double Notch	25	303	7584
Robust Posicast	2	406	2337
Bang-off-bang	0	105	873

5.1.2.2 On-orbit Study

Because the behavior of the system changes quite significantly while on-orbit, it is important to consider how a slack tether affects this motion. Table 5.2 shows the general behavior of the system using the slack results from the deep space study in Table 5.1 as a baseline.

With the same slack in the tether as the deep space results, the input shaping methods fail to produce gravity gradient or tumbling motion of the system. Because the slack distance is so small for the Posicast and bang-off-bang profiles, it can be concluded that neither are capable of withstanding any slack in the tether.

Table 5.2: Maximum slack possible in tether for a given shaping method. On-orbit. $L_0 = 1$ km, the debris mass is 2000 kg (1500 kg expected). Simulation duration of 6 orbits.

Input Shape Method	Slack In Tether (m)	Minimum Separation (m)	Average, both bodies ω_{body} (deg/s)	Gravity Gradient?
Double Notch	5	943	$\approx$2.05 $\pm$1.7	Yes
Double Notch	25	642	$\approx$7.70 $\pm$4.6	No - large change in distance
Robust Posicast	2	621	$\approx$5.45 $\pm$4.5	No - large change in distance
Bang-off-bang	2	603	$\approx$9.90 $\pm$4.8	No - large change in distance

However, the notch can achieve gravity gradient and small rotation rates with very small slack distances of less than 10 m.

Figure 5.3 demonstrates the motion experienced by all of the input shaping methods when the slack distance has become too large for the controller. Overall, the tethered-tug system oscillates about gravity gradient but has a lot of end body motion, with periods of slack and tension. This is not ideal, however the distances do stay fairly large making this a decent response.

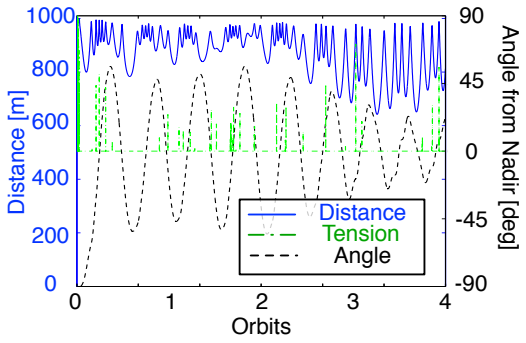

Figure 5.3: Motion of system using a notch and 25 m of slack

In the end, the system is not tolerant to an initially slack tether. The best way to combat this is to allow for the orbital motion to tension the tether passively and then apply thrust. The question then arises: how tolerant is the system to tension in the tether prior to input shaping? This behavior is explored next.

5.1.3 Input Shaping Methods' Sensitivity to a Tensioned Tether

5.1.3.1 Deep Space Study

The system is placed back in deep space and the input shaping methods are again compared for the ability to perform with tension in the tether. The starting positions of the bodies are stretched just enough to achieve the desired tensions in the tether. These stretch distances are less than a meter. All bodies start equally spaced.

Table 5.3 shows that the system is much more robust to pre-tension in the tether than slack. With tens to a few hundred Newtons of tension force, all input shaping methods perform relatively well. This is highly encouraging because ensuring the tether is taut appears like a requirement for the system, to avoid any slack behavior. Tether tension could also potentially be detected fairly easily by the system, allowing for a metric to determine when the thruster should actuate.

Table 5.3: Response of various pre-existing tensions in tether for a given shaping method. Deep space. $L_0 = 1$ km, the debris mass is 2000 kg (1500 kg expected). Simulation duration of 1500 s.

Input Shape Method	Tension in Tether (N)	Travel Dist. After 1500 s (m)	Max. Tension (N)
Double Notch	10	8	801
	100	14	870
	250	106	1475
	500	284	2295
	800	458	3572
	1000	637	4256
Robust Posicast	10	19	774
	100	34	880
	250	304	1177
	500	832	1838
	800	Collision at 1369 s	2795
	1000	Collision at 1216 s	3280
Bang-off-bang	10	110	895
	100	174	949
	250	299	1047
	500	535	1294
	800	113	1705
	1000	467	2039

When the force is relatively low in the tether, the Posicast and notch filters behave very well and do not see much degraded performance. Once tensions get higher, however, the notch and the bang-off-bang profiles appear more robust. It should be noted that once the pre-existing tension in the tether reaches about the same size as the tension created by the thrust, all forms of input shaping appear to stop working. Pre-

existing forces of about 500 N or larger negate most of the positive benefits of the input shaping methods, therefore any shaping should occur before this force is reached.

5.1.3.2 On-orbit Study

Based upon the results from the deep space study, pre-tensions of 100 N and 250 N are used to explore the performance of the input shaping methods on-orbit. These forces are used because they produced reasonably good results in deep space and should on-orbit as well. Table 5.4 shows that the system generally continues to respond well to a pre-tensioned tether. As with deep space, a tension of 100 N still produces good motion for the system and actually initiates the notch to achieve a tumble/gravity gradient motion, which is not caused from a direct notch implementation. The Posicast system also falls into a tumble/gravity gradient motion and both methods have small residual end body rotation rates.

With 250 N of pre-tension, the notch continues to perform very well. The Posicast unfortunately does not tumble or get into a gravity gradient oscillation. Similarly, the bang-off-bang profile does not perform as well with pre-tension, however this is expected from the deep space results since the bang-off-bang never had great performance. Still, the separation distance remains relatively large for both Posicast and bang-off-bang profiles. Their formations end up oscillating about nadir but the end bodies simply do not settle to the full tether length. The end body rotation rates are also larger than the 100 N pre-tension results.

Table 5.4: Response of various existing tensions in tether for a given shaping method. On-orbit. $L_0 = 1$ km, the debris mass is 2000 kg (1500 kg expected). Simulation duration of 6 orbits.

Input Shape Method	Tension in Tether (N)	Minimum Separation (m)	Average, both bodies ω_{body} (deg/s)	Gravity Gradient?
Double Notch	100	525	$\approx$2.3 $\pm$3.9	Tumble-to-gravity gradient
	250	141	$\approx$1.1 $\pm$.94	Tumble-to-gravity gradient
Robust Posicast	100	217	$\approx$.87 $\pm$.71	Tumble-to-gravity gradient
	250	617	$\approx$5.1 $\pm$3.6	No - large change in distance
Bang-off-bang	100	627	$\approx$6.2 $\pm$4.6	No - large change in distance
	250	652	$\approx$7.7 $\pm$6.0	No - large change in distance

This generally shows that a slack tether prior to thrusting is not acceptable. Small to moderate pre-tension generally allows for much better performance and the notch and Posicast are more robust to this change in the system.

5.2 Rotational Motion

5.2.1 Challenges of Towing Rotating Debris

It can be easily imagined that many of the debris capture concepts do not guarantee that the tether attachment location will be aligned with the center of mass (CM). The net and harpoon capture methods are likely to create off-axis forces. Many mechanical grapples may also attach to the most structurally sound component that is not necessarily in line with the CM.

In this study debris attachment point will be varied from the CM around the body, but the tether will remain aligned with the tug's CM. The attachment will be placed at an angle about the body's radial, or 'pitch', axis. The rotation rates induced by variable offsets angles are characterized in both deep space and on-orbit simulations. 'Yaw' axis rotation (Figure 5.4(b)) is not directly considered however the analysis and results are similar.

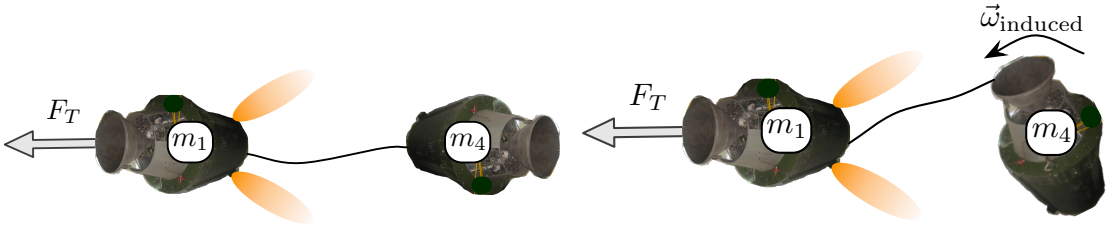

(a) In-line tether attachment (b) Off-axis tether attachment

Figure 5.4: Tether attachment locations on debris

Further, some debris have been found to tumble at rates of just a few degrees per second[68] in orbit which is reasonably small, improving the viability of attaching a tether. Asteroids also tumble or spin. Removing existing motion of the target mass might be difficult, however, because a single axis tether force cannot always reduce a three axis tumble. The tether must be attached intelligently so that it is relatively far from the (moving) spin axis of the object. This will allow the tether to properly apply torque to the object to remove the spin. Achieving an ideal tether attachment location to reduce the tumble rate of the debris is not directly considered because it includes many aspects of the capture system that are beyond the scope of the control methods explored here. However, the debris is given an initial tumble rate and the control's ability

to reduce that motion is briefly discussed, assuming a tether attachment that is in-line with the CM.

5.2.2 Offset Tether Attachment to Debris

An offset tether attachment will cause rotation of the debris once thrust is applied and the tether begins to tension. To avoid this, it is useful to find the natural rotation rate of the debris, given an offset attachment, and apply input shaping to remove that mode from the system.

Figure 5.5 demonstrates a simplified attachment model so that the natural rotation rate can be found. This model only considers $\pm 90^o$ in rotation angle ϕ due to the fact descriptions become non-unique for larger angles. Also, the simulation does not account for wrapping of the tether around bodies, again reducing the angle to $\pm 90^o$.

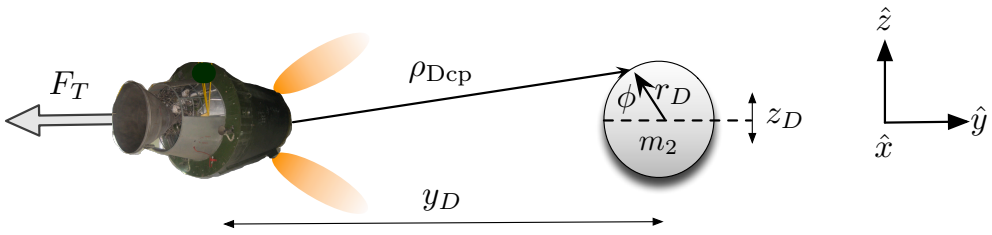

Figure 5.5: Tether attachment model inducing rotation about 'pitch' axis (about the minor axis of the cylinder)

Using the geometry set-up in Figure 5.5, a model of the debris' pitching rotation can be created. Euler's rigid body equations of motion, $\dot{\boldsymbol{H}} = \boldsymbol{\tau}$, are used. Because the cylinder is rotating in a pure spin about a principal axis the derivative of the angular momentum, $\boldsymbol{H}$ simply becomes:

$$\dot{\boldsymbol{H}} = \begin{bmatrix} I_{11}\dot{\omega} \\ 0 \\ 0 \end{bmatrix} \tag{5.1}$$

where ω here is the rotation rate of the debris and I_{11} is the body's minor axis inertia. The torque can then be defined as:

$$\boldsymbol{\tau} = \boldsymbol{r} \times \boldsymbol{F_S} \tag{5.2}$$

where $\boldsymbol{r}$ is the radius vector of the cylinder and $\boldsymbol{F_S}$ is the tether tension force. Rotating the tether radius into

the local tethered-tug frame (which is an inertial frame in deep space and the orbit/LVLH frame in orbit) can be expressed as:

$$\boldsymbol{r} = \begin{bmatrix} -r_D \cos(\phi) \\ 0 \\ r_D \sin(\phi) \end{bmatrix} \tag{5.3}$$

Simplifying the system so that tension in the tether is only related to the position of the debris:

$$\boldsymbol{\rho}_D = \begin{bmatrix} 0 \\ y_D \\ z_D \end{bmatrix} \tag{5.4}$$

and the vector to the tether connection point:

$$\boldsymbol{\rho}_{Dcp} = \boldsymbol{\rho}_D + \boldsymbol{r} \tag{5.5}$$

For this model, there is no x-axis contribution because it does not change the rotational motion in the pitch axis. Using Eq. (2.3) for the direction of the tether force the tether unit vector is written as:

$$\hat{\boldsymbol{e}} = \frac{\boldsymbol{\rho}_{Dcp} - \boldsymbol{\rho}_{Tcp}}{|\boldsymbol{\rho}_{Dcp} - \boldsymbol{\rho}_{Tcp}|} = \frac{\boldsymbol{\rho}_{Dcp}}{|\boldsymbol{\rho}_{Dcp}|} \tag{5.6}$$

Here, $\boldsymbol{\rho}_{Tcp}$ is the connection point to the tug, which is defined as the 'zero' position. The tether force can then be defined as:

$$\boldsymbol{F_S} = K_S(|\boldsymbol{\rho}_{Dcp}| - L_0)\hat{\boldsymbol{e}} = K_S(|\boldsymbol{\rho}_{Dcp}| - L_0)\frac{\boldsymbol{\rho}_{Dcp}}{|\boldsymbol{\rho}_{Dcp}|} \tag{5.7}$$

Crossing Eq. (5.7) and Eq. (5.3), solving for the angular acceleration $\ddot{\phi}$, and linearizing with respect to ϕ, a rotational natural frequency can be found. It should be noted that the z-position is nominally zero and the y-position is set to the average separation distance given a thrust, or $y_D = \frac{F_T}{2K_S} + L_0$. This means that the frequency is not only a function of the tether properties, the tether length, the size and inertia of the debris, but also the amount of thrust used. This makes sense as the tension in the tether is directly related to the thrust force applied and a higher thrust should provide a "stiffer" tensioning force. The debris' rotational natural frequency is:

$$\omega_{n\,\text{Rot}} = \sqrt{\frac{-K_S L_0 r_D y_D + \frac{K_S r_D^2 z_D^2}{\sqrt{r_D^2 - 2r_D y_D + y_D^2 + z_D^2}} + K_S r_D y_D \sqrt{r_D^2 - 2r_D y_D + y_D^2 + z_D^2}}{I_{11}\sqrt{r_D^2 - 2r_D y_D + y_D^2 + z_D^2} - \frac{r_D z_D(-K_S L_0 r_D z_D + K_S r_D z_D \sqrt{r_D^2 - 2r_D y_D + y_D^2 + z_D^2}}{I_{11}(r_D^2 - 2r_D y_D + y_D^2 + z_D^2)^{3/2}}}} \tag{5.8}$$

Evaluating Eq. (5.8) given the properties in Table 2.1, $z_D = 0$, $y_D = \frac{F_T}{2K_S} + L_0$, the rotational frequency of the system is 0.123 Hz. A similar analysis can be performed for a major axis spin of the debris but this is not analyzed here.

Figure 5.6 shows how the natural frequency in Eq. (5.8) changes as the thrust force is varied from zero to 2000 N. The frequency changes by about 0.07 Hz over this thrust range. As was shown in Chapter 3.3.3 a change of even 0.03 Hz has noticeable effects on the behavior of the system. Also, the continuous notch and Posicast input shape methods utilize variable thrust levels, meaning that the frequency will change *because* of the control.

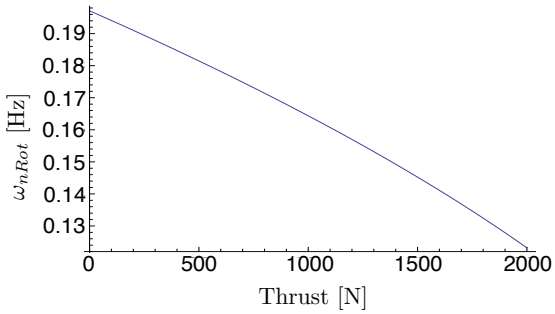

Figure 5.6: Approximate frequency response as thrust varies

Because all thrust profiles baseline 2000 N as the maximum thrust, the frequency predicted at this level (0.123 Hz) is assumed to be the frequency to remove from the thrust profile. All thrust methods assume that the debris mass knowledge is perfect in the following discussion. The double notch control is modified to place one notch at 0.19 Hz for the tether, and the other is placed at 0.123 Hz for the rotational motion. The Posicast filter is unaltered in this discussion due to the fact that the residual vibration in the system for this frequency is still less than 1% (Figure 3.32). The robust Posicast already utilizes 5 thrust levels and adding another frequency to the control would add more delays, something that is undesirable, especially if this control can handle such a wide range of frequency changes. (If the Posicast control was not robust, this rotational frequency should definitely be added to the system to ensure this mode is not overly excited.) The next sections consider the various control strategies in deep space and on-orbit using the frequency found in Eq. (5.8).

5.2.2.1 Deep Space Study

First, the rotation induced by variable tether offset angles is considered in deep space. Figure 5.7(a) shows the rotation frequency of the debris given an initial attachment offset of 10 degrees. The rotation rate is about 0.1338 Hz, which is reasonably close to the 0.123 Hz computed from Eq. (5.8). It is interesting to see that this frequency is relatively unchanged by the tether attachment angle, as shown in Figure 5.7(b). The frequency falls between 0.12 Hz and 0.14 Hz consistently. This is encouraging because it should help to make the input shaping profiles more effective, independent of the oscillation amplitude of the debris.

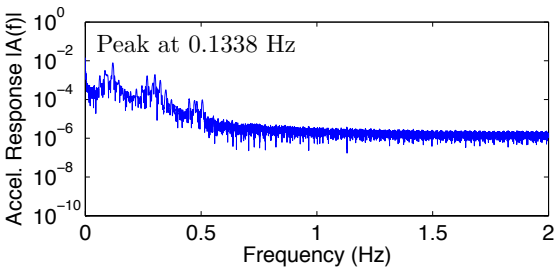

(a) Frequency response of a step input with $\phi_0 = 10^o$

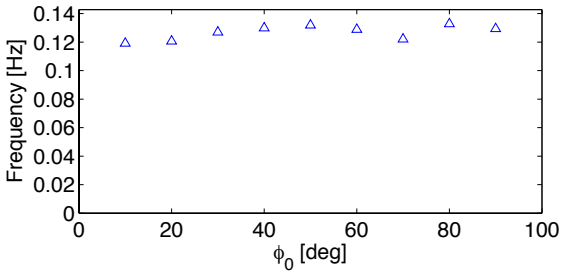

(b) Frequency response of a step input given various initial tether offsets, ϕ_0

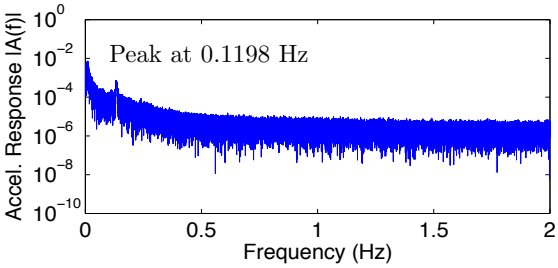

(c) Frequency response of robust Posicast input shaping with $\phi_0 = 10^o$

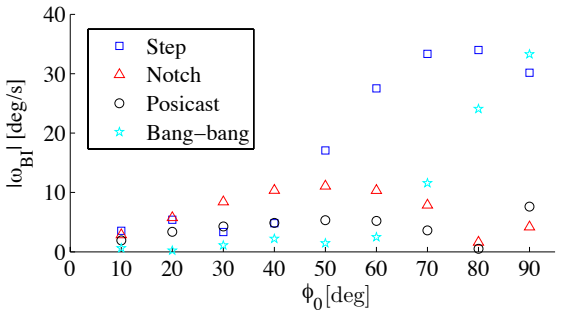

(d) Rotation rate at the end of thrust for various thrust methods

Figure 5.7: Deep space performance of system with various tether attachment offsets about debris minor inertia axis

Figure 5.7(c) shows the frequency response of the debris with a Posicast control applied. One exciting result is that the primary frequency peak is attenuated, when compared to the step input frequency response in Figure 5.7(a), demonstrating that the rotation rate should be minimized. It is also interesting to see the frequency peak shift slightly, as predicted since the frequency depends upon thrust amplitude. Similar results are witnessed for the notch and bang-off-bang profiles.

Figure 5.7(d) shows the post-thrust rotation rate of the debris, given an initial tether angle. All thrust profiles perform decently with small angles but larger angles cause issues for the step and bang-off-bang profiles. The notch and Posicast profiles experience an arcing behavior with a peak in rotation rate at about $\phi_0 = 50^o$. Thrusting in general does cause spinning but not as large as maybe originally expected.

Input shaping does seem to help reduce the final rotation rate of the debris, as shown in Figure 5.8. The Posicast control performs best over the range of possible angles but is beaten sometimes especially by the the bang-off-bang at smaller angles.

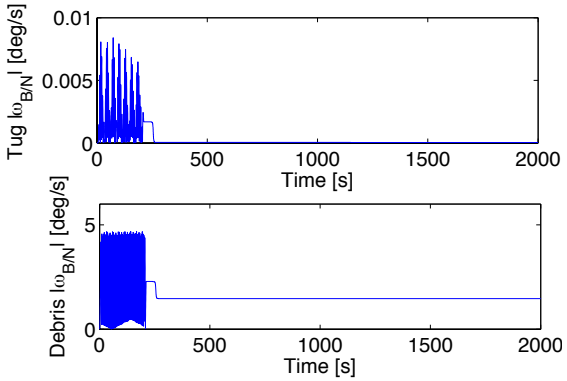

Figure 5.8: Example deep space rotation rates of the end bodies with $\phi_0 = 10^o$

5.2.2.2 On-Orbit Study

When putting the rotating system on-orbit, the overall performance changes considerably from the deep space behavior. Like in Chapter 3, both the notch and bang-off-bang controls do not settle into gravity gradient or tumbling motion. However the Posicast can achieve a tumble about nadir, as shown in Figures 5.9(a). Further, the rotation rate in Figure 5.9(c) is on par with the rates seen when the debris was not induced to spin. Much of the change in the rotation rate is induced by frequent tensioning of the tether on the bodies. The end bodies rarely complete a full rotation due to the tether tensioning frequently.

Looking at the maximum rotation rate angle from the deep space results, 50^o, Figure 5.9(b) that the the motion is no longer tumbling and there is a much more dynamic response in the end body separation. Figure 5.9(d) shows that the end body rotation rates are also much larger, causing them to spin up, potentially

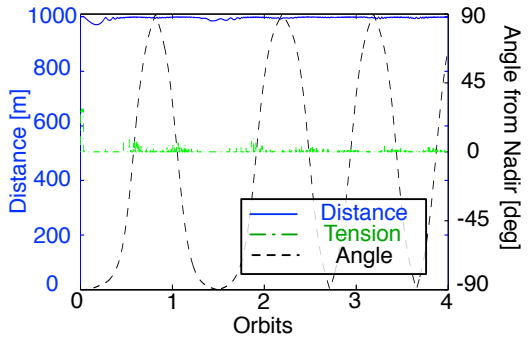

(a) Separation distance, tension, and angle from nadir for $\phi_0 = 10^o$

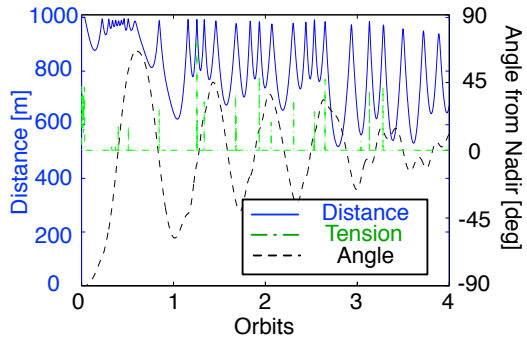

(b) Separation distance, tension, and angle from nadir for $\phi_0 = 50^o$

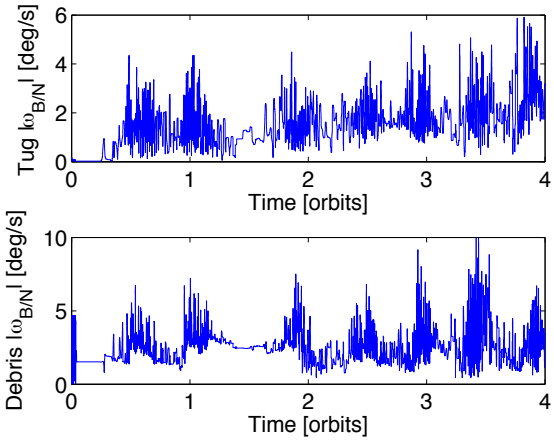

(c) Angular rotation for initial attachment offset of $\phi_0 = 10^o$

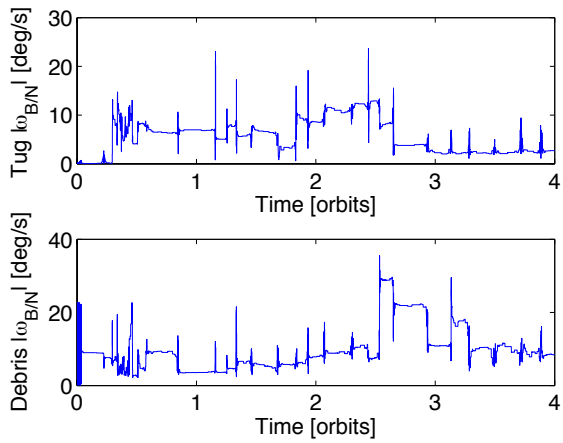

(d) Angular rotation for initial attachment offset of $\phi_0 = 50^o$

Figure 5.9: End body motion for a Posicast control with initial tether attachment offset, on-orbit

wrapping-up in the tether. This shows that while the Posicast control generally performs the best out of all the control methods for handling an offset tether attachment, it is limited to high or low angles, where the final end body rotation rates are relatively small.

5.2.3 Tumbling Debris

Tumble rates of debris is very hard to characterize. Radar frequently cannot provide spin rate information and optical observations are limited in their capabilities as well. When considering rocket bodies, studies suggest that if the rocket has been on-orbit for many months or several years, the eddy currents caused by the rocket's interaction with the Earth's magnetic field damp out its spin motion to only few de-

grees per second.[68] Using this as a metric for estimated tumble rates, the rocket is given an initial tumble rate of 1.15 deg/s about each axis (a 2 deg/s magnitude).

The Posicast control is applied to this system since it performed well in the on-orbit and deep space offset tether attachment study. Figure 5.10 demonstrates that the system can still achieve a tumbling motion with moderate rotation rates of the end bodies. Unfortunately, the debris is spun up more than its initial rotation rate, however this is consistent with the other scenarios that utilize Posicast input shaping and is an expected rotation rate profile. Because the system is spinning, but not necessarily making complete rotations, wrapping of the tether may be avoided, making this motion bad.

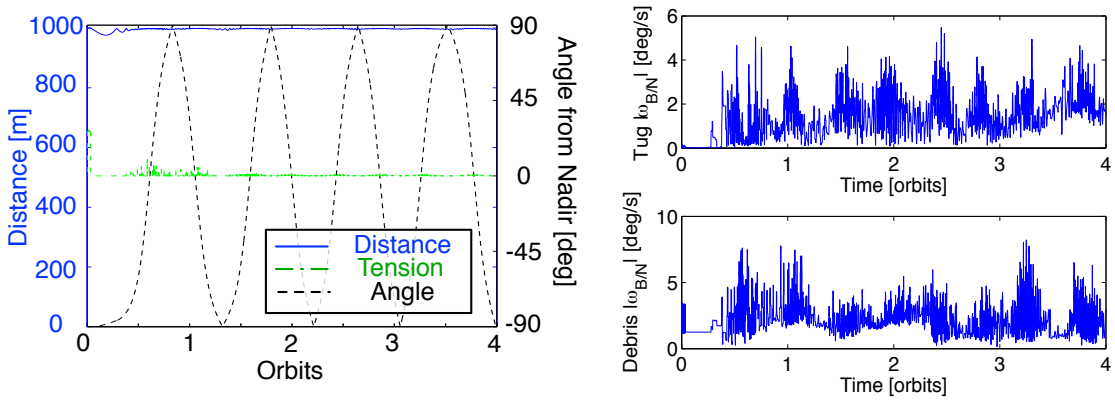

(a) Separation distance, tension, and angle from nadir

(b) Angular rotation rates

Figure 5.10: End body motion for a Posicast control with body rotation rate of 1.15^o/sec about each axis, on-orbit

5.3 Conclusions

With more realistic debris behavior and system performance, the tethered-tug still has a considerable design space in which to operate. While a slack tether, prior to thrusting, is unacceptable, pre-tensioning of the tether is a viable option, especially for the notch and Posicast filters.

Rotational motion of the debris adds another challenge to the system. However, the rotation rate of the debris can be approximated and used in input shaping techniques. Input shaping techniques can reduce some rotational motion in the debris, when compared to a step input while achieving the target tumble/gravity gradient behavior. Finally, it is interesting to see that the Posicast filter again appears to be

the most versatile for the wide range of system variables, while still being reasonably feasible with current rocket technology.

Chapter 6

Conclusion

6.1 Thesis Summary

Towing objects in space is a fundamentally challenging process that has been considered for many future missions. Frequently, capturing the target object is considered the primary obstacle and maneuvering the objects is not even mentioned. This dissertation addresses the complications associated with towing and suggests several open loop input shaping controllers to maneuver the system. Properly maneuvering this system is not simple if excessive end body motion, and high tether tensions, are to be avoided. Input shaping provides a method of applying thrust to the system that successfully maneuvers the bodies.

Step input thrust profiles are shown to have poor characteristics for the tethered system due to the highly dynamic motion of the end bodies, collision potential, and high tether tensions induced. The majority of the relative motion that occurs between both end bodies is due to the tether's first fundamental mode, that is excited by the step thrust profile. Reducing energy input into the system at this frequency, through thrust input shaping, effectively reduces these problems. Because the fundamental mode is the primary contributor to motion between the large end bodies only tether material properties and length affect the frequency. This means that the end body motion can be effectively modeled and studied without incredibly high-fidelity tether dynamics.

Applying a frequency notch to the step input allows for the thrust profile to have highly attenuated input at the system's natural frequency. This effectively reduces the relative motion between the end bodies causing almost zero relative velocity in deep space, and small drift rates while on-orbit. The notch is also made robust to system uncertainties through a double notch frequency filter spanning around the fundamen-

tal mode.

Unfortunately, the notch requires a continuously varying thrust profile that is not realistic with current rocket engine technology. The utilization of rigorous impulsive input shaping techniques, such as the Posicast and Bang-off-bang controllers, successfully attenuates the first natural frequency of the tethered-tug system providing reduced relative motion and tether tension while being more realistic for current-day rocket technology capabilities. The impulsive techniques are useful in both deep-space and on-orbit applications. However, the Posicast control produces the most beneficial motion on-orbit, falling into a tumbling motion about the nadir vector, with small end body rotation rates. Still, this dissertation has shown that a multitude of thrust profiles can be successfully implemented to control this system while avoiding collisions.

The design space for the tether is not directly intuitive and increases in length do not guarantee desirable performance. Similarly, the value of elasticity alone does not appear to significantly change system performance. However, it is very obvious that input shaping on the thrust profile is required to achieve any form of desirable performance without damping. With the correct conditions the system achieves a tumbling or gravity gradient motion with input shaping. Further, it appears that short to intermediate values for tether length ($L_0 = 100 - 2000$ m) achieve the best performance. Again, elasticity does not seem to drastically change performance of the system and so any stiff (Kevlar-based) tether appears acceptable.

With damping, the performance of the system significantly changes. Damping helps to moderately improve performance of an input shaped thrust profile by reducing end body motions and spin rates. However, when damping is applied to the step input thrust profile, the performance is drastically improved with higher damping ratios and gravity gradient motion can be induced. One of the most exciting results is that damping can be used as a replacement to input shaping, reducing some complexity for the rocket engine.

A slack tether, prior to thrusting, is detrimental to the system for all thrust profiles considered. It is therefore pivotal for the tether to be taut, or have some small pre-existing tension. The notch filter's response degrades the most gracefully as tension increases while the Posicast performs best with smaller tensions and the bang-off-bang performance is not greatly degraded by larger tensions.

Rotational motion also does not drastically reduce input shaping performance. The notch and bang-off-bang filters both can withstand some rotational motion but the Posicast filter performs the best on average

and causes fairly consistent end body rotation rates across all trials.

While multiple different thrust profiles could be utilized for this system, the robust Posicast filter is the most versatile to a variety of conditions and system properties. To implement a towing system in reality, significantly more design work is required. Still, there is a large design space for the tethered-tug and many possible configurations could be utilized to realize a safe system.

6.2 Future Work for the Tethered-Tug System

Beyond this dissertation, there are many avenues of future research for the tethered-tug system. For ADR systems in general, the process of rendezvous with the debris needs further study. Because the launch vehicle (tug) has minimal fuel resources after it has delivered its payload to orbit, its ability to reach another debris object will be limited. The range of the tug, and the phasing maneuver to another debris object should be understood to identify the amount of fuel that can be used for the de-orbit burn. Further, the capability of a launch vehicle to accurately rendezvous with another object should be explored. The identification of desirable debris to remove is another large task itself and continues to be studied.

The risks and expense associated with modifying a launch vehicle to perform the ADR mission is a real concern. While most of this dissertation is applicable to general towing in space, if the tethered-tug concept were to be used, significant changes to launch vehicles must be made. It is not a trivial task to perform rendezvous and capture operations, let alone have a rocket engine re-start multiple times, as is required by the input shaping profiles suggested.

An emerging and very active arena of research are the capture methods to be used. Grapples, harpoons, nets and other systems have all been proposed but all necessitate further research and testing before they would be ready for operation. Servicing of a satellite would require similar grappling methods however it may be assumed that the satellite to be serviced is cooperative, reducing overall complexity. Asteroid towing will require considerable development of attachment methods and asteroid properties.

Once the connection has been made and the orbit altering burn has been applied, the longer duration behavior of the system should be explored. A step input thrust creates very dynamic behavior. This behavior over a longer duration (more than several orbits) should be studied to determine if collisions actually do

occur. If the control has input shaping, the behavior of the system should be much more benign but long-term simulations should be explored to see how the behavior evolves over days, months and years.

If large damping within the tether is desired, it seems unlikely that material selection alone can achieve functional damping values. There are many mechanical solutions that could be used for this purpose. One example is a spring-shock system attached to either, or both, ends of the tether that are similar to shock systems in car suspensions. Cable brake systems could also be investigated for this purpose.

Improvements to the tether model can always be made and increasing the fidelity with more accurate internal forces (i. e. curling of the tether and use of string-like PDEs) may help to demonstrate less well understood tether effects. Further, FEM models could be used to achieve similar results however this would limit longer-duration simulations. Modeling the interaction between the tether and end bodies, with respect to wrapping in the tether, is also an improvement to the model that may yield new results for the behavior of the system. This will help to determine how pre-existing rotational motion and an offset tether attachment point will affect the system. This work shows that in deep space, each control method can minimize the induced spin, but they do not zero it. Induced spin will occur. How this behavior changes with wrapping is unknown.

Finally, the ADR system could be studied to determine its impact on the overall debris field. A kilometer long tether is a large structure in orbit. This is bound to create unforeseen complications and the likelihood of collision with other objects, both big and small, can be studied over a wide range of altitudes. The result of the tether being severed by a small piece of debris is also unknown and should be studied.

There are likely many questions beyond those addressed above, to be answered before this concept could ever become a reality. Encouragingly, there are many components of the concept that are currently possible and the concept relies on many technologies that exist today.

Bibliography

[1] AIAA. Orbital Debris Mitigation Techniques: Technical, Economic, and Legal Aspects, 1992. Special Project Report SP-016-1992.

[2] D. Alary. Astrium's views on oos & adr. In European On-Orbit Satellite Servicing and Active Debris Removal Conference, Brussels, Belgium, October 30 2012.

[3] A. P. Alpatov, V. V. Beletsky, V. I. Dranovskii, V. S. Khoroshilov, A. V. Pirozhenko, H. Troger, and A. E. Zakrzhevskii. Dynamics of Tethered Space Systems. CRC Press, 1st edition, 2010.

[4] Megan Ansdell. Active space debris removal: Needs, implications, and recommendations for today's geopolitcal envrionment. Journal of Public and International Affairs, 21:7 – 22, 2010. Princeton University.

[5] Luciano Anselmo and Carmen Pardini. Assessing the impact risk of orbital debris on space tethers. Space Debris, 1:87–98, 2000.

[6] Luciano Anselmo and Carmen Pardini. The survivability of space tether systems in orbit around the earth. Acta Astronautica, 56(3):391–396, 2005.

[7] Raymond G. Ayoub. Paolo ruffini's contributions to the quintic. Archive for History of Exact Sciences, 23(3):253–277, 1980.

[8] Riccardo Benvenuto and Michele Lavagna. Dynamics analysis and gnc design support tool of flexible systems for space debris active removal. In IAA Conference on Dynamics and Control of Space Systems, Rome, Italy, March 24–26 2014. IAA-AAS-DyCoSS2-14-09-02.

[9] Claudio Bombardelli and Jesus Pelaez. Ion beam shepherd for contactless space debris removal. Journal of Guidance, Control, and Dynamics, 34(3):916 – 920, 2011.

[10] C. Bonnal and C. R. Koppel. Getting rid of large debris: a safe low cost alternative. In 2nd European Workshop on Active Debris Removal, Quentin, Paris, France, June 18 – June 19 2012. Paper No. 3.2.

[11] B Buckham and M Nahon. Dynamics simulation of low tension tethers. OCEANS'99 MTS/IEEE. Riding the Crest into the 21st Century., 2:757 – 766, 1999.

[12] J. Burton and W. Hayes. Gemini rendezvous. Journal of Spacecraft and Rockets, 3(1):145–147, 1966.

[13] Joseph A. Carroll. Tether applications in space transportation. Acta Astronautica, 13(4):165–174, 1986.

[14] Joseph A. Carroll and John C. Oldson. Tethers for small satellite applications. In AIAA/USU Small Satellite Conference, Logan, Utah, 1995.

[15] M. P. Cartmell and D. J. McKenzie. A review of space tether research. Elsevier Progress in Aerospace Sciences, 44:1–21, 2008.

[16] Yi Chen and M Cartmell. Dynamical modelling of the motorised momentum exchange tether incorporating axial elastic effects. Advanced Problems in Mechanics: Russian Academy of Sciences, pages 20–28, June 2007.

[17] W. H. Clohessy and R. S. Wiltshire. Terminal guidance system for satellite rendezvous. Journal of the Aerospace Sciences, 27(9):653–658, 1960.

[18] Inter-Agency Space Debris Coordination Committee. IADC Space Debris Mitigation Guidelines. IADC, iadc-02-01 edition, Septemper 2007.

[19] M Dobrowolny and N H Stone. A technical overview of tss-1: the first tethered-satellite system mission. Il Nuovo Cimento, 17(1):1–12, 1994.

[20] T P Dreyer and D M Murray. On the modeling of two-dimensional segmented representations of cable shape. Ocean Engineering, 11(6):609 – 625, 1984.

[21] F R Driscoll, R G Lueck, and M Nahon. Development and validation of a lumped-mass dynamics model of a deep-sea rov system. Applied Ocean Research, 22:169 – 182, 2007.

[22] James Finch. Sustainability and the national security space strategy: An approach to the congested environment. In Address to the International Symposium on Sustainable Space Development and Utilization for Humankind, Tokyo, Japan, March 1 2012.

[23] Keck Institute for Space Studies. Asteroid Retrieval Feasibility Study. Smithsonian Astrophysical Observatory, Pasadena, California, 2012.

[24] David B French and Andre P Mazzoleni. Asteroid diversion using a long tether and ballast. Journal of Spacecraft and Rockets, 46(3):645–661, 2009.

[25] Robert B. Friend. Orbital express program summary and mission overview. In SPIE 6958, Sensors and Systems for Space Applications II, Orlando, FL, April 15 2008. Paper No. 695803, doi:10.1117/12.783792.

[26] Xiaohua He and David Powell. Tether damping in space. Journal of Guidance Dynamics and Control, 13(1):104–112, 1990.

[27] G. W. Hill. Researches in the lunar theory. American Journal of Mathematics, 1:5 – 26, 1980.

[28] Robert P Hoyt. Design and simulation of a tether boost facility for leo – gto transport. AIAA Paper 3866.3, 2000.

[29] Robert P Hoyt, Jeffrey Slostad, and Robert Twiggs. The multi-application survivable tether (mast) experiment. In The 39th AIAA/ASME/SAE/ASEE Joint Propulsion Conference and Exhibit, Huntsville, Alabama, July 20-23 2003. Paper 2003-5219.

[30] Leland B. Jackson. Digital filters and signal processing, volume 3. Kluwer Academic Publishers, Norwell, MA, 1989.

[31] Ram Jakhu. Towards Long-term Sustainability of Space Activities: Overcoming the Challenges of Space Debris. International Association for the Advancement of Space Safety, IAASS Legal and Regularoty Committee, February 15 2011.

[32] Lee Jasper and Hanspeter Schaub. Discretized input shaping for a large thrust tethered debris object. In 24th AAS/AIAA Space Flight Mechanics Meeting, Santa Fe, New Mexico, January 26–30 2014. AAS 14-446.

[33] Lee Jasper and Hanspeter Schaub. Input shaped large thrust maneuver with a tethered debris object. Acta Astronautica, 96:128–137, March-April 2014.

[34] Lee Jasper, Hanspeter Schaub, Carl Seubert, Trushkyakov Valery, and Evgeny Yutkin. Tethered tug for large low earth orbit debris removal. In AAS/AIAA Astrodynamics Specialists Conference, Charleston, SC, Jan 31 – Feb 2 2012. Paper No. AAS 12-252.

[35] Ruediger Jehn. Environmental challenges to space security. In ISU Summer Session 2009, Centre Darmstadt, Germany, 2009.

[36] L. Johnson, B. Gilchrist, R. D. Estes, and E. Lorenzini. Overview of future nasa tether applications. COSPAR Advanced Space Research, 24(4):1055–1063, 1985.

[37] Nicholas L. Johnson. Orbital debris: The growing threat to space operations. In 33rd Annual AAS Guidance and Control Conference, Breckenridge, CO, Feb. 6–10 2010.

[38] T.S. Kelso. CelesTrak. CSSI Center for Space Standards and Innovation, http://celestrak.com/, December 2012.

[39] Donald J. Kessler and Burton G. Cour-Palais. Collision frequency of artificial satellites: The creation of a debris belt. Geophysical Research, 83(A6):2637–2646, 1978.

[40] Mischa Kim and Christopher D. Hall. Control of a rotating variable-length tethered system. Advances in the Astronautical Sciences, 114:1713–1732, 2003.

[41] Krishna Kumar and K D Kumar. Auto-attitude stabilization of a twin-satellite system through very short tethers. Journal of Spacecraft and Rockets, 35(2):199–204, 1998.

[42] Ravi Kumar and Tarunraj Singh. Design of input shapers using modal cost for multi-mode systems. Automatica, 46(3):598–604, 2010.

[43] Claude Lafleur. Number of Spacecrafts Launched Each Year. Spacecraft Encyclopedia, September 2012.

[44] Jean De LaFontaine and Peter Hughes. An analytic version of jacchia's 1977 model atmosphere. Celestial Mechanics, (29):3 – 26, 1983.

[45] Nicolas N. Lee, Alan H. Zorn, and Matthew West. Passive vertical stabilization of two tethered nanosatellites with engineered damping. In AIAA/AAS Astrodynamics Specialist Conference and Exhibit, Honolulu, Hawaii, August 18–21 2008. Paper 2008-6450.

[46] D. Lewis, G. G. Parker, B. Driessen, and R. D. Robinett. Comparison of command shaping controllers for suppressing payload sway in a rotary boom crane. In International Conference on Control Applications, pages 719–724, Kohala Coast, Hawaii, 1999.

[47] J.-C. Liou. An active debris removal parametric study for leo environment remediation. Advances in Space Research, 47(11):1865 – 1876, 2011.

[48] J.-C. Liou and Nicholas L. Johnson. Risks in space for orbiting debris. Science, 311:340 – 341, 2006.

[49] J.-C. Liou, N.L. Johnson, and N.M. Hill. Controlling the growth of future leo debris populations with active debris removal. Acta Astronautica, 66(5-6):648 – 653, 2010.

[50] Yury Makarov, Alexander Ronse, and Valery Trushlyakov. The use of adapted upper stages for the removal of satellite and rocket body debris from unstable orbital regions. In 62nd International Astronautical Congress, Cape Town, South Africa, October 3 – 7 2011. IAC-11,A6,5,10,x10020.

[51] M J Mashayekhi and A K Misra. Tether assisted near earth object diversion. Acta Astronautica, 75:71–77, 2012.

[52] Darren McKnight. Pay me now or pay me more later: start the development of active orbital debris removal now. In Advanced Maui Optical and Space Surveillance Technologies Conference, Maui, Hawaii, September 14–17 2010.

[53] NASA, Marshall Space Center. Collision Probability of Apollo Spacecraft with Objects in Earth Orbit, msc in 67-fm-44 edition, April 10 1967.

[54] Arun Natarajan and Hanspeter Schaub. Linear dynamics and stability analysis of a two-craft coulomb tether formation. Journal of Guidance, Navigation and Control, 29(4):813–839, 2006.

[55] Simon Nolet, Alvar Saenz-Otero, David W. Miller, and Amer Fejzic. Spheres operations aboard the iss: maturation of gn&c algorithms in microgravity. In AIAA Guidance, Navigation and Control Conference and Exhibit, Hilton Head, South Carolina, August 2007. AAS 07-042.

[56] NASA Orbital Debris Program Office. History of On-orbit Satellite Fragmentations. NASA, 14 edition, June 2008.

[57] NASA Orbital Debris Program Office. Only a few minor satellite breakups in 2011. Orbital Debris Quarterly News, 16(1):1 – 8, 2012.

[58] NASA Orbital Debris Program Office. Upper stage explosion places leo satellites at risk. Orbital Debris Quarterly News, 17(1):1 – 8, 2013.

[59] Oystein Ore. Niels Henrik Abel: Mathematician Extraordinary. U of Minnesota Press, 1st edition, 1957.

[60] Carmen Pardini and Luciano Anselmo. Evolution of the debris cloud generated by the fengyun-1c fragmentation event. In 20th International Symposium on Space Flight Dynamics, Goddard Space Flight Center Greenbelt, MD, September 2007. NASA CP-2007-214158.

[61] Carmen Pardini and Luciano Anselmo. Physical properties and long-term evolution of the debris clouds produced by two catastrophic collisions in earth orbit. Advances in Space Research, (48):557 – 569, 2011.

[62] Carmen Pardini, T Hanada, and P H Krisko. Benefits and risks of using electrodynamic tethers to de-orbit spacecraft. Acta Astronautica, 64(5):571–588, 2009.

[63] Jerome Pearson, Joseph Carroll, Eugene Levin, John Oldson, and Paul Hausgen. Overview of the electrodynamic delivery express (edde). Defense Technical Information Center, 2003.

[64] Antoine Petit, Eric Marchand, and Keyvan Kanani. Tracking complex targets for space rendezvous and debris removal applications. In IEEE/RSJ International Conference on Intelligent Robots and Systems, pages 4483 – 4488, Vilamoura, Algarve, Portugal, October 7 - 12 2012.

[65] Antoine Petit, Eric Marchand, and Keyvan Kanani. Vision-based detection and tracking for space navigation in a rendezvous context. In International Symposium on Artificial Intelligence, Robotics and Automation in Space, Turin, Italy, November 11 2012. hal-00750606.

[66] Marcin D. Pilinski, Brian M. Argrow, Scott E. Palo, and Bruce R. Bowman. Semi-empirical satellite accommodation model for spherical and randomly tumbling objects. Journal of Spacecraft and Rockets, 50(3):556–571, 2013.

[67] David S. F. Portree. Orbital Debris: A Chronology. NASA, Lyndon B. Johnson Space Center Houston, Texas, nasa/tp-1999-208856 edition, January 1999.

[68] N Praly, M Hillion, C Bonnal, J Laurent-Varin, and N Petit. Study on the eddy current damping of the spin dynamics of space debris from the ariane launcher upper stages. Acta Astronautica, 76:145–153, 2012.

[69] J. Reed, J. Busquets, and C. White. Grappling system for capturing heavy space debris. In 2nd European Workshop on Active Debris Removal, Quentin, Paris, France, June 18 – June 19 2012. Paper No. 4.2.

[70] I. Retat, B. Bischof, J. Starke, WP Froth, and K. Bennell. Net capture system. In 2nd European Workshop on Active Debris Removal, Quentin, Paris, France, June 18 – June 19 2012. Paper No. 4.3.

[71] Hanspeter Schaub and John L. Junkins. Analytical Mechanics of Space Systems. American Institute of Aeronautics and Astronautics, Inc., 2nd edition, 2009.

[72] Hanspeter Schaub, Kurt Maute, and Daniel Moorer. Tethered Coulomb Structure. NRO, University of Colorado, Boulder, director's innovation initiative edition, November 2010.

[73] Hanspeter Schaub and Daniel F. Moorer. Geosynchronous large debris reorbiter: Challenges and prospects. In AAS Kyle T. Alfriend Astrodynamics Symposium, Monterey, CA, May 17–19 2010. Paper No. AAS 10-311.

[74] T Schildknecht, R Musci, and T Flohrer. Properties of the high area-to-mass ratio space debris population at high altitudes. Advances in Space Research, 41:1039–1045, 2008.

[75] Thierry Senechal. Orbital debris: Drafting, negotiating, implementing a convention. Thesis for Master of Business Administration, 2007. Massachusetts Institude of Technology.

[76] Carl Seubert, Stephen Panosian, and Hanspeter Schaub. Attitude and power analysis of two-node, multi-tethered coulomb structures. Journal of Spacecraft and Rockets, 48(6):1033–1045, 2011.

[77] Tarunraj Singh. Optimal Reference Shaping for Dynamical Systems, Theory and Applications. CRC Press, Boca Raton, Florida, 2010.

[78] Tarunraj Singh, Puneet Singla, and Umamaheswara Konda. Polynomial chaos based design of robust input shapers. Journal of Dynamic Systems, Measurement, and Control, 132:051010–1 – 13, 2010.

[79] W. E. Singhose, A. K. Banerjee, and W. P. Seering. Slewing flexible spacecraft with deflection-limiting input shaping. Journal of Guidance, Control, and Dynamics, 20(2):291–298, 1997.

[80] William Singhose. Command shaping for flexible systems: A review of the first 50 years. International Journal of Precision Engineering and Manufacturing, 10(4):153–168, 2009.

[81] William Singhose, Steve Drezinski, and Neil Singer. Extra-insensitive input shapers for controlling flexible spacecraft. Journal of Guidance, Control and Dynamics, 19(2):385–391, 1996.

[82] William Singhose, W. Seering, and Neil Singer. Residual vibration reduction using vector diagrams to generate shaped inputs. Journal of Mechanical Design, 116:654–659, 1994.

[83] Kirk Sorensen. Conceptual design and analysis of an mxer tether boost station. AIAA Paper 3915.3, 2001.

[84] Eugene Stansbery. NASA Orbital Debris Program Office Frequently Asked Questions. NASA, Lyndon B. Johnson Space Center Houston, Texas, March 2012.

[85] Brook Sullivan, David Barnhart, Lisa Hill, Paul Oppenheimer, Bryan Benedict, Gerrit van Ommering, Laurie Chappell, John Ratti, and Peter Will. Darpa phoenix payload orbital deliver system: "fexex to geo". In AIAA SPACE Conference and Exposition, San Diego, CA, September 10-12 2013. AIAA 2013-5484.

[86] Julie K Thienel, John M VanEepoel, and Robert M Sanner. Accurate state estimation and tracking of a non-cooperative target vehicle. In AIAA Guidance, Navigation and Control, Keystone, CO, August 21 – 24 2006.

[87] V. Trushlyakov, J. Makarov, G. Raykunov, J. Shatrov, and D. Baranovo. The development of autonomous onboard systems for the controlled deorbiting of stages separating parts of space launch vehicle. In 2nd European Workshop on Active Debris Removal, Quentin, Paris, France, June 18 – June 19 2012. Paper No. 2.5.

[88] A. Tustin. A method of analyzing the behavior of linear system in terms of time series. JIEE, London, 94(IIA):130–142, 1947.

[89] Takeo Watanabe, Takeshi Makida, Hironori A Fujii, Hirohisa Kojima, and William Singhose. An application of input shaping for electrodynamic tether system. In AIAA/AAS Astrodynamics Specialist Conference and Exhibit, Providence, Rhode Island, August 16–19 2004. Paper 2004-5313.

[90] Paul Williams. Dynamic multibody modeling for tethered space elevators. Acta Astronautica, 65:399–422, 2009.

[91] Kazuya Yoshida, Hiroki Nakanishi, Hiroshi Ueno, Noriyasu Inaba, Takeshi Nishimaki, and Mitsushige Oda. Dynamics, control and impedance matching for robotic capture of non-cooperative satellite. Advanced Robotics, 18(2):175–198, 2004.

[92] Dawei Zhang, Shenmin Song, and Run Pei. Safe guidance for autonomous rendezvous and docking with a non-cooperative target. In AIAA Guidance, Navigation and Control, Toronto, Ontario, Canada, August 2 – 5 2010. AIAA 2010-7592.

[93] Douglas Zimpfer, Peter Kachmar, and Seamus Tuohy. Autonomous rendezvous, capture and in-space assembly: past, present and future. In 1st Space Exploration Conference: Continuing the Voyage of Discovery, Orlando, Florida, January 30 - February 1 2005. AIAA 2005-2523.